Insights into the Electronic Nature of the Iron Porphyrin Framework: A Computational Study

by

Victoria E. J. Berryman

Submitted in partial fulfilment of the requirements
for the degree of Doctor of Philosophy

at

Dalhousie University
Halifax, Nova Scotia
March 2015

This thesis is dedicated to my teachers
for being a source of knowledge and inspiration.

Table of Contents

List of Tables

viii

List of Figures

Abstract

Density functional theory, a quantum mechanical based electronic structure method, is used to investigate iron porphyrin systems. Specific interest in the electronic structure of the heme group in myoglobin and hemoglobin has motivated investigations of the geometry and electronic nature of the deoxy-heme system, as well as binding energies for O_2 and subsequent NO oxidation of the oxyheme complex.

Specifically, the size of iron within the porphyrin ring in different spin states of the iron porphyrin complex is analyzed using the quantum theory of atoms in molecules (QTAIM). It is shown that the bonding interaction between the iron atom and the axial ligand has a more significant role in the domed structure of the high-spin state, counter to previous explanations of the atomic volume of iron contributing to increased doming in the high-spin ground state.

The performance of contemporary density functional approximations is assessed, with specific interest on the effects of including Hartree-Fock exchange when investigating iron porphyrin systems. Varied amount of Hartree-Fock exchange are employed in popular hybrid and range-separated type functionals. It is found that increasing Hartree-Fock exchange improves the ability of the functional to correctly predict the high-spin ground state, however, inhibits the prediction of favourable dioxygen binding to the system.

Binding of oxygen to heme and subsequent nitric oxide oxidation of the oxyheme species is of significant interest to aid in advancing the field of cell-free blood substitutes, as well as understanding analogous systems to assist in protein design, development of catalysts, and designing therapeutics. The mechanism of NO oxidation is explored and the effect of replacing the proximal histidine, which tethers heme to the protein backbone, with other amino acid ligands is probed. The binding energies of dioxygen to the system, and resulting superoxide character of the dioxygen ligand are reported. Substitution of the amino acid group is found to have little effect on the NO affinity of the oxyheme system, however, electronic differences suggest modification of the reaction mechanism may be possible and requires further study.

List of Abbreviations and Symbols Used

Abbreviations

Arg	Arginine
au	Atomic units
BCP	Bond critical point
BE	Binding energy
CC	Coupled cluster
CCP	Cage critical point
CFBS	Cell-free blood substitute
CGF	Contracted Gaussian function
CI	Configuration interaction
Cys	Cysteine
DFA	Density functional approximation
DFT	Density functional theory
erf	Gauss error function
erfc	Complementary Gauss error function
FeP	Iron (II) porphine
FePIm	Imidazolium ligated iron (II) porphine
FePIm-O_2	Dioxygen bound FePIm
FePL	Iron (II) porphine with a ligand denoted L
FePL-O_2	Dioxygen bound to FePL
GGA	Generalized gradient approximation
Glu	Glutamic acid
GTO	Gaussian-type orbital
HF	Hartree-Fock theory
His	Histidine
HOMO	Highest occupied molecular orbital
KS	Kohn-Sham
LCAO	Linear combination of atomic orbitals
LDA	Local density approximation
LSDA	Local spin-density approximation

Met	Methionine
MPPT	Møller-Plesset perturbation theory
NCP	Nuclear critical point
QTAIM	Quantum theory of atoms in molecules
RCP	Ring critical point
RHF	Restricted Hartree-Fock
ROHF	Restricted open-shell Hartree-Fock
S	Spin angular momentum
SCF	Self-consistent field
SI	International System of Units
SOMO	Singly occupied molecular orbital
STO	Slater-type orbital
TS	Transition state
Tyr	Tyrosine
UHF	Unrestricted Hartree-Fock

Symbols

h	Planck constant
m_e	Electron mass
e	Electron charge
$\hbar$	Reduced Planck constant, or Dirac constant
π	Pi, the mathematical constant equal to the ratio of the circumference to the diameter of a circle
ε_0	Permittivity of the vacuum
$\hat{H}$	Hamiltonian operator
E	Total energy
Ψ	Wave function
m_A	Mass of nucleus A
r_{ij}	Distance between particles i and j
Z_A	Effective nuclear charge of nucleus A
∇^2	Laplacian operator
$\hat{H}_{elec}$	Electronic Hamiltonian
$\hat{T}$	Kinetic energy operator
$\hat{V}$	Potential energy operator
$\vec{r}$	Position vector of an electron
χ	Spin-orbital function or molecular orbital
ψ	Spatial orbital function
σ	Electron spin
α or β	Spin function (up or down)
Ψ^*	Complex conjugate of the wave function
Φ_{SD}	Slater determinant
N	Number of electrons in a system
δ	Kronecker delta
ε_i	Lagrangian multiplier
$\hat{F}$	Fock operator

$\hat{J}$	Coulomb integral
$\hat{K}$	Exchange integral
φ	Basis function
c	Basis function expansion coefficient
S	Overlap integral
H^{core}	Core Hamiltonian
$D_{\sigma\gamma}$	Density matrix
$\nu\mu \mid \sigma\gamma$	Two-electron repulsion integral
Y_l^m	Spherical harmonic function
θ, ϕ	Angles in polar coordinates
ζ	Orbital exponent
n, l, m	Quantum numbers describing the shell, subshell and orbital of an electron, respectively
N	Normalization constant
$d_{u\tau}$	Basis function contraction coefficient
*	Polarization function in a Pople-type basis set
+	Diffuse function in a Pople-type basis set
$\hat{A}$	Perturbation to the Hamiltonian
λ	Perturbation parameter
$\rho(\vec{r})$	Electron density
$E_0[\rho_0]$	Energy expressed as a functional of the electron density
$F[\rho_0]$	Universal functional
$\hat{f}^{KS}$	Kohn-Sham operator
ϕ	Kohn-Sham orbital
ε_i^{KS}	Kohn-Sham orbital energy
$\nabla\rho$	Gradient of the electron density
$\nabla^2\rho$	Laplacian of the electron density
A	Hessian matrix
ϖ	Rank of a critical point
ϑ	Signature of a critical point

Å	Angstrom
ω	Interelectronic distance parameter for partitioning in range-separated density functionals
δ	Delocalization index
pK_a	Negative logarithm of the acid dissociation constant
pH	Measure of acidity, Negative logarithm of the hydronium ion concentration
ΔG	Change in Gibbs energy
ΔH	Change in enthalpy
ΔS	Change in entropy

Acknowledgements

I would first like to gratefully acknowledge my supervisor, Prof. Russell Boyd, for the opportunity to pursue graduate studies under his supervision. The direction and thoughtful guidance he has provided me has been invaluable. I am especially thankful for his constant support and encouragement along my graduate school journey.

I would also like to acknowledge my co-supervisor, Prof. Axel Becke, for numerous insightful conversations. His passion for density functional theory has made a lasting impression. I also acknowledge the members of my supervisory committee, Profs. Donald Weaver and Peng Zhang, for their time and support.

Dr. Norberto Castillo and Prof. Chérif Matta performed preliminary work relating to Chapter 3 and are acknowledged for their helpful suggestions during the preparation of the manuscript. Prof. Erin Johnson is gratefully acknowledged for her assistance with Chapter 4. Her guidance, insight and suggestions were invaluable to the success of the project. Matthew Baker worked on binding energies closely associated with the work in Chapter 5 and is acknowledged for his hard work. Prof. Jesus Ugalde is acknowledged for welcoming me to his research group in Donostia, Spain during my studies. Although research we pursued is not presented in this thesis, the experience was unforgettable.

I am grateful to the members of the Boyd, Weaver and Becke research groups for many discussions, both helpful and entertaining. My time in graduate school has been more enjoyable as a result of these individuals.

The financial support of the Natural Sciences and Engineering Research Council of Canada (NSERC), Atlantic Computational Excellence Network (ACEnet), Walter C. Sumner Foundation, and Dalhousie University is graciously acknowledged. Also, the computational resources provided by ACEnet, WestGrid, and Dalhousie University have made this research possible.

I would also like to thank my family and friends for their constant encouragement and support. I am grateful to my parents for being my first supporters and for always believing in me. I am especially thankful to my husband. His unconditional support has been essential during my academic endeavours. Finally, I thank my son, Jack, who, although too young to understand my efforts, never fails to brighten my day.

Chapter 1 : Introduction

1.1   Porphyrins

Porphyrins are a class of molecules characterized as heterocyclic macrocycles composed of four pyrrole subunits joined via the α-carbons by methine groups. They are prominent molecules found ubiquitously in nature and thus generate a significant amount of research interest in almost every field of science, including chemistry, biology, materials science, physics and medicine. The characteristic attributed for many of the unique chemical properties of the porphyrin framework is the alternating system of double bonds, allowing π-electrons to delocalize over the perimeter of the porphyrin structure. The extended nature of the conjugated system gives rise to unique properties such as intense absorption of light in the visible spectrum. Porphyrins are perhaps best known as the red pigment of blood, from the iron porphyrin containing hemoglobin protein, and the green pigment of leaves, from the magnesium porphyrin containing biomolecule chlorophyll. They are also extremely versatile structures, capable of many substitutions, yielding derivatives with an array of interesting biological and chemical properties. Porphyrins are also versatile ligands that can coordinate to nearly every atom of the periodic table. Consequently, these structures are the subject of much scientific interest and represent an incredibly active area of research.[1–4]

The simplest, unsubstituted porphyrin is known as porphine and is shown in Figure 1.1. The conjugated nature of the system is depicted in this elegant structure. Porphine is frequently used to model substituted porphine systems, known generally as porphyrin systems. Most notably, iron containing porphine is employed to study heme. Heme is a biologically relevant coenzyme found in numerous proteins and enzymes, such

as myoglobin, hemoglobin, cytochromes, catalases, and peroxidases. Proteins containing heme are one of the most studied classes of biomolecules. In this thesis, an iron porphine system is employed extensively as a model system to investigate the complex nature of heme containing systems.
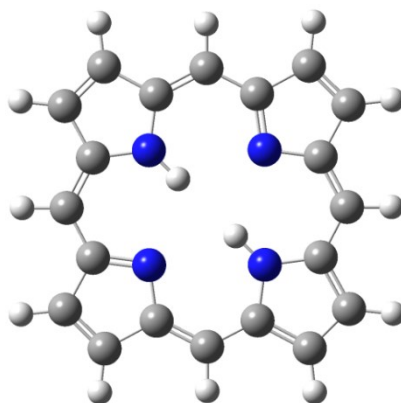
Figure 1.1. Molecular structure of porphine. Carbon, nitrogen and hydrogen atoms are shown as grey, blue and white spheres, respectively.

1.2   Computational Chemistry

The advent of quantum mechanics led to the development of the field of computational chemistry which allows chemists to investigate chemical systems beyond the limits of experimental methods. A subfield of theoretical chemistry, computational chemistry employs computers to perform mathematical operations to ultimately gain insight into chemical systems. There are two general areas of computational chemistry: molecular mechanics and electronic structure theory. The former uses the laws of classical physics and the spatial arrangement of the nuclei in a chemical system. Electronic structure theory methods are based on the laws of quantum mechanics and the position of both nuclei and electrons. Both aim to compute the energy of a molecular system and derive properties of the system to solve problems of chemical relevance. A number of textbooks provide comprehensive introductions to computational chemistry.[5–7]

Ultimately, our ability to exactly compute the structure and properties of matter using quantum mechanics is limited by the computational demand of these calculations. In theory, calculations using the full configuration interaction (CI) method with a complete basis set give an exact solution to the non-relativistic, time-independent Schrödinger equation employing the Born-Oppenheimer approximation. However, these calculations are only possible for systems containing a very small number of electrons. In practice, high level coupled-cluster theory is regarded as the gold standard for benchmarking quantum mechanical methods and can be computed accurately for small to medium-sized molecular systems. Although these methods provide accurate results, the computational demand increases extraordinarily with the size of the system, factorially, with respect to the number of electrons, for full configuration interaction, and thus more efficient approximate computational methods are essential. It is for this reason that density functional theory (DFT) has gained significant and widespread popularity. The popularity of DFT has grown exponentially, driven by the excellent level of accuracy and computational efficiency it provides. Density functional theory is employed exclusively for the research presented in this thesis. Some of the fundamentals of this method are discussed in section 2.12.

The advantages of computational chemistry over conventional experimental methods are numerous. A significant benefit is that research is not limited to species that can be synthesized in a particular lab. Extensive experimental study of systems can be restricted by the expense of chemical reagents. Computational studies make the investigation of these systems financially feasible. Also, the safety of the scientist is not a concern when investigating radioactive, hazardous or highly reactive species. On a

larger scale, computational chemistry is a green research field. Solvent waste is not generated and toxic chemical agents are not required since research is carried out on computers.

Computational methods are often used to complement experimental results. Computational studies have been especially useful for mechanistic studies since high energy transition states and intermediate products are often difficult to isolate experimentally. Many short-lived species are only hypothesized to exist, however these previously inaccessible systems can be examined using computational methods. The impact of quantum mechanical methods, such as density functional theory, is immense and accelerating. This is a result of the advancements in methods, and technology, which have allowed for the permeation of the field into many scientific disciplines such as chemistry, condensed matter physics, atmospheric physics, biochemistry and biology. Computational studies are becoming an important adjunct to experimental research and are increasingly being considered an essential component of publications.

Chapter 2 : Theoretical Background

2.1   Introduction

Quantum mechanics was born out of the failure of classical physics to describe blackbody radiation, the electromagnetic radiation emitted from heated matter.   A blackbody is an ideal object, in other words, an opaque, non-reflective object that absorbs all radiation and re-emits it at a characteristic spectrum.   The light, or electromagnetic radiation, emitted from a blackbody depends only on the temperature of the system. Classical physics predicted an infinite amount of energy is emitted from a blackbody, which is not physically accurate.

In 1900, Max Planck described blackbody radiation by breaking away from the convention of classical physics that allowed observables, such as momentum and energy, to exist at any value. Planck proposed that the energies had to exist in discrete, quantized values. He predicted each frequency of wave had an intrinsic energy. Thus, a wave must have an energy less than the associated temperature of the blackbody to contribute to the energy of the emitted radiation. Using this hypothesis Planck was able to explain the full experimental spectra of blackbody radiation for the first time *hitherto*.[8] It was at this time that he defined what is known today as Planck's law and the familiar Plank constant, h. Shortly thereafter, Einstein used this concept to explain the photoelectric effect.[9] Consequently, quantum mechanics was able to describe what classical mechanics could not, the behaviour of atomic and subatomic systems. Throughout the 1920s quantum theory was shaped by individuals such as Werner Heisenberg, Max Born, Wolfgang Pauli, Niels Bohr, Erwin Schrödinger, Paul Dirac and John von Neumann.

In this chapter, some of the fundamentals of electronic structure theory and various methods used in the field of quantum chemistry are introduced. Emphasis has been placed on density functional theory (DFT), which is used exclusively in the work discussed in this thesis. A comprehensive review of the theoretical background of computational chemistry is beyond the scope of this thesis. Such a discussion of this nature can be found in quantum chemistry textbooks.[10,7,11,12]

2.2   Atomic Units

Unlike many fields of science which use the International System of Units, commonly referred to as SI units, equations in quantum chemistry are typically expressed using the system of atomic units, which are abbreviated as au. In this system four fundamental physical constants are set to unity. These are the electron mass, m_e, electron charge, e, reduced Planck constant, $\hbar$, equal to the Planck constant divided by 2π, and Coulomb's constant, $\dfrac{1}{4\pi\varepsilon_0}$, where ε_0 the permittivity of the vacuum.[13] This allows for properties such as angular momentum, length, and energy to be expressed as multiples of these constants, resulting in compact equations since they appear without fundamental physical constants.

Another advantage of using atomic units to express computed quantities is that the value will not change over time. Values reported using a system of measurement based on physical constants, for example, SI units, vary depending on the value of the constant used. Physical constants are based on experimental measurements that are accompanied by some amount of uncertainty and limited by the development of accurate experimental methods. For example, the speed of light is one of the most measured fundamental

physical constants.[14] Since 1875, the reported value for the speed of light has changed numerous times deviating by as much as 2.1×10^5 m·s⁻¹ from the currently accepted value of 2.9979×10^8 m·s⁻¹.[15] Atomic units are robust and thus values expressed in atomic units are not subjected to changes based on accepted values of measured physical constants.

2.3   Schrödinger Equation

Central to quantum mechanics is the Schrödinger equation whose approximate solution is the objective of quantum chemistry methods. The Schrödinger equation was proposed by Erwin Schrödinger in 1926 and describes the wave and particle behaviour of electrons.[16] The significance of this equation was recognized in 1933, when Erwin Schrödinger shared the Nobel Prize in Physics, with Paul Dirac, for his contributions to quantum theory. In its condensed form, the time-independent Schrödinger equation is written as,

$$\hat{H}\Psi = E\Psi \qquad\qquad \textbf{2.1}$$

where $\hat{H}$ is the Hamiltonian operator and E is the total energy of the system whose state is described by the wave function, Ψ. The Hamiltonian operator contains the energy operators of the system. For a system with M nuclei denoted A and B and N electrons denoted i and j the Hamiltonian operator can be expanded to,

$$\hat{H} = -\frac{1}{2}\sum_{i=1}^{N}\nabla_i^2 - \frac{1}{2}\sum_{A=1}^{M}\frac{1}{m_A}\nabla_A^2 - \sum_{i=1}^{N}\sum_{A=1}^{M}\frac{Z_A}{r_{iA}} + \sum_{i=1}^{N}\sum_{j>i}^{N}\frac{1}{r_{ij}} + \sum_{A=1}^{M}\sum_{B>A}^{M}\frac{Z_A Z_B}{r_{AB}} \qquad \textbf{2.2}$$

where the mass of nucleus A is denoted m_A, the distance between two particles, for example i and j, is denoted r_{ij} and the effective nuclear charge of nucleus A is denoted

7

Z_A. The Laplacian operator, ∇^2, is the sum of the differential operators and, in Cartesian coordinates, is defined as,

$$\nabla^2 = \frac{\partial^2}{\partial x^2} + \frac{\partial^2}{\partial y^2} + \frac{\partial^2}{\partial z^2}$$ **2.3**

The first two terms of the Hamiltonian operator, given in equation 2.2, describe the kinetic energy of the system, more specifically the electronic and nuclear kinetic energies, respectively. The middle term represents the potential energy that arises as a result of the electrostatic attraction between the nuclei and electrons. The final two terms describe the potential energy resulting from the repulsion between the electrons and nuclei, respectively.

The time-independent form of the Schrödinger equation yields stationary state wave functions, which is sufficient to solve many problems of interest to chemists. Although an exact solution to the Schrödinger equation can be obtained for simple systems such as a particle in a box, the harmonic oscillator and single-electron systems, there is no exact solution for multi-electron systems. Consequently, investigating chemically relevant systems relies on methods that seek approximate solutions through simplification and parameterization.

2.4   Born-Oppenheimer Approximation

The Born-Oppenheimer approximation, sometimes referred to as the clamped-nuclei approximation, assumes the electrons of a system move in a field defined by fixed nuclei and therefore the kinetic energy of the nuclei is zero. This makes intuitive sense considering the mass of a nucleus consisting of only a single proton, for example a hydrogen atom, is approximately 1800 times greater than the mass of an electron. In

other words, the velocity of the nuclei is negligible compared to the velocity of the electrons and there is negligible coupling between their motions.[17] By separating the nuclear and electronic motion we can assume that the nuclei are at fixed positions. Since there is no nuclear motion, the nuclear kinetic energy is zero and the potential energy resulting from nuclear repulsion becomes a constant, reducing the Hamiltonian to,

$$\hat{H}_{elec} = -\frac{1}{2}\sum_{i=1}^{N}\nabla_i^2 - \sum_{i=1}^{N}\sum_{A=1}^{M}\frac{Z_A}{r_{iA}} + \sum_{i=1}^{N}\sum_{j>i}^{N}\frac{1}{r_{ij}} = \hat{T} + \hat{V}_{ne} + \hat{V}_{ee} \qquad \textbf{2.4}$$

where $\hat{H}_{elec}$ is known as the electronic Hamiltonian. The electronic Hamiltonian is comprised of the electronic kinetic energy, electron-nuclei attraction potential and electron-electron repulsion potential energy terms, abbreviated as $\hat{T}$, $\hat{V}_{ne}$ and $\hat{V}_{ee}$, respectively. Use of the electronic Hamiltonian to solve the Schrödinger equation yields the total electronic energy, E_{elec}. The total energy of a system is the sum of the electronic energy and the potential energy from nuclear repulsion, E_{nuc}, such that,

$$E_{total} = E_{elec} + E_{nuc} \qquad \textbf{2.5}$$

The E_{nuc} term is a constant since the nuclei are fixed. The Born-Oppenheimer approximation introduces very little error, providing a valid simplification of the Schrödinger equation and is a cornerstone of computational chemistry methods.

It should be noted that the electronic Hamiltonian terms which are system dependent are the charges and positions of the nuclei, denoted Z_A and r_A, respectively, and the number of electrons, N. In other words, the Hamiltonian can be uniquely determined by $\hat{V}_{ne}$ and N.

2.5   Orbital Approximation

A many-electron wave function is a complex function depending on the coordinates of all the electrons it describes,

$$\Psi(\vec{r}_1,\vec{r}_2,...,\vec{r}_N)$$
2.6

where $\vec{r}_i$ is the vector from the nucleus to electron i. The orbital approximation assumes that the exact wave function can be approximated by assuming that each electron occupies a single independent orbital. The wave function can therefore be represented as,

$$\Psi(\vec{r}_1,\vec{r}_2,...,\vec{r}_N)=\psi(\vec{r}_1)\psi(\vec{r}_2),...,\psi(\vec{r}_N)$$
2.7

where the wave function is represented as a product of one-electron functions, or orbitals, denoted by $\Psi(\vec{r}_i)$. This representation is known as the Hartree product. By expressing the wave function in such a way, the orbital approximation assumes the motion of the electrons to be independent of one another.

The above orbitals only contain the spatial coordinates of the electrons, however, a complete description would also include the intrinsic spin coordinates. Consequently, spin-orbitals, denoted $\chi(\vec{x})$, are more frequently used to describe electrons. The $\vec{x}$ term associated with each spin-orbital function contains information about the position, $\psi(\vec{r})$, and spin, either $\alpha(s)$ or $\beta(s)$, for each electron and can be expressed as,

$$\chi(\vec{x})=\psi(\vec{r})\sigma(s),\quad \sigma=\alpha,\beta$$
2.8

In other words, the spin-orbital function is the product of the spatial orbital and the spin function.

2.6   Properties of the Wave Function

The wave function is a function of position and time that contains all the information that can be obtained from a quantum mechanical system. The wave function is not an observable property, however, the square of the wave function represents the probability that a set of electrons can be found simultaneously in a given volume element,

$$|\Psi(\vec{x}_1,\vec{x}_2,...,\vec{x}_N)|^2 d\vec{x}_1, d\vec{x}_2,..., d\vec{x}_N \qquad \textbf{2.9}$$

and is known as the probability density. It follows intuitively that the probability of finding the N electrons anywhere is space is equal to one,

$$\int...\int |\Psi(\vec{x}_1,\vec{x}_2,...,\vec{x}_N)|^2 d\vec{x}_1, d\vec{x}_2,..., d\vec{x}_N = 1 \qquad \textbf{2.10}$$

and any wave function that satisfies this property is said to be normalized. The majority of quantum chemical methods deal with normalized wave functions.

Electrons are indistinguishable from one another and therefore if the coordinates of any of the electrons were interchanged then their properties must remain the same. This holds true for the probability thus,

$$|\Psi(\vec{x}_1,\vec{x}_2,...,\vec{x}_i,\vec{x}_j,...,\vec{x}_N)|^2 = |\Psi(\vec{x}_1,\vec{x}_2,...,\vec{x}_j,\vec{x}_i,...,\vec{x}_N)|^2 \qquad \textbf{2.11}$$

This implies that there are two possible solutions for the wave function: they are identical, making the wave function symmetric; or the interchange results in a sign change, making it antisymmetric. Since electrons are fermions, having half-integral spin values, they are known to be antisymmetric, such that,

$$\Psi(\vec{x}_1,\vec{x}_2,...,\vec{x}_i,\vec{x}_j,...,\vec{x}_N) = -\Psi(\vec{x}_1,\vec{x}_2,...,\vec{x}_j,\vec{x}_i,...,\vec{x}_N) \qquad \textbf{2.12}$$

The well-known Pauli exclusion principle, which states that no two electrons can occupy the same quantum state, is a consequence of the antisymmetric property of wave

functions. It should be noted that a major shortcoming of the Hartree product, given in equation 2.7, is the failure to satisfy the antisymmetric property of the wave function.

2.7   The Variational Principle

In order to solve the Schrödinger equation, the Hamiltonian operator for the system of interest must be determined, from which the eigenfunction, Ψ, and consequently the eigenvalue, E can be determined. As previously noted, the system dependent terms of the Hamiltonian operator are the number of electrons and the charges and positions of the nuclei. Although this process may seem straightforward, it has no practical application. The Schrödinger equation can only be solved exactly for simple systems containing one electron, such as the hydrogen atom. Thus, where direct solutions of the Schrödinger equation are not possible, methods to obtain approximate solutions are pivotal to the success of quantum mechanical methods.

The variational principle states that the energy computed as the expectation value of an arbitrary, normalized wave function can only be higher than or equal to the true energy of the ground state of the system. That is,

$$\left\langle \hat{H} \right\rangle = \int ... \int \Psi_{trial}^{*} \hat{H} \Psi_{trial} d\vec{x}_1 d\vec{x}_2 ... d\vec{x}_N = \left\langle \Psi_{trial} \left| \hat{H} \right| \Psi_{trial} \right\rangle = E_{trial} \geq E_0 = \left\langle \Psi_0 \left| \hat{H} \right| \Psi_0 \right\rangle \qquad \textbf{2.13}$$

where Ψ^{*} is the complex conjugate of the wave function. E_0 and Ψ_0 are the ground state energy and wave function, respectively. Equation 2.13 is shown in bra-ket notation, also known as Dirac notation, which is common practice in the field of quantum mechanics. It follows that the energy of the wave function can act as a measure of its quality, since the energy will always be too high for an approximate wave function. In short, the variational principle provides a foundation for determining the ground state

wave function, from all acceptable, *N*-electron wave functions, since it returns the minimum energy and is therefore the true ground state energy.

2.8 The Hartree-Fock Approximation

Since it is not practical to search all possible wave functions, the Hartree-Fock approximation helps to provide a subset of potential wave functions on which to employ the variational principle. It is a prominent approximation used in the majority of wave function based quantum mechanical methods. The Hartree-Fock approximation uses a normalized, antisymmetrized product of N one-electron functions, or spin-orbital functions, denoted $\chi_i(\vec{x}_i)$, to approximate the N-electron wave function. This product is called a Slater determinant,[18,19] denoted Φ_{SD}, and is written as,

$$\Psi = \Phi_{SD} = \frac{1}{\sqrt{N!}} \begin{vmatrix} \chi_1(\vec{x}_1) & \chi_2(\vec{x}_1) & \cdots & \chi_N(\vec{x}_1) \\ \chi_1(\vec{x}_2) & \chi_2(\vec{x}_2) & \cdots & \chi_N(\vec{x}_2) \\ \vdots & \vdots & \ddots & \vdots \\ \chi_1(\vec{x}_N) & \chi_2(\vec{x}_N) & \cdots & \chi_N(\vec{x}_N) \end{vmatrix} \qquad \textbf{2.14}$$

where the $(N!)^{-1/2}$ term imposes normalization of the wave function. The antisymmetric property of the wave function is upheld since if two rows, or electrons, of the determinant are interchanged the sign of the determinant changes. The construct of the Slater determinant also ensures that the wave function upholds the Pauli exclusion principle since if two of the electrons have the same spin and position (i.e. $\vec{x}$) then two columns of the determinant would be equal and the determinant would vanish. Thus the condition that two electrons with the same spin have zero probability of being found at the same position in space is not a result of physical forces, but a reflection of the mathematical properties of the wave function. It should also be noted that both the spin functions and

spin-orbital functions are orthonormal. This property can be represented by the Kronecker delta, δ, and is shown here for the spin-orbital functions,

$$\int \chi_i^*(\vec{x}_i)\chi_j(\vec{x}_j)d\vec{x} = \delta_{ij} \qquad \textbf{2.15}$$

where the Kronecker delta equals 1 when $i = j$ and 0 otherwise. It is effectively the spin-orbital functions, constrained so that they remain orthonormal, that are varied to determine the Slater determinant that yields the lowest energy.

2.9   Hartree-Fock Theory

Shortly after the derivation of the Schrödinger equation, in 1927, Hartree proposed the self-consistent field method as a way to obtain approximate solutions to the Schrödinger equation from an *ab initio* approach.[13,20] This is known as the Hartree method. The Hartree method approximates the electron-electron repulsion term, $\hat{V}_{ee}$, with the average repulsion of the electrons. In addition the approximation of the $\hat{V}_{ee}$ term, the method does not maintain the antisymmetry property of the wave function. Gaunt, Slater and Fock independently contributed to the advancement of the Hartree method.[21–24] Significant improvements include application of the variational principle and the use of the Slater determinant, a product of one electron orbitals that ensures consistency with the antisymmetric property of the wave function, as a trial wave function. Hartree redefined his original method in 1935 to include these improvements, known as the Hartree-Fock method (HF).[25] Although the HF method was the most accurate technique *hitherto*, it was not widely used until electronic computers emerged in the 1950s. Currently, the HF method, as a standalone method, is not routinely employed in modern computational chemistry; however, the method provides the foundations for

many current quantum mechanical based computational methods and is thus, briefly discussed herein.

2.9.1 The Hartree-Fock Equations

In the HF method the energy is calculated as the expectation value of the Hamiltonian operating on the Slater determinant, given in bra-ket notation as,

$$E_{HF} = \left\langle \Phi_{SD} \middle| \hat{H} \middle| \Phi_{SD} \right\rangle \qquad \textbf{2.16}$$

The spin-orbital functions that yield the lowest energy for a system are obtained iteratively from the Hartree-Fock equation,

$$\hat{F}\chi_i = \varepsilon_i \chi_i \qquad \textbf{2.17}$$

where ε_i is the Lagrangian multiplier which represents the energy of the spin-orbital and $\hat{F}$ is the Fock operator. Koopmans' theorem states that the energy associated with the spin-orbital is an approximation of negative the ionization energy required to remove an electron from that orbital.[26] The Fock operator is defined as,

$$\hat{F} = -\frac{1}{2}\nabla_i^2 - \sum_A^M \frac{Z_A}{r_{iA}} + V_{HF}(i) \qquad \textbf{2.18}$$

where the first term describes the kinetic energy and the second term the electrostatic attractive potential between the electrons and nuclei. The final term is the Hartree-Fock potential which is the electronic repulsive potential. Since the Fock operator is a one-electron operator, it is a simplification over the two-electron operator, $\hat{V}_{ee}$, of the Hamiltonian in equation 2.4. The Hartree-Fock potential is given by,

$$V_{HF}(\vec{x}_1) = \sum_j^N \left(\hat{J}_j(\vec{x}_1) - \hat{K}_j(\vec{x}_1) \right) \qquad \textbf{2.19}$$

where $\hat{J}$ and $\hat{K}$ are the Coulomb and exchange operators, respectively. The Coulomb operator is the electronic repulsive potential experienced by an electron at $\vec{x}_1$ as a result of another electron described by the spin-orbital function, $\chi_j(\vec{x}_2)$, and is given by,

$$\hat{J}_j(\vec{x}_1) = \int |\chi_j(\vec{x}_2)|^2 \frac{1}{r_{12}} d\vec{x}_2 \qquad \textbf{2.20}$$

The exchange operator is related to the antisymmetric property of the wave function and does not have a classical interpretation analogous to the Coulomb operator. It is given by,

$$\hat{K}_j(\vec{x}_1)\chi_i(\vec{x}_1) = \int \chi_j^*(\vec{x}_2) \frac{1}{r_{12}} \chi_i(\vec{x}_2) d\vec{x}_2 \chi_j(\vec{x}_1) \qquad \textbf{2.21}$$

As the name suggests, in the exchange operator the components of the spin-orbital functions are exchanged. It acts as a correction to the Coulomb operator which doesn't take into account the antisymmetric character of the wave function. If the spins on the electrons described by the exchange operator are antiparallel the expression will be zero since spin functions are orthonormal, as mentioned previously. Therefore, only electrons of the same spin contribute to the exchange potential. When $i = j$, the Coulomb integral gives a potential for the interaction with the electron with itself. The Coulomb and exchange integral are equal in this case and therefore exactly cancel in equation 2.19. Thus, there is no self-interaction energy in HF theory.

The above equations are constructed from the spin-orbital functions of the Slater determinant and used to obtain the expectation value of the Hamiltonian and therefore the Hartree-Fock energy. They are solved iteratively, until the energies are unchanged to within a chosen value, referred to as the self-consistent field (SCF) method. Since the

Hartree-Fock equations are non-linear, they are difficult to solve for systems containing more than two atoms.

2.9.2 The Roothaan-Hall Equations

In 1951, Roothann[27] and Hall[28] independently proposed the idea of representing the spin-orbital functions, χ, as linear combinations of atomic orbitals (LCAO). These atomic orbitals are one-electron functions and are also termed basis functions, φ. It should be noted that the spin-orbital functional are often referred to as molecular orbitals. This made the computation of accurate wave functions viable for polyatomic systems and can be represented as,

$$\chi_i = \sum_{\mu=1}^{b} c_{\mu i} \varphi_\mu \qquad \textbf{2.22}$$

where $c_{\mu i}$ is the expansion coefficient for the basis function φ_μ that represents the molecular orbital χ_i and a basis set consisting of b basis functions construct the molecular orbital. In order to obtain an exact representation of the molecular orbital, a basis set composed of an infinite number of basis functions would be required. In practice an infinite set cannot be employed. Nonetheless, through careful selection of the expansion coefficients and a reasonably large, finite basis set, the molecular orbital can be obtained with negligible error.[12]

Substitution of equation 2.22 into the Hartree-Fock equation, equation 2.17, and application of the concepts of the variational theorem yields the Roothaan-Hall equations,

$$\sum_{\mu=1}^{b} c_{\mu i} \left(F_{\nu\mu} - \varepsilon_i S_{\nu\mu} \right) = 0 \qquad \nu = 1, 2, \ldots, b \qquad \textbf{2.23}$$

where $S_{\nu\mu}$ is the overlap integral between basis functions φ_ν and φ_μ, ε_i is the orbital energy of χ_i and the $\hat{F}_{\nu\mu}$ represents the Fock operator, expressed in terms of basis functions. The Fock matrix elements are defined by,

$$\hat{F}_{\nu\mu} = H_{\nu\mu}^{core} + \sum_{\sigma=1}^{b}\sum_{\gamma=1}^{b} D_{\sigma\gamma}\left[(\nu\mu\,|\,\sigma\gamma) - \frac{1}{2}(\nu\gamma\,|\,\sigma\mu)\right] \qquad \textbf{2.24}$$

where $H_{\nu\mu}^{core}$ is the core Hamiltonian, containing the one-electron elements of $\hat{T}$ and $\hat{V}_{ne}$, and $D_{\sigma\gamma}$ denotes the density matrix elements described by,

$$D_{\sigma\gamma} = 2\sum_{i=1}^{n/2} c_{\sigma i}^{*} c_{\gamma i} \qquad \sigma = 1, 2, ..., b \ , \ \gamma = 1, 2, ..., b \qquad \textbf{2.25}$$

The two-electron repulsion integral, denoted $(\nu\mu\,|\,\sigma\gamma)$, describes the Coulombic repulsion and can be expanded in terms of the basis functions such that,

$$(\nu\mu\,|\,\sigma\gamma) = \int\int \frac{\varphi_\nu^{*}(1)\varphi_\mu(1)\varphi_\sigma^{*}(2)\varphi_\gamma(2)}{r_{12}} d\upsilon_1 d\upsilon_2 \qquad \textbf{2.26}$$

The calculation of the two-electron integrals is very computationally expensive, since there are approximately N^4 six-dimensional integrals, representing a significant computational bottleneck. Analogous to the Hartree-Fock equations, the Roothaan-Hall equations must be solved iteratively using the self-consistent field method. An initial set of orbital coefficients must be chosen and recalculated from the Fock matrix until consistent.

2.9.3 *Restricted and Unrestricted Hartree-Fock Methods*

The spin-orbital functions comprising the Slater determinant are defined as the product of the position and spin functions, as discussed in section 2.5. If the system has

an even number of electrons, and all electrons are paired, it is referred to as a closed-shell system. Closed-shell systems are treated with the restricted Hartree-Fock (RHF) method which confines two electrons of opposite spin to each orbital.

For open-shell systems, where unpaired electrons are present, either restricted or unrestricted methods can be employed. The restricted open-shell Hartree-Fock (ROHF), similar to RHF, confines two electrons of opposite spin to each orbital and assigns unpaired electrons to singly occupied orbitals. Unrestricted Hartree-Fock (UHF) assigns different orbitals for each electron. In other words, all electrons, of either α-spin or β-spin, are in different orbitals and their energies are allowed to vary. The three methods are depicted in Figure 2.1.
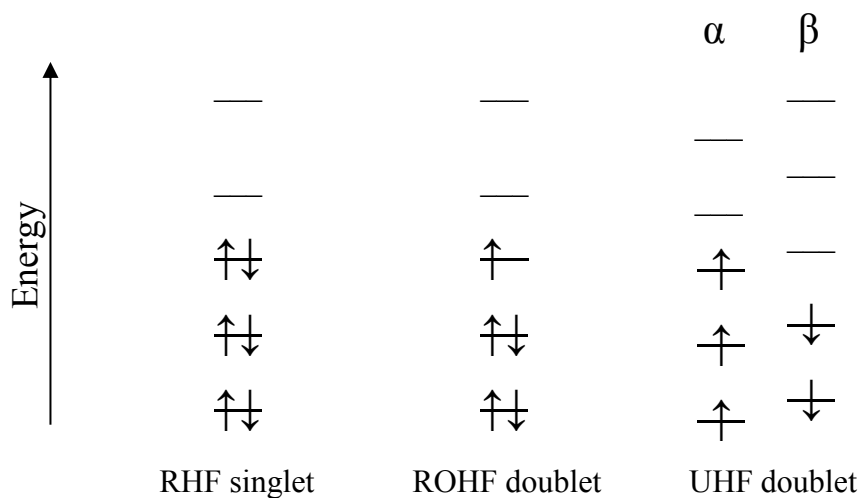
Figure 2.1. A representation of the orbital energies for a singlet using the RHF method and a doublet using the ROHF and UHF methods.

The energy of the UHF wave function is always lower than or equal to the energy computed using a restricted method. A disadvantage of UHF is that the Slater determinants used to compute the wave function are not eigenfunctions of the total spin operator and thus spin contamination can occur. A wave function that is spin

contaminated has higher spins states contributing to the total energy. Despite this drawback, UHF is the most frequently employed method in HF and post-HF methods.

2.10   Basis Sets

A basis set is a collection of basis functions, φ_μ, that represent a molecular orbital, χ_i. In general, both the accuracy and computational expense increases as the number of basis functions comprising the basis set increases. However, it is possible to obtain better accuracy with fewer basis functions if the particular basis set better represents the orbital. Consequently, the ultimate goal when selecting a basis set is to find a balance between these parameters.

2.10.1 Slater-Type Orbitals and Gaussian-Type Orbitals

The basis functions most commonly employed to construct basis sets are Slater-type orbitals (STOs) and Gaussian-type orbitals (GTOs). STOs were the first proposed basis functions[29] and have the general form,

$$\varphi^{STO} = \text{N} \; Y_l^m(\theta,\phi)r^{n-1}e^{-\zeta r} \qquad\qquad \textbf{2.27}$$

where N is the normalization constant, $Y_l^m(\theta,\phi)$ is the spherical harmonic function describing the angular distribution and $r^{n-1}e^{-\zeta r}$ is the exponential function describing radial distribution, where ζ is the orbital exponent. The orbital exponent controls the size of the orbital. The values of m, l and n are the magnetic, angular momentum, and principal quantum numbers, respectively, corresponding to the orbital being described. STOs represent reasonable approximations of atomic orbitals, however they are computationally expensive since the resulting integrals must be computed numerically. This is because STOs have a discontinuity, or cusp, at each nucleus, which results from

20

the $e^{-\zeta r}$ term of the function. In short, due to the high computational expense, STOs are typically only applied to small, highly symmetric systems.

GTOs were later proposed[30] as a less computationally demanding alternative and thus are more commonly employed over STOs. Their integrals are simpler to evaluate because they do not have a cusp, but are instead continuous at the nucleus. GTOs have the general form,

$$\varphi^{GTO} = N \; Y_l^m(\theta,\phi) r^{2n-2-l} e^{-\zeta r^2} \tag{2.28}$$

where the exponential function describing the radial distribution differs from STOs causing GTOs to decay rapidly as they move away from the nucleus, unlike the correct asymptotic behaviour of STOs. These characteristics can be seen in Figure 2.2. The GTO can be represented in Cartesian coordinates, for a GTO centred at a, as follows:

$$\varphi^{GTO} = N \; x_a^i y_a^j z_a^k e^{-\zeta r^2} \tag{2.29}$$

where x, y and z are Cartesian coordinates and i, j and k are nonnegative integers whose sum correspond to the angular momentum quantum number l.

To represent an orbital with the same level of accuracy achieved from a single STO, a combination of at least three GTOs is required.[31] Key to the efficiency of GTOs is that the product of two GTOs is another GTO, thus the two-electron integrals are much easier and faster to evaluate. Although, at least three GTOs are required to reach the same level of accuracy as a single STO even at this ratio, GTOs are much less computationally demanding.[7] Generally, GTOs represent a better compromise between accuracy and computational expense.
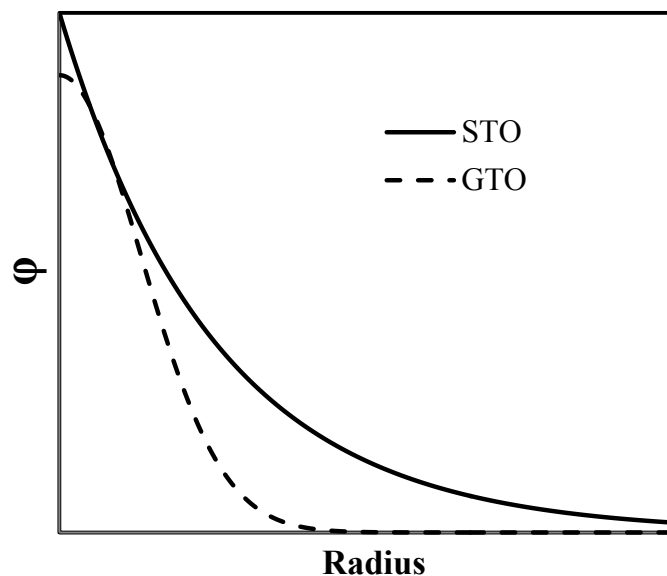
Figure 2.2. Comparison of the general form of a Stater-type (STO) and Gaussian-type orbital (GTO).

A linear combination of GTOs is referred to as a contracted Gaussian function (CGF) and is defined as,

$$\varphi_\tau^{CGF} = \sum_u d_{u\tau} \varphi_u^{GTO} \qquad\qquad \textbf{2.30}$$

where φ_τ^{CGF} is a contracted basis function, $d_{u\tau}$ is the fixed contraction coefficient and φ_u^{GTO} represents the set of GTOs that compose the CGF which differ only by their orbital exponents. A single GTO is referred to as a primitive GTO. Typically, three to six primitive GTOs are used to construct a CGF.

2.10.2 Minimal Basis Set

A minimal basis set uses only one STO or CGF to represent each atomic orbital of an atom. For example, when using a minimal basis set a single 1s basis function would represent a hydrogen atom and five basis functions would represent a carbon atom: 1s; 2s; $2p_x$; $2p_y$; and $2p_z$. Minimal basis sets can yield good starting geometries but generally

are not adequate since they are not flexible enough to accurately describe the electron distribution. A minimal basis set is referred to as a single-zeta basis set, often denoted single-ζ basis set, to represent the orbital exponent of a basis function.

2.10.3 Split Valence Basis Sets

Split valence basis sets are extended basis sets, where more than one STO or CGF, with varied orbital exponents, are used to describe the valence orbitals. Chemical bonding occurs between valence orbitals, while core orbitals are essentially independent of their chemical environment. Thus, generally valence orbitals are of more chemical interest. Since a split basis set has two or more functions, differing in size or radial distribution, there is more flexibility to better describe the orbitals environment. Although any basis set can be split, typically only the valence orbitals are split to provide a better description since they are typically more chemically relevant. This means that core orbitals are represented by a single basis function, and the valence orbitals are represented by two or more basis functions. For example, in the 3-21G basis set, core orbitals are represented by one CGF, which is a linear combination of three primitive GTOs, and valence orbitals are represented by two basis functions: one CGF that is a linear combination of two primitive GTOs and one primitive Gaussian function.

A basis set where the valence basis functions have been split into two basis functions, each comprised of a number primitive GTOs is called a double- ζ basis set. If the valence basis function has been split into three basis functions it is called a triple- ζ basis set, and so forth.

2.10.4 Polarization Functions

The addition of polarization functions to a basis set increases the flexibility of the orbital. Polarization functions are basis functions with higher angular momentum than the occupied orbitals already present. Adding these functions increases the accuracy of the basis set since the orbitals have increased flexibility allowing them to generate an improved representation of the electron distribution.

Consider a hydrogen atom with s-type orbitals, whose functions have spherical symmetry. The electron distribution of a hydrogen atom, particularly in a molecular system, is rarely spherical. Thus, the addition of p-type functions allows the orbital to distort to a more accurate portrayal of the electron distribution. Similarly any number of higher-order angular momentum functions can be added to the atoms of a system.

In Pople-type basis functions[32,33] the inclusion of polarization functions can be represented by either a '*' or by indicating the added functions in parentheses. A single '*' infers a single set of polarization functions are added to all non-hydrogen atoms, while a double '*' infers polarization functions are added to all atoms. As such, 6-31G** and 6-31G(d,p) are analogous for systems containing atoms in the first three rows of the periodic table. Multiple polarization functions can be added by specifying the number followed by the type of polarization function. For example, in the 6-311G(3d,2p) basis set two sets of p-type orbitals are added to hydrogen atoms and three sets of d-type orbitals are added to atoms in the system from the first three rows of the periodic table. In addition to Pople-type basis sets, Dunning[34,35] and Ahlrichs[36,37] basis sets are also widely used.

2.10.5 Diffuse Functions

Diffuse functions are added to a basis set to increase its radial distribution. This allows orbitals to extend further from the nucleus, again increasing the flexibility of the basis set. The inclusion of diffuse functions is especially important when describing systems such as anions, excited states, systems at non-equilibrium geometries where bonds are stretched or other weakly bound systems involving intermolecular interactions such as hydrogen bonding, since the electrons are less tightly bound.

In Pople-type basis functions[32,33] the inclusion of diffuse functions is denoted by a '+', as in 6-31+G. A single '+' infers a diffuse function is added to all non-hydrogen atoms, while a double '+' infers diffuse functions are added to all atoms.

2.11 Electron Correlation

A result of the variational principle is that the Slater determinant delivers an approximate wave function which corresponds to an energy, E_{HF}, that is greater than the exact energy, E_0. This discrepancy provides a measure of the error introduced by the Hartee-Fock approximation and is referred to as the correlation energy, E_C^{HF},

$$E_C^{HF} = E_0 - E_{HF} \qquad\qquad \textbf{2.31}$$

A significant portion of electron correlation arises because HF methods treat electron motion in an average way. This is not an accurate representation since electrons do not move completely independently of one another, but instead their motion is correlated, due to the effects of the instantaneous electron-electron repulsions. This effect is termed dynamical electron correlation. Non-dynamical, or static electron correlation represents the other contributor to electron correlation and is a result of a single Slater determinant

being used to describe the wave function, a result of the HF approximation. It is often referred to as left-right correlation and becomes a larger factor if the system exists in a degenerate or nearly degenerate state such that the system would be best described by multiple Slater determinants or as an atom deviates from the equilibrium bond distance, e.g. in bond dissociation. The magnitude of E_C^{HF} is often comparable to the energy of a chemical bond.[38] Thus, to accurately study most chemical systems, methods that account for electron correlation are essential.

Post-HF methods have been developed to deal with electron correlation. Some of the commonly used post-HF methods include: configuration interaction (CI); Møller-Plesset perturbation theory (MPPT); and coupled cluster approaches (CC). Some of these wave function based methods will be briefly discussed below, followed by a more significant discussion of another *ab initio* theory, density functional theory (DFT). DFT uses the electron density, as oppose to the wave function, as its central variable and is employed exclusively in this thesis.

2.11.1 *Configuration Interaction*

Configuration interaction (CI) is a variational method that includes electron correlation by approximating the wave function as a linear combination of Slater determinants, such that,

$$\Psi_{CI} = c_0 \Phi_{HF} + \sum_s c_s \Phi_s + \sum_d c_d \Phi_d + \sum_t c_t \Phi_t + ... + \sum_k c_k \Phi_k \qquad \textbf{2.32}$$

where the ground state determinant, Φ_{HF}, is combined with excited state determinants. The ground state determinant is the HF result and the subsequent terms of equation 2.32 denote the singly, doubly, triply and k^{th} excited determinants, respectively. The kth

determinant represents the excitation of all electrons. The expansion coefficients, c, are treated variationally to obtain the lowest energy wave function. The summation operator indicates that all possible excitations of that type are included. Theoretically, if an infinite basis set was employed and all possible electronic excitations were considered CI would yield the exact energy. However, in practice, a finite basis set and a limited number of electron excitations must be employed, for all but the smallest systems.

Thus, for computational feasibility, truncated CI methods are used. The configuration interaction singles (CIS) method includes all possible singly excited configurations. To instead include all double excitations, the configuration interaction double (CID) method is employed. The configuration interaction singles and doubles (CISD) method combines these, including all singly and doubly excited configurations. CI is a computationally expensive method. A CI method should be chosen such that it includes configurations with the largest contribution to the wave function.

2.11.2 Møller-Plesset Perturbation Theory

Perturbation theory includes electron correlation by approximating the real system to be the sum of the unperturbed system, or the HF result, and a perturbation. This method, proposed in 1934 by Møller and Plesset,[39] defines the Hamiltonian of the system, $\hat{H}$, to be,

$$\hat{H} = \hat{H}_0 + \lambda\hat{A}$$

2.33

where $\hat{H}_0$ is the unperturbed reference system and $\hat{A}$ is the perturbation. The value of the λ parameter varies from 0 to 1, corresponding to the strength of the perturbation. Substitution of the perturbed Hamiltonian into the Schrödinger equation gives,

$$(\hat{H}_0 + \lambda\hat{A})\Psi = E\Psi \qquad\qquad \textbf{2.34}$$

The perturbed wave function and energy can be expressed as a Taylor series,

$$\Psi = \lim_{n\to\infty} \sum_{i=0}^{n} \lambda^i \Psi^{(i)} \qquad\qquad \textbf{2.35}$$

$$E = \lim_{n\to\infty} \sum_{i=0}^{n} \lambda^i E^{(i)} \qquad\qquad \textbf{2.36}$$

respectively, where i denotes the order of the perturbation for that term. For example, the Taylor series is expanded to $n = 2$ to obtain a second-order perturbation, which corresponds to the MP2 method. A second-order, or higher, perturbation must be applied to obtain a correction to the HF energy. Although theoretically an infinite number of perturbations can be applied, in application a finite number must be selected. It has been shown that the majority of the correlation energy is recovered from a second-order perturbation method, and thus is a popular choice.[12]

Relative to HF or DFT, MP2 is a more computationally costly method, scaling with the fifth power of the system size.[10] Nonetheless, it represents one of the most computationally efficient perturbation methods. The coupled-cluster method is another perturbation method that includes electron correlation that will not be discussed here. Coupled cluster methods scales to the sixth to eighth power of the system size, depending on the types of excitations included in the method.

2.12   Density Functional Theory

Drawbacks of using wave function based methods are that they depend on $4N$ variables, corresponding to three spatial and a spin variable for each electron, where N is the number of electrons in a system and that the wave function is not an observable,

and therefore experimentally inaccessible. This makes the application of these methods restrictive due to the computational cost and thus, many systems are inaccessible with such methods. The major difference between density functional theory and other quantum chemical methods is that the electron density is implicitly used to obtain a solution to the Schrödinger equation, instead of the wave function. This makes intuitive sense given that: the integral of the density defines the number of electrons, N; cusps in the density define the position of the nuclei, r_A; and the ratio of the slope to the height of the cusps define the nuclear charge of these nuclei, Z_A.[40] The electron density, $\rho(\vec{r})$, is defined as the probability that an electron exists within a volume, $d\vec{r}$, and depends on only three spatial variables, regardless of the size of the system. The electron density can be represented as,

$$\rho(\vec{r}) = N \int ... \int \left| \Psi(\vec{x}_1, \vec{x}_2, ..., \vec{x}_N) \right|^2 d\vec{x}_1 d\vec{x}_2 ... d\vec{x}_N \qquad \textbf{2.37}$$

and is synonymous with the probability density.

Early work with the electron density was carried out by Thomas,[41] Fermi,[42] Dirac[43] and Slater.[44] This research is considered to be the precursor to modern density functional theory which was established from the work of Hohenberg, Kohn, and Sham.

2.12.1 Hohenberg-Kohn Theorems

A 1964 paper by Hohenberg and Kohn proposed two theorems that laid the theoretical framework for density functional theory.[45] The first theorem proves that the electron density uniquely determines the energy and thus all quantum mechanical properties of the system. As mentioned previously, the Hamiltonian operator can be determined from the expectation value of the electrostatic attractive potential felt by the

electrons from the nuclei, $\hat{V}_{ne}$, and the number of electrons in the system, N. In density functional theory the electrostatic attractive potential is referred to as the external potential and is denoted $\hat{V}_{ext}$. Hohenberg and Kohn proved that two distinct external potentials cannot yield the same ground state electron density, concluding that the electron density is a unique variable that contains all the information about the quantum mechanical properties of a system. A functional associates a number with a function, as oppose to a number with another number as a function does, and is denoted with square brackets. For example, $E_0[\rho_0]$ denotes the ground state energy of a system which is a functional of the ground state electron density.

The second Hohenberg-Kohn theorem is analogous to the variational principle and applies to the electron density. The theorem proof concludes that an electron density delivers the lowest energy only if it is the true ground state electron density, ρ_0.

2.12.2 The Universal Functional

From the first Hohenberg-Kohn theorem, the validity of employing the electron density as a central variable is affirmed. Given that the ground state energy of a system is a functional of the ground state electron density, it follows that the ground state energy can be represented as,

$$E_0[\rho_0] = T[\rho_0] + E_{ee}[\rho_0] + E_{ext}[\rho_0] \qquad \textbf{2.38}$$

where the terms comprising the total ground state energy are also functionals of the electron density. In the above equation the electronic kinetic energy and the electronic repulsive potential energy are denoted $T[\rho_0]$ and $E_{ee}[\rho_0]$, respectively. Both these terms are independent of the system and are said to be universal functionals. They are

independent of the system because they do not contain Z_A, r_A or N. These terms are collected into what is known as the universal functional, $F[\rho_0]$, that is defined as,

$$F[\rho_0] = T[\rho_0] + E_{ee}[\rho_0] = \left\langle \Psi \middle| \hat{T} + \hat{V}_{ee} \middle| \Psi \right\rangle \qquad \textbf{2.39}$$

The electron-electron interaction term, $E_{ee}[\rho_0]$, can be further broken into the known classical Coulomb contributions, $J[\rho_0]$, and the unknown non-classical contributions, $E_{ncl}[\rho_0]$, which include the self-interaction correction as well as exchange and Coulomb correlation effects. Therefore, the universal functional can be written as,

$$F[\rho_0] = T[\rho_0] + J[\rho_0] + E_{ncl}[\rho_0] \qquad \textbf{2.40}$$

The explicit form of the universal functional is unknown and represents a significant challenge in density functional theory. The final term of equation 2.38, is the external potential energy, or the energy due to the attraction between the nuclei and electrons. It does depend on the system and is independent of the wave function since it can be obtained from only the electron density. The total ground state energy can therefore be written as,

$$E_0[\rho_0] = F[\rho_0] + \int \rho_0(\vec{r}) V_{ext} d\vec{r} \qquad \textbf{2.41}$$

From this expression the ground state wave function is connected to a chosen electron density. However, although the Hohenberg-Kohn theorems validate the theoretical framework of density functional theory, they have no practical use since they do not provide any information about the composition of the universal functional. More specifically, the second Hohenberg-Kohn theorem applies only to the exact universal functional and since it is unknown it does not have practical application. This can result in energies lower than the exact energy being computed from density functional methods.

2.12.3 Kohn-Sham Theorem

The next major contribution to density functional theory came the following year, in 1965, from a paper by Kohn and Sham.[46] In this paper a way to approximate the universal functional is presented. Kohn and Sham did this by first recognizing that the most significant difficultly encountered by orbital-free methods is the inadequate representation of the kinetic energy term. They addressed this issue by using orbitals to construct a non-interacting system for which the kinetic energy can be computed exactly. For this task, a Slater determinant is employed, since it represents the exact wave function of a non-interacting system that is moving in an effective potential. Analogous to equation 2.17 of the Hartree-Fock approximation, the spin orbitals of the Slater determinant are determined by,

$$\hat{f}^{KS}\phi_i = \varepsilon_i^{KS}\phi_i \qquad\qquad 2.42$$

where $\hat{f}^{KS}$ denotes the Kohn-Sham (KS) operator, ϕ denotes the KS orbitals and ε_i^{KS} denotes the KS orbital energy. The one-electron KS operator is defined as,

$$\hat{f}^{KS} = -\frac{1}{2}\nabla^2 + V_S(\vec{r}) \qquad\qquad 2.43$$

where V_S is the effective local potential which is chosen such that the density of the model, non-interacting system, $\rho_S(\vec{r})$, is equal to the density of the real, interacting system, $\rho_0(\vec{r})$. Thus,

$$\rho_S(\vec{r}) = \sum_i^N \sum_s |\phi_i(\vec{r},s)|^2 = \rho_0(\vec{r}) \qquad\qquad 2.44$$

This condition connects the real and model systems, and allows for a significant portion of the kinetic energy, denoted T_S, to be calculated exactly. To incorporate this kinetic energy term, Kohn and Sham redefine the universal functional as,

$$F[\rho] = T_S[\rho] + J[\rho] + E_{XC}[\rho]$$
2.45

where $E_{XC}[\rho]$ is introduced as the exchange-correlation energy and is equal to,

$$E_{XC}[\rho] = (T[\rho] - T_S[\rho]) + (E_{ee}[\rho] - J[\rho]) = T_C[\rho] + E_{ncl}[\rho]$$
2.46

In other words, the remaining part of the kinetic energy, T_C, is added to the non-classical electrostatic contributions. This exchange-correlation term represents all the unknown components of the universal functional. It follows, via the variational principle, that the exact form of the KS operator can be expressed as,

$$\hat{f}^{KS} = -\frac{1}{2}\nabla^2 + \int \frac{\rho(\vec{r}_2)}{r_{12}} d\vec{r}_2 + V_{XC}(\vec{r}_1) - \sum_A^M \frac{Z_A}{r_{1A}}$$
2.47

where V_{XC} is the potential due to the exchange-correlation energy and the functional derivative of E_{XC} with respect to the density,

$$V_{XC} = \frac{\delta E_{XC}}{\delta \rho}$$
2.48

The KS orbitals are obtained iteratively and then used to determine the ground state density and energy. If all the functionals were known exactly, the KS equations would yield the exact energy of the system. The only approximation made in the KS method is the functional used to describe the exchange correlation energy and corresponding potential. It remains a central goal of density functional theory to develop approximations for the unknown exchange-correlation functional.

2.12.4 Exchange-Correlation Holes

The exchange-correlation energy can be separated into the exchange and the correlation contributions. These are easy to conceptualize as holes in the electron density. The exchange energy hole conveys that the probability of having two electrons of parallel spin at the same position is zero. Thus, the exchange hole generates a hole in the electron density surrounding the electron with a volume equal to the charge of the electron,

$$\int h_X^\sigma(\vec{r},\vec{r}')d\vec{r}' = -1 \qquad \textbf{2.49}$$

and with a depth equal to,

$$h_X^\sigma(\vec{r}=\vec{r}') = -\rho_\sigma(\vec{r}) \qquad \textbf{2.50}$$

where $\vec{r}$ is the position of the electron with spin σ, $\vec{r}'$ is a vector that defines the distance from the electron and ρ_σ is the total electron density of spin σ. Equations 2.49 and 2.50 represent the self-repulsion correction and exchange repulsion, respectively. The shape of the hole changes such that in areas of increased electron density the hole is deeper, and more diffuse in areas of lower electron density.

The correlation hole is also centered on each electron but influences electrons of both same and opposite spin. The correlation hole satisfies,

$$\int h_C(\vec{r},\vec{r}')d\vec{r}' = 0 \qquad \textbf{2.51}$$

The consequence of the correlation hole is that the exchange-correlation hole becomes deeper than $-\rho_\sigma(\vec{r})$ since opposite spin electrons are also being repelled. Ultimately, the exchange-correlation energy is calculated by,

$$E_{XC} = \frac{1}{2} \iint \frac{\rho_0(\vec{r}) h_{XC}(\vec{r},\vec{r}')}{|\vec{r}'-\vec{r}|} d\vec{r} d\vec{r}'$$

2.52

In practice spherical model holes are often used and are sufficient to calculate accurate energies. The approach used to model the exchange-correlation hole has led to many different exchange-correlation functional approximations. Three major types, as well as some general approaches to developing approximate exchange-correlation functionals, will be discussed.

2.12.5 Exchange-Correlation Functional Approximations

The quality of a density functional method relies directly on the quality of the approximation used for the exchange-correlation density functional approximation, often referred to as density functional approximations (DFAs) or more simply functionals. Thus, DFT hinges on the ability to approximate the exchange-correlation functional, for which the exact form is unknown. As previously mentioned, the exchange-correlation functional contains all the unknown elements of the system's energy. It incorporates the non-classical portion of the electron-electron interactions, the correction for self-interaction and the part of the kinetic energy not accounted for by the non-interacting reference system.

Failures of DFT to predict the correct energy or properties of a system are the fault of the approximate form of the exchange-correlation functional. Unfortunately, there is no systematic methodology that points to this functional. Without a systematic approach, the field is instead advanced by "relying on many little bits of information about the true functional and compensating for lack of mechanical recipes with insight and ingenuity."[47] Consequently, a range of approaches are taken in the development of

new density functional approximations. The most prevalent strategies are reviewed in reference 47 and are summarized here:

A. Local-density approximation (LDA) and local-spin-density approximation (LSDA) - The exchange-correlation functional is defined such that it depends only on the electron density. The functional is designed to satisfy the conditions of a uniform electron gas and then locally applied to the non-uniform densities of chemical systems.

B. Density-gradient expansion - The exchange-correlation functional is expanded to include electron density and gradients of the electron density. These are known as generalized gradient approximations (GGA).

C. Constraint satisfaction - Design of the functional form of the exchange-correlation functional is based on the known behaviour of the true functional. In general, this approach is combined with other strategies listed here and may involve semiempirical corrections to the gradient terms or be entirely nonempirical. It has been a very successful method for the development of new functionals.

D. Modelling the exchange-correlation hole - This is the most popular approach and yields the most diverse group of functionals. The exchange-correlation hole can be modelled with respect to the electron density, the gradient, the Laplacian and the kinetic energy density. This approach may produce functionals that contain empirical parameters or may generate nonempirical descriptions. These types of functionals are known as meta-generalized gradient approximations (meta-GGA) if they employ the kinetic energy density.

E. Empirical fits - This method employs experimental data in the form of large data sets, to optimize the functional form. The result is empirical parameterization of adjustable parameters within the functional. The functional can be of any form, or a linear combination of multiple functional forms.

F. Mixing Hartree-Fock (HF) exchange and DFT approximate exchange - This method adds some degree of HF exchange to the functional form. The goal is to include nonlocal exchange, which is difficult to model in the functional form since it is composed of local variables such as density, the gradient of the density, the Laplacian and the kinetic energy density. These density functionals are known as hybrid functionals.

These methods will be discussed further in the following section. Also, it should be noted that this list is not all-inclusive; for example, the double-hybrid method is a strategy that adds second-order perturbation theory, to more accurately model correlation, to the hybrid functional form discussed above.[48] It should be noted that strategies are often used in combination with one another. For example, an approach that aims to model the exchange-correlation hole may contain parameters fitted to experimental data sets, employing strategies D and E.

2.12.6 Types of Exchange-Correlation Functional Approximations

There are three main categories of exchange-correlation density functional approximations: local density and local spin density approximations; generalized gradient approximations; and hybrid functionals.

The local density approximation (LDA), or in spin polarized systems, the local spin-density approximations (LSDA) assumes that the exchange-correlation energy

locally depends solely on the electron density. These methods yield accurate geometries and slightly overestimated covalent and ionic bond energies, but do not accurately describe hydrogen bonds.[49–51] They also fail to give accurate molecular energies. LDA and LSDA provide accurate results for systems that closely resemble a uniform electron gas, such as systems with only slight variation in electron density with position. These methods are primarily used in the field of physics to describe extended systems that fit a uniform electron gas model.[52]

The generalized gradient approximation (GGA) uses a functional that depends on the density and its first derivative, the gradient of the density. In GGA methods, the exchange-correlation functional is broken into an exchange contribution and correlation contribution. Various exchange and correlation functionals exist and are combined to form a complete density functional theory method. Accurate geometries and energies can be obtained from GGA methods, and thus represent a substantial improvement over LDA and LSDA methods. One of the most popular exchange functionals was developed by A. D. Becke and is abbreviated as B88 or, perhaps more often, as B.[53] A popular correlation functional, denoted LYP, was proposed by C. Lee, W. Yang and R. G. Parr in the same year.[54] These two functionals can be combined to yield the BLYP exchange-correlation functional, employed in studies found in this thesis.

Another popular type of exchange-correlation functional incorporates Hartree-Fock exact exchange and is referred to as a hybrid functional. A widely used hybrid exchange-correlation functional is B3LYP, which combines the Becke three-parameter exchange functional (B3), developed by A. D. Becke,[55] with the LYP correlation functional mentioned above. This functional is defined as,

$$E_{XC}^{B3LYP} = (1-a)E_X^{LSDA} + aE_X^{HF} + b\Delta E_X^{B88} + (1-c)E_C^{LSDA} + cE_C^{LYP} \qquad \textbf{2.53}$$

where a, b and c are semiempirical coefficients that vary the contributions of each parameter. The B3LYP exchange-correlation functional is employed in Chapters 3 and 4 of this thesis.

2.13   Dispersion

The notion that atoms do not influence one another at large internuclear or intermolecular distances and strongly repel one another at short distances is a straightforward concept. However, at intermediate distances they can slightly attract one another. This is because the motion of the electrons can generate an uneven electronic distribution in atoms causing an instantaneously induced multipole moment and momentary attraction between the atoms, even in the absence of a permanent dipole moment. This force is referred to as a dispersion, or London, force and is gievn by the inverse sixth power of the intermolecular distance.

Noncovalent interactions, or noncovalently bound complexes frequently involve dispersion interactions. Dispersion is the result of long-range correlation effects and, as such, cannot be described by many popular density functional approximations. Many functionals only account for local or semilocal effects, also referred to as short and medium-range correlation. There are various approaches to account for the description of dispersion interactions that can be generalized into two categories: developing a new functional form that includes physical terms to model dispersion, and adding dispersion correction terms empirically to an existing functional form. The first approach can be acheived by including non-local terms in the functional form[56,57] or effective core potential[58] or the dispersion interaction can be described by the dipole moment induced

by an electron and its exchange hole.[59–63] Adding empirical, or semiclassical, dispersion terms to a density functional approximation adds negligible computational expense, since only interactions between atomic centres are required, and are often referred to as DFT-D methods. The most popular method of this type was proposed by Grimme and employs an R^{-6} term, where R is the interatomic distance, along with a dispersion coefficient constant, and a damping function to correct the interaction at short-range.[64–66] This approach provides the correct dependence of the dispersion energy on the interatomic distance modified by empirical coefficients.   A recent improvement to the DFT-D method, known as DFT-D3, uses theoretical data to optimize the coefficients of the dispersion correction and thus is considered to be nonempirical in nature.[66]

It should be noted that some density functional approximations are parameterized with test sets that include dispersion interactions. These functionals, notably M05-2X and M06-2X, are recommended by their developers as functionals that account for dispersion interactions.[67,68] It is important to note that these functionals do not include a physical description of dispersion nor do they include a London-type R^{-6} dispersion term.

A detailed discussion of DFT methods that include dispersion is beyond the scope of this thesis. For a comprehensive review of this topic see reference 69. Within this thesis, a number of density functional approximations are employed that account for dispersion interactions, including M06-2X, BLYP-D, B3LYP-D, B97-DB97-D and ωB97X-D. These functionals account for dispersion interactions by including empirical dispersion terms.

2.14   Techniques for Geometry Optimization

Exploration of the potential energy surface for a molecular system is perhaps the most powerful tool in computational chemistry. The changes in geometry and energy that happen as a molecular system undergoes a chemical change are at the foundation of chemical phenomena. There are numerous algorithms that can be employed to find a local minimum in total energy. The Berny geometry optimization algorithm is the default method implemented in the popular computational chemistry software Gaussian.[70] The method is based on a program written by H. B Schlegel.[71] In essence, the geometry of the molecule is systematically modified until an energy minimum, to within a criterion determined by the user, is obtained. This process is referred to as geometry optimization or energy minimization. The local minimum is determined with respect to initial molecular coordinates inputted by the user. These may be generated from an experimentally determined structure, such as from X-ray crystallographic data or chemical intuition based on typical bond lengths for atoms or analogous molecules. The closer the starting geometry is to the minimum energy geometry, the fewer number of necessary iterations, thus making the calculation faster. Frequently, the global minimum structure is desired, thus geometry optimizations of various conformations of the molecule must be performed. In general, the more atoms involved in a system, the larger number of local minima present along the potential energy surface, thus careful consideration of various conformations is essential.

In addition to the local and global minima on a potential energy surface, the saddle points that connect the minima and transition state structures are also often of interest. These saddle points are minima along the potential energy surface in all

coordinates, except one, the reaction pathway. Mathematically, this corresponds to one negative eigenvalue in the Hessian matrix, the matrix of the second derivatives of the energy, also known as the force constant matrix. The negative eigenvalue manifests as an imaginary vibrational frequency for the molecular system.

2.15   The Quantum Theory of Atoms in Molecules

The quantum theory of atoms in molecules (QTAIM)[72–74] exploits information that can be obtained from the electron density of a system to explain and understand experimental observations made in chemistry. More specifically, QTAIM employs the electron density, $\rho(r)$, using its topology to partition the molecular system into atomic regions. Analysis of the atomic regions allows for the characterization of bonding and various atomic properties.

In QTAIM, the central variable used for analysis is the electron density, $\rho(r)$. At the nuclei there exists a localization of electron density, a result of the attractive forces between the electrons and nucleus, which extends from the nucleus into the internuclear space. The equilibrium of the forces between the nuclei and surrounding electrons enables the partitioning of the molecule into atomic regions, or atoms in molecules. The boundaries of the atomic regions occur where the first derivatives of the electron density are zero, referred to as a zero-flux surface.

2.15.1 The Gradient-Vector Field and Critical Points

The charge density topology is analyzed by evaluating the gradient of the electron density, $\nabla\rho$, defined as,

$$\nabla\rho = \vec{i}\,\frac{\partial\rho}{\partial x} + \vec{j}\,\frac{\partial\rho}{\partial y} + \vec{k}\,\frac{\partial\rho}{\partial z} \qquad\qquad \textbf{2.54}$$

If the first derivatives of the density are zero, in other words, each term of the gradient in equation 2.54 is zero, a critical point is obtained. There are four types of critical points that characterize unique chemical components of a molecule: nuclear critical points (NCP); bond critical points (BCP); ring critical points (RCP); and cage critical points (CCP). A critical point is classified by assessing the second derivatives of the electron density at that point, r_c, shown in the form of a Hessian matrix,

$$A(\vec{r}_c) = \begin{pmatrix} \dfrac{\partial^2\rho}{\partial x^2} & \dfrac{\partial^2\rho}{\partial x\partial y} & \dfrac{\partial^2\rho}{\partial x\partial z} \\[2mm] \dfrac{\partial^2\rho}{\partial y\partial x} & \dfrac{\partial^2\rho}{\partial y^2} & \dfrac{\partial^2\rho}{\partial y\partial x} \\[2mm] \dfrac{\partial^2\rho}{\partial z\partial x} & \dfrac{\partial^2\rho}{\partial z\partial y} & \dfrac{\partial^2\rho}{\partial z^2} \end{pmatrix} \qquad\qquad \textbf{2.55}$$

To obtain the eigenvalues, the Hessian matrix is diagonalized and the trace of the matrix evaluated. This is the Laplacian of the density,

$$\nabla^2\rho(\vec{r}) = \frac{\partial^2\rho(\vec{r})}{\partial x^2} + \frac{\partial^2\rho(\vec{r})}{\partial y^2} + \frac{\partial^2\rho(\vec{r})}{\partial z^2} \qquad\qquad \textbf{2.56}$$

The critical points are classified by the nature of the three eigenvalues of the Hessian matrix, which describe the curvature of the density. More specifically, the critical points are characterized by two values, the rank and signature, denoted ϖ and ϑ, respectively. The rank is defined as the number of non-zero curvatures, or eigenvalues, and is equal to three in all types of critical points. The signature assigns a value of +1 to positive eigenvalues and -1 to negative eigenvalues, and is defined as the sum of these three values. The rank and signature corresponding to each type of critical point is shown in Table 2.1.

43

Table 2.1. Classification of critical point types.

Type of Critical Point	Rank and Signature, (ϖ, ϑ)
Nuclear critical point (NCP)	(3,−3)
Bond critical point (BCP)	(3,−1)
Ring critical point (RCP)	(3,+1)
Cage critical point (CCP)	(3,+3)

The composition of critical points within a molecule obey the topological rule such that,

$$n_{NCP} - n_{BCP} + n_{RCP} - n_{CCP} = 1 \qquad \textbf{2.57}$$

where n is the number of each type of critical point in a molecule or other isolated system. This property is known as the Poincaré-Hopf relationship. Its satisfaction is used as an indication of a successful analysis.

2.15.2 Electron Density at the Bond Critical Point

The magnitude of the electron density at the BCP provides a measure of the bond strength. More specifically, a larger electron density is associated with greater bond strength. The value of ρ at the BCP can be used to characterize the type of bonding. Typically, BCPs with an electron density above 0.20 are indicative of covalent bonding character while an electron density less than 0.10 signifies a closed-shell interaction. In QTAIM, a closed-shell interaction refers to non-covalent interactions such as ionic, hydrogen bonding or van der Waals interactions. This property is also reflected in the sign of the Laplacian, $\nabla^2 \rho$, at the BCP. Covalent and closed-shell interactions give negative and positive values for the Laplacian, respectively.

Analysis of the value of ρ at the BCP can be a powerful tool to assess bond strength within a molecule. Although bond lengths are often used to determine bond strength, this has proven erroneous in some cases which are discussed later in this thesis. Conventionally, bond strength is assessed by carrying out lengthy and often complicated bond dissociation calculations, however, QTAIM analysis allows for the comparison of the bonds within a molecule, often inaccessible via a bond dissociation calculation.

2.15.3 *Interatomic Surfaces and Bond Paths*

A zero-flux surface is a region of the electron density defined by,

$$\nabla \rho(\vec{r}) \cdot n(\vec{r}) = 0 \qquad \qquad \textbf{2.58}$$

where $n(\vec{r})$ is a unit vector orthogonal to the surface. These zero-flux surfaces define an atomic basin and occur between atoms involved in a bonding interaction. These boundaries result in a division of real space into atomic regions, where a nucleus and its associated atomic basin define an atom in a molecule. The electrons contained within an atomic basin can be obtained by integrating over the basin. For an atomic basin, A, this is defined by,

$$N(A) = \int_A \rho(r) dr \qquad \qquad \textbf{2.59}$$

where $N(A)$ is the number of electrons contained in the atomic basin of atom A, and the sum of all the atomic basins is the number of electrons in the molecule, N. This separation allows for the determination of various atomic properties that contribute to molecular properties, such as charge, volume, dipole moment and energy, by integration with the appropriate operator over the individual atomic basin.

Between nuclei that share a zero-flux surface, or bonded atoms, there exists a path of locally maximum electron density. This is defined as the bond path. The bond path crosses the zero-flux surface at the BCP, which is a local minimum of the electron density along the bond path.

2.15.4 Delocalization Indices

QTAIM involves the analysis of the topology of the one-electron density; however two-electron properties, based on the electron pair density, can also provide insight into chemical properties. The electron pair density, denoted $\rho(\vec{r}_1, \vec{r}_2)$, represents the probability of simultaneously finding an electron at $\vec{r}_1$ and $\vec{r}_2$, and contains information about electron correlation.[10,75] A two-electron property employed for analysis in this thesis is the delocalization index, denoted as δ. If atomic basins A and B are considered, the delocalization index provides a quantitative measure of the sharing of electrons between atoms A and B, and is defined as,

$$\delta(A, B) = -4D(A, B) + 2N(A)N(B) \qquad \textbf{2.60}$$

where $D(A, B)$ is the probability of simultaneously finding an electron in atomic basin A and another in atomic basin B. This property is obtained by integrating over the coordinates of one electron in the pair density over the atomic basin A and the coordinates of the other electron over atomic basin B, such that,

$$\textbf{2.61}$$
$$D(A, B) = \int_A d\vec{r}_1 \int_B d\vec{r}_2 \rho(\vec{r}_1, \vec{r}_2)$$

Depending on the density functional approximation employed, the delocalization index captures Coulomb correlation and the Hartree-Fock exchange, or Fermi

correlation.[72,74,76–78]   In other words, the delocalization index partitions the exchange-correlation density between atoms.

The delocalization index between bonded atoms provides a measure of bond order, since it is a measure of the number of electron pairs shared between them, and thus has considerable practical applications.[74]   It should be noted that since the electron-pair density is not defined within density functional theory the two-electron density is approximated.   It has been shown that the delocalization indices obtained via the KS orbitals slightly overestimate delocalization, or covalency, relative to those computed from the HF orbitals.[79]   Although not theoretically rigorous, the approximate delocalization indices derived from DFT methods have been shown to be useful tools for the analysis of the molecular electronic structures.[76–82]   The delocalization index is employed to analysis results in Chapter 4 of this thesis.

2.15.5 Criticisms of QTAIM

QTAIM is a density-based topological tool which allows for the study of chemical bonding and is one of the most well-known and most cited approaches to query the chemical bond.   The method exploits the large amount of information that can be obtained from the electron density of a system to explain and understand experimental observations made in chemistry.   Analysis of the topological features of the electron density allows for the characterization of chemical bonding and atomic properties such as charge, radius, volume, polarization, and atomic energy.   It is advantageous over molecular orbital based analyses since the understanding of a system does not depend on the way the wave function was obtained.   The underlying concepts of QTAIM are generally regarded as robust methods since the topology of the electron density and

associated bond paths can be obtained from experimental techniques such as X-ray energy dispersive techniques.

As with any method developed within the scientific community, QTAIM is subject to criticism. One of the most prevalent criticisms stems from the absence or presence of bond paths where chemical intuition would disagree. A full discussion of these criticisms is beyond the scope of this thesis; however, it is the opinion of the author that the definition of a chemical bond is too restrictive to encompass all the interactions between atoms and molecules. R. F. W. Bader, the developer of QTAIM, has emphasized that a bond path indicates chemical bonding and not a chemical bond, since its definition is not rigorous, nor rooted in quantum mechanics, in other words, there is no quantum mechanical operator for the chemical bond.[83,84] The work presented in this thesis does not employ QTAIM to define novel chemical bonding, but instead uses the QTAIM properties derived from the electron density to gain insight into the electronic properties of these systems which are largely regarded as robust.

Chapter 3 : The Effect of Multiplicity on the Size of Iron (II) and the Structure of Iron (II) Porphyrins

3.1 Introduction

Hemoglobin is an iron-containing metalloprotein found predominately in the red blood cells of vertebrates. Its ability to bind oxygen and to transport it throughout the body is of significant physiological importance. Oxygen is bound at the heme site, a nearly planar iron-containing porphyrin molecule, located in a hydrophobic pocket on each of the four sub-units of the protein.[86] Each heme group is coordinated to the protein by an amino acid, typically histidine, which acts as an axial ligand to the iron. The porphyrin nature of the heme group makes it a highly delocalized system, allowing electron and spin delocalization throughout the molecule.[87–89] The formation of many stable heme species with varying iron oxidation states in biological systems can be attributed to this effective delocalizing framework.[90]

The functionality of the hemoglobin protein is, in part, due to the structure of the high-spin state of the iron atom, the quintet state. The penta-coordinated heme site is domed[91] and when oxygen binds to the other axial position of the iron atom the heme group undergoes a conformational change. The iron atom moves into the porphyrin plane, from the original domed position, resulting in the movement of the histidine residue toward the porphyrin plane. This conformational change is transmitted through the peptide chain, resulting in a change of the tertiary structure and new binding

interactions which leads to a new quaternary structure. As a consequence, the heme binding site of the second deoxy subunit binds oxygen more favourably, resulting in a significant increase in affinity of hemoglobin for oxygen.[92] This effect is further strengthened as subsequent oxygen molecules bind to hemoglobin until all four heme groups are bound.[93] Although deoxyhemoglobin has a modest affinity for oxygen, this allosteric mechanism of hemoglobin, as well as the high oxygen pressure in the lungs makes hemoglobin an effective transporter of oxygen.

Consequently, the domed structure of the penta-coordinated iron has a key role in the functionality of the hemoglobin protein.[94,95] The original explanation for this geometry was based on X-ray structures[96,97] and assumed that the effect was a result of the high-spin state of iron being more spatially extended than the lower spin states, forcing the iron atom out of the plane. Later it was shown, both theoretically[98] and experimentally[99], that for isolated atoms or ions the high-spin state is spatially smaller than the low-spin state of an atom with the same charge and configuration. A more recent study has shown this to hold true for various spin states of iron (II).[100] This observation has been shown to be consistent with the quantum mechanical interpretation of Hund's multiplicity rule.[101] The valence electrons, or highest energy electrons, in higher spin states are unpaired and as a result experience less screening from the nucleus. This results in greater electron-nuclear attraction and thus a smaller atomic size. Despite these more recent studies disproving the earlier assumption, it is still often stated that the larger atomic radius of high-spin iron forces it out of the porphyrin plane.[102–106]

In this study, the quantum theory of atoms in molecules (QTAIM)[72–74] is used to investigate the atomic volume of iron within the porphyrin environment. Five spin states

of Fe^{2+} are considered, $2S + 1 = 1, 3, 5, 7$, and 9, which correspond to the singlet, triplet, quintet, septet and nonet states, respectively. The QTAIM method defines the volume of an atom in a molecule as the space bound by zero-flux surfaces and a chosen outer isodensity envelope. Typically, an isosurface of $\rho = 0.001$ au is used since it generally contains more than 99% of the electrons and closely reproduces the experimental van der Waals volumes in the gas phase.

3.2   Computational Methods

All calculations employed density functional theory using the B3LYP functional and were performed with Q-Chem, version 3.1.[107] Density functional theory is widely used due to its high efficiency for large systems. The B3LYP density functional approximation combines Becke's three-parameter hybrid exchange functional with the Lee-Yang-Parr correlation functional and has been shown to be an adequate computational method for the study of heme models[102,103,108,109] and other iron containing systems.[110,111] Consequently, it is an appropriate method for this investigation.

Preliminary calculations, including the potential energy surface, were completed using the 6-31G(d) basis set, to ensure consistency with the previous study by Ugalde *et al.*[100] The optimized structures were used as starting geometries for calculations with a higher basis set to reduce computational time. These calculations were performed using a mixed basis set. The 6-31G(f) basis set was used for iron and all other atoms were treated with the 6-311G(d,p) basis set. Atomic properties of iron and bond critical points (BCPs) were computed using AIMAll.[112] Molecular graphs depicting the critical points were computed using AIM2000.[113]

51

This study considers the singlet, triplet, quintet, septet and nonet states of iron (II), iron (II) porphine and iron (II) porphine ligated by imidazole in the axial position. The structures are abbreviated as Fe^{2+}, FeP and FePIm, respectively. Porphine, the simplest porphyrin, is used in these molecules as a model for the heme group. Figure 3.1 displays a ball-and-stick model of the FePIm model system. The Fe^{2+} atom has a d^6 electronic configuration, thus it is reasonable to assume that d-orbitals are involved in the coordination of iron to the porphine ring and any axial ligands. Imidazole was selected because it mimics the histidine residue that binds the heme group in hemoglobin.[93,95,100] The porphyrin framework is otherwise unligated since it is sufficient to model the environment of the iron atom. No symmetry constraints were assumed. Frequency calculations on the optimized geometries were performed to confirm that no imaginary frequencies were present and that the geometries obtained are local minima.
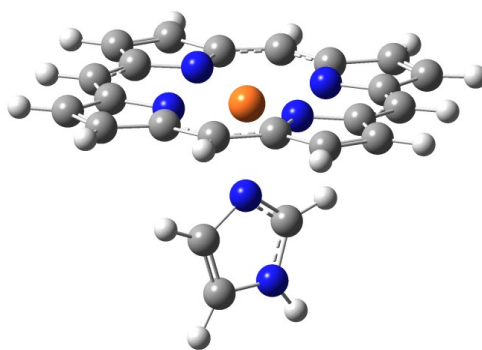
Figure 3.1. Molecular structure of FePIm shown in ball and stick format. Carbon, nitrogen and hydrogen atoms are shown as grey, blue and white spheres, respectively. The iron atom is shown in orange.

3.3   Results and Discussion

3.3.1   *Potential Energy Surfaces*

To ensure the global minima were located, a relaxed potential energy surface for each spin state was computed by varying the degree of rotation of the imidazole group

relative to the porphyrin. The spin states closest in energy are the singlet, triplet and quintet states. These states are of most interest because they are lowest in energy and have physiological relevance.[4] The potential energy surfaces for these states are shown in Figure 3.2. The septet and nonet states of FePIm are significantly higher in energy, approximately 28 kcal·mol^{-1} and 69 kcal·mol^{-1}, respectively. A 0° rotation, as shown in Figure 3.2a, is defined to be when the plane of the imidazole group eclipses two of the nitrogen atoms of the porphyrin ring and a 45° rotation, as shown in Figure 3.2b is defined to be when the plane of the imidazole group is located between the nitrogen atoms of the porphyrin ring. The lowest energy configurations were then optimized without constraints to obtain the true minima structures for each spin state.
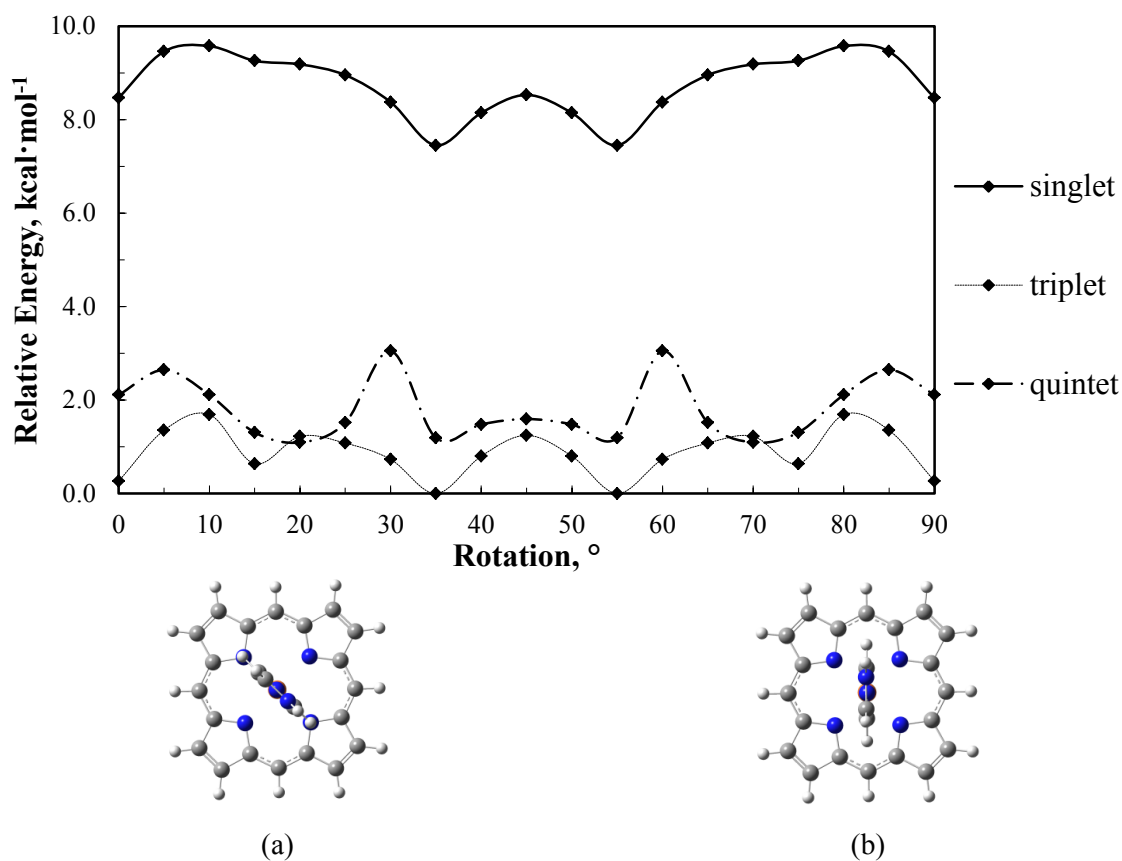
Figure 3.2. Potential energy surfaces for the singlet, triplet and quintet states of FePIm computed at B3LYP/6-31G(f) for iron and B3LYP/6-31G(d,p) for all other atoms. The configuration of structure (a) defines a 0° rotation and structure (b) defines a 45° rotation.

The energy barrier of rotation is less than 2.1 kcal·mol^{-1} for the singlet, triplet and quintet spin states. This shallow potential energy surface implies that there is some degree of free rotation in the porphyrin ring with respect to the imidazole group. It should also be noted that the potential energy surfaces for the triplet and quintet states are very close in energy, intersecting at points. Thus, for this functional, the ground state varies depending on the relative orientation of the porphyrin ring with respect to the imidazole group.

3.3.2 Structures

The relative energies of each spin state of Fe^{2+}, FeP and FePIm are reported in Table 3.1. The ground state of the Fe^{2+} ion is the quintet state. The ground states of FeP and FePIm are the triplet states. This difference is due to two competing energetic effects: Hund's rule, which predicts high-spin states to be energetically favoured since they exhibit greater electron-nucleus attraction energies, a result of greater electron repulsion from Fermi, or exchange, correlation;[114] and the aufbau principle, which favours filling the lowest available molecular orbitals. The qualitative ordering of the relative energies is in agreement with results computed with other computational studies.[88,100] It should be noted that the quintet state of FePIm, which is the predominant state in deoxygenated heme, is very close in energy to the triplet ground state having an energy difference of less than 1.5 kcal·mol^{-1}.

The computed geometry for the quintet state is in agreement with experimental results for human deoxyhemoglobin.[94] The experimental out of plane displacement of iron from the plane defined by the nitrogen atoms of the porphyrin is 0.36(5) Å. The computed displacement for the quintet state is 0.361 Å which is within the error of the

54

experimental result. The experimental bond distance between the iron and the nitrogen of the proximal histidine group is 2.06(2) Å and between the iron and the nitrogens of the porphyrin is 2.12(4) Å. The computed bond distances for the quintet state are in good agreement: 2.098 Å, between iron and the nitrogen of the imidazole group (Fe-N_{Im}); and 2.179 Å, between the iron and the nitrogens of the porphyrin (Fe-N_P). This excellent agreement between the computed and experimental geometries provides further support to the adequacy of the level of theory chosen in the present work.

Table 3.1. The relative energies (kcal·mol^{-1}) for each spin state of Fe^{2+}, FeP and FePIm computed at the B3LYP/6-31G(f) level for iron and the B3LYP/6-311G(d,p) level for all other atoms.

	Singlet	Triplet	Quintet	Septet	Nonet
Fe^{2+}	91.59	61.08	0.00	94.10	1697.78
FeP	39.79	0.00	15.45	48.75	93.41
FePIm	8.87	0.00	1.48	27.51	68.69

The optimized molecular structure of imidazole ligated iron (II)-porphyrin is shown in Figure 3.1. The molecular graphs of the optimized structures for its various spin states are shown in Figure 3.3. It can be seen in these graphs that the out of plane displacement of iron is greatest in the high-spin states, relative to the singlet state. Distances for the out of plane displacement are listed in Table 3.2. There is no displacement of iron from the plane in the unligated iron (II)-porphyrin species. Even when computed using no symmetry constraints, the displacement from the plane is negligible (less than 0.001 Å). This supports the notion that the doming effect observed in hemoglobin is not a result of a larger volume of the high-spin state of iron, since if this were the case, a similar displacement should also be observed in the unligated structure.

Molecular Graph

Spin State	Side view	Top view
Singlet		
Triplet		
Quintet		
Septet		
Nonet		
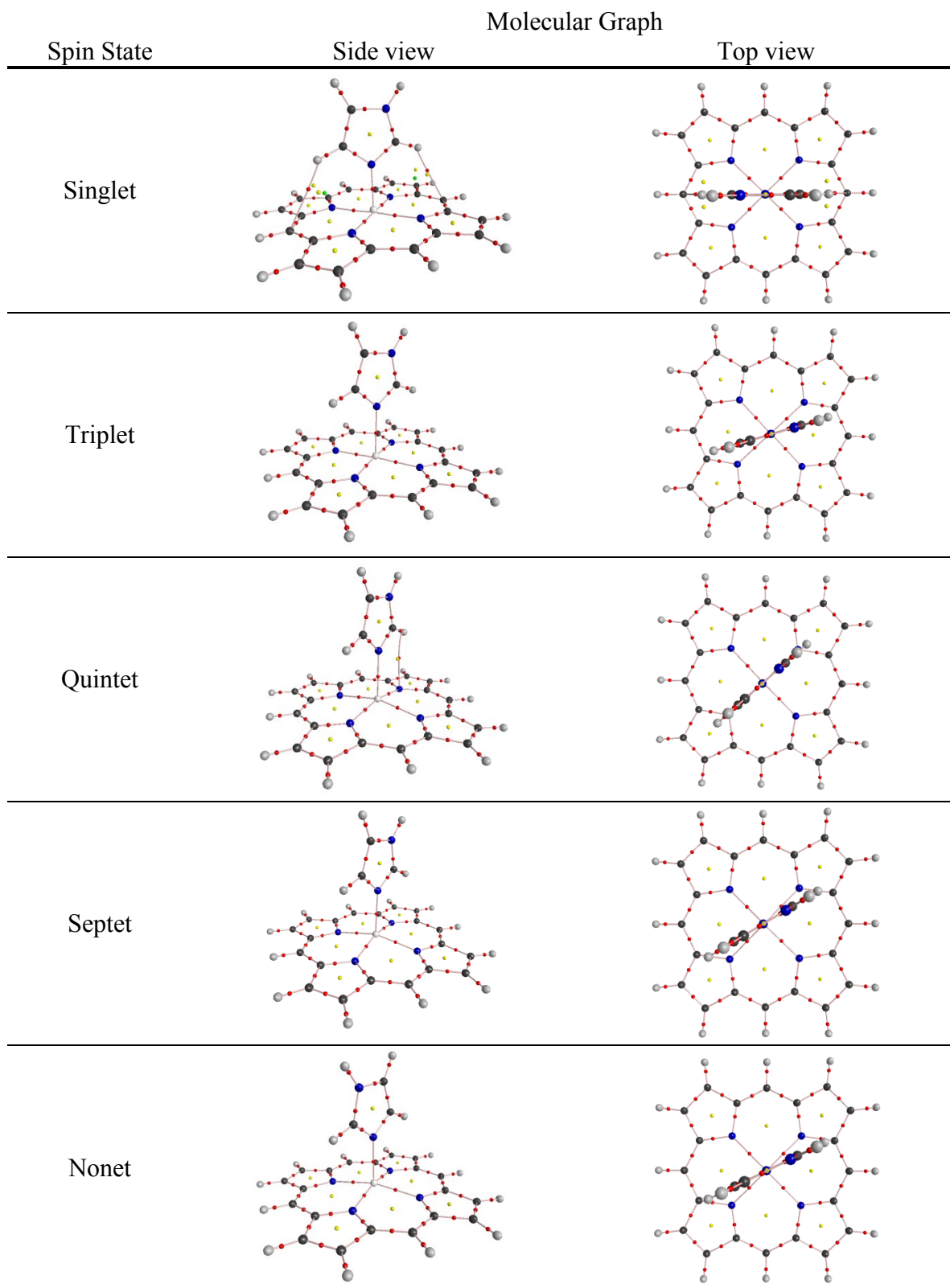
Figure 3.3. Molecular graphs for each spin state of FePIm. Bond critical points (BCPs) are denoted in red and ring critical points (RCPs) are denoted in yellow.

56

Table 3.2. The out-of-plane displacement (Å) of iron from the porphyrin plane and the iron-nitrogen bond distances (Å) for each spin state of FePIm.

	Singlet	Triplet	Quintet	Septet	Nonet
Displacement	0.161	0.115	0.361	0.379	0.237
Fe-N_P	2.005	2.008	2.098	2.064	2.069
Fe-N_{Im}	1.926	2.255	2.179	2.112	2.109

Given the larger out of plane displacement in the quintet state versus the triplet state, the Fe-N_P and Fe-N_{Im} distances are as expected. Relative to the triplet state, the Fe-N_P distance in the quintet state is larger due to the greater distortion from the plane. This distortion in the quintet state brings the iron atom closer to the imidazole group resulting in a stronger interaction and a shorter distance, relative to the triplet state.

3.3.3   Atomic Volume of Iron

The atomic volume of iron in each spin state of FeP and FePIm is listed in Table 3.3. Relative to the triplet ground state, the iron atom in the quintet state of both molecules has a smaller volume. The average electron densities for iron are also listed in Table 3.3. The average electron density of an atom is defined to be the total electron population of the atom bound by the union of a chosen isodensity envelope and the internal zero-flux surface divided by its atomic volume. An isosurface of $\rho = 0.001$ au was used in this study. The larger average electron density of the quintet state relative to the ground state demonstrates that the charge concentration is greater in the quintet state, since a larger percentage of the electron population resides in the atomic volume for the quintet state of iron. This suggests that the electron density is more concentrated and compressed in the quintet state. This is indicative of electron donors and reflects iron susceptibility to oxidation.

Table 3.3. Volumes (au^3) bound by a 0.001 au isosurface of the electron density, the average electron density (au) within each volume and the atomic charges (au) of iron for each spin state of FeP and FePIm.

		Singlet	Triplet	Quintet	Septet	Nonet
FeP	Volume	95.02	103.07	92.75	110.15	81.58
	Average ρ	0.261	0.240	0.265	0.224	0.297
	Charge	1.166	1.203	1.379	1.323	1.727
FePIm	Volume	72.05	79.46	76.35	70.42	70.01
	Average ρ	0.343	0.311	0.322	0.344	0.346
	Charge	1.255	1.287	1.379	1.740	1.759

QTAIM defines the atomic charge to be the difference between the nuclear charge of the atom and its total electron population in a molecule. The atomic charge for iron is also listed in Table 3.3. The atomic charge of iron in the quintet state is more positive than in the ground state. This would increase the propensity for the iron atom to react with an approaching O_2 molecule, or other electron-rich molecule, in the quintet state. It should also be noted that the charge difference between Fe and N_{Im} in the quintet state is 2.523 au and in the triplet state is 2.410 au.

3.3.4 *Electron Density at the Bond Critical Point*

The electron density (ρ) at the bond critical point (BCP) provides a measure of bond strength.[115,116] The ρ_{BCP} and $\nabla^2 \rho_{BCP}$ values for the bond critical points around iron in FePIm are given in Table 3.4. The magnitudes of the electron densities and sign of the Laplacian at the BCP indicate that the interactions between iron and the surrounding nitrogen atoms are closed-shell interactions. The two states of significant interest are the triplet, since it is the ground state, and the quintet state, since it has physiological importance. In comparing the electron densities of these states the quintet state has a

greater electron density at all of the BCPs between iron and the surrounding nitrogen atoms. This is expected between the iron and the nitrogen atom of the imidazole group since there is a shorter bond length in the quintet state, reported in Table 3.2. However, the greater electron density between the iron and the nitrogen atoms of the porphyrin ring is counter intuitive, since the bond is longer due to the larger out of plane displacement of the quintet state. This also contradicts an earlier suggestion that the doming is due to the weakening of the Fe-N_P bonds.[100]

Table 3.4. Electron density, ρ, (au) and Laplacian, $\nabla^2\rho$, (au) at the bond critical point between iron and the nitrogen of the imidazole group and the average electron density between the iron and the four nitrogen atoms of the porphyrin ring for FePIm.

		Singlet	Triplet	Quintet	Septet	Nonet
Fe-N_P*	ρ	0.0816	0.0691	0.0742	0.0849	0.0837
	$\nabla^2\rho$	0.469	0.331	0.331	0.277	0.272
Fe-N_{Im}	ρ	0.0976	0.0591	0.0618	0.0739	0.0737
	$\nabla^2\rho$	0.613	0.247	0.223	0.244	0.254

*Average ρ of the four BCPs of Fe-N_P, standard deviation < 0.0007 au. Average $\nabla^2\rho$ at the four BCPs of Fe-N_P, standard deviation < 0.005 au.

3.3.5 *Molecular Orbitals*

In order to further investigate the above results, the molecular orbitals were plotted. The reactive molecular orbitals, or highest occupied molecular orbitals (HOMO), of the triplet and quintet states of FePIm are shown in Figure 3.4. With respect to the iron atom, the highest occupied orbital of the triplet state is the d_{z^2} orbital. In the quintet state the $d_{x^2-y^2}$ orbital of the iron atom is the highest occupied orbital. The resulting interactions with the surrounding porphyrin environment have both bonding and antibonding character. Although previous studies[100,102] have proposed that the magnitude

of the antibonding interaction is greater in the quintet state, resulting in the longer Fe-N$_P$ bond distance, it is quite difficult to deduce which orbital interaction has greater antibonding or bonding character from the diagrams shown in Figure 3.4. Taking into account the greater electron density at the BCPs between Fe and N$_P$ in the quintet state, it is unlikely that the orbital interactions of the quintet state have greater antibonding character, or that this is the cause of the out of plane doming seen in the quintet state. The greater electron density at these points would infer that these interactions have significantly more bonding character. The doming effect likely causes the longer bond distance in spite of the stronger bonding interaction, and not vice versa. This is supported by the molecular orbital diagrams that are observed for the unligated FeP species, since no doming is seen in these species and the Fe-N$_P$ orbital environment is very similar.

(a)   (b)
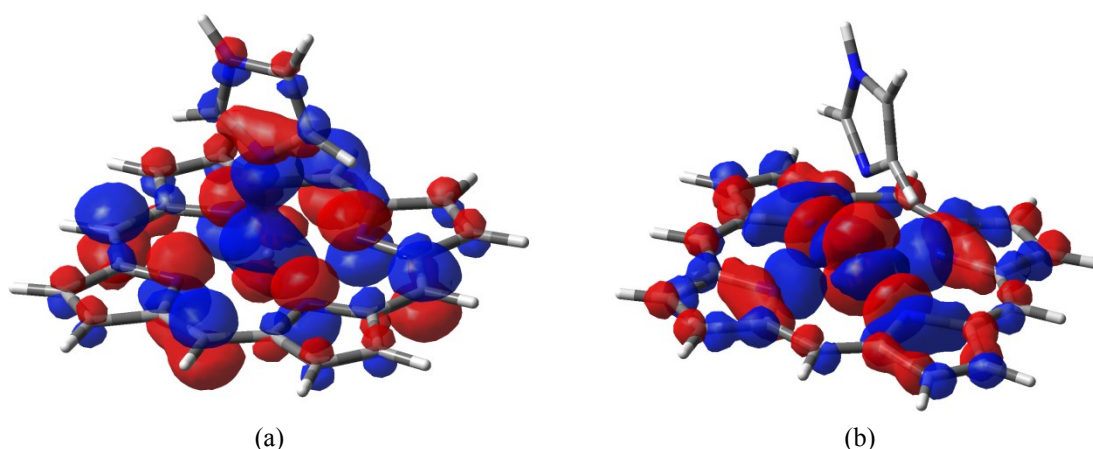
Figure 3.4. Highest occupied molecular orbital (HOMO) of the triplet (a) and quintet (b) state of FePIm. Positive and negative lobes are indicated by red and blue, respectively.

Since there is no doming observed in the unligated porphyin species the cause of the doming must involve the interaction of the iron and porphyrin ring with the imidazole group. It can be seen from the molecular orbital diagram that in the triplet state the d_{z^2} orbital would typically have an antibonding interaction along the Fe-N$_{Im}$ bond. However,

in this case the d_{z^2} orbital has distorted itself so that the equatorial lobe is interacting with the orbital on the N_{Im} atom. This distortion likely contributes to the lower electron density at the Fe-N_P BCPs in the triplet state. Despite this distortion, the electron density at the BCP between Fe and N_{Im} is greater in the quintet state than in the triplet state. The weaker interaction in the triplet state causes Fe^{2+} to remain in the porphyrin plane. A greater out of plane displacement is seen in the quintet state due to the stronger Fe-N_{Im} interaction which pulls the iron atom out of the plane. This is likely due to the larger atomic charge difference between these atoms in the quintet state resulting in a greater electron density and stronger interaction.

3.4   Conclusions

The QTAIM analysis of the doming in iron-porphyrin complexes shows that in the quintet state of FePIm the iron atom is spatially smaller and has a larger out of plane displacement than in the triplet ground state. This is consistent with recent studies and renders the original assumption that the larger size of high-spin iron was the cause for the out of plane displacement observed in heme invalid.

There is no iron out of plane displacement observed in the unligated iron (II) porphyrin, FeP, and the ρ values at the iron BCPs are higher, indicative of a stronger Fe-N_{Im} bonding interaction in the quintet state relative to the triplet state. Therefore the cause of the doming must depend significantly on the interaction of FeP with the imidazole group. In conclusion, the doming effect observed in the quintet state is a result of two effects: the nature of the occupied of molecular orbitals, resulting in a lessened repulsion between Fe^{2+} and nitrogen of the imidazole group relative to the triplet state;

and a greater electrostatic attraction between Fe^{2+} and nitrogen of the imidazole group due to a greater difference in atomic charge.

Chapter 4 : Binding of O₂ to Iron Porphyrin: Effects of Hartree-Fock and Range-Separated Exchange

The research presented in this chapter has been submitted for publication: Berryman, V. E. J.; Boyd, R. J.; Johnson, E. R. Balancing Exchange Mixing in Density-Functional Approximations for Iron Porphyrin, *Journal of Chemical Theory and Computation*.

4.1   Introduction

Many biological proteins have active sites that feature metalloporphyrin centers. These systems represent a significant area of research due to their diverse chemical applicability and potential for diagnostic and therapeutic purposes.[117–119] Iron-centred systems in particular have attracted much interest due to their relevance in biological systems, known universally to occur in the oxygen-carrying proteins hemoglobin and myoglobin, as well as in enzymes such as cytochrome c and peroxidase.[120–122]

The functionality of the hemoglobin protein is, in part, due to the structure of the high-spin state of iron at the centre of the heme group, an iron-porphyrin structure.[123] Since these systems are characterized by multiple spin states that are relatively close in energy, they present a challenge to electronic structure methods in accurately predicting the correct ground state. Another challenging feature of the system is that upon dioxygen binding to the heme group the spin state of the system changes. This makes them an attractive system to test the ability of contemporary functionals of density functional theory (DFT) to account for the properties of transition metal complexes.

Density functional theory is probably the most popular electronic structure calculation method for efficient, approximate calculations of chemical systems. Despite widespread popularity, there are important limitations of the method that are apparent in

some chemical systems. One such error is the many-electron self-interaction error, or delocalization error, which is a common problem for many popular density functional approximations, such as widely used GGA and hybrid functionals.[123–126] This is because the non-locality of the exchange-correlation hole is crucial, leading to failures in the calculation of dissociation barriers and long-range charge-transfer excitations. These errors result from the artificial stabilization of delocalized states, and can also arise from the destabilization of localized states.[123,124,126]

Hybrid functionals attempt to resolve this error by including a portion of Hartree-Fock (HF) exchange. The goal is to incorporate exactly computed nonlocal exchange, also referred to as Fermi correlation, which is difficult to model in the functional form since it is composed of local variables such as density, the gradient of the density, the Laplacian and the kinetic energy density. However, the HF method does not take into account Coulomb correlation and thus localizes the electron density. Since pure DFAs delocalize the electron density, hybrid functionals aim to blend these effects to achieve a better description of the electron density.

Long-range corrected hybrid density functionals attempt to resolve delocalization error by enacting 100% HF exchange for long-range electron-electron interactions, where the parameter denoted ω controls the partitioning of the interelectronic distance, r_{12}. The electron repulsion, $\frac{1}{r_{12}}$, is partitioned at a parameterized value, denoted ω, such that:

$$\frac{1}{r_{12}} = \frac{\text{erf}(\omega r_{12})}{r_{12}} + \frac{erfc(\omega r_{12})}{r_{12}}$$

4.1

The first and second terms of equation 4.1 are the long range and short range portions of the electron repulsion, respectively. It should be noted that as ω increases, the r_{12} value decreases and thus more of the electronic interactions are being treated by 100% HF

exchange. The erf and erfc functions, known as the Gauss error function and complementary Gauss error function, respectively, ensure the terms sum to unity. For further details see references 127 and 128. Other methods for range-separation have also been used,[129] but the concept remains the same whereby a transition between a short range description and a long range description happens at a defined length scale.

This study aims to investigate the performance of common density functionals for an iron porphyrin model system, focusing on the prediction of the correct ground state spin multiplicity and the dioxygen binding energy. The role of the exchange functional on the prediction of these properties is highlighted.

4.2   Computational Methods

A model system comprised of porphine and an imidazole axial ligand, are used to model the heme and histidine groups, respectively. This is a common model system employed to represent the active sites of both hemoglobin and myoglobin, since it retains the central feature of heme, and is previously employed in Chapter 3 of this thesis.[85,100,102,130] A model system is essential, since modelling the entire heme group with the quantum mechanical methods would not be computational feasible. In this chapter, the model system is denoted as FePIm and is shown in Figure 4.1a. Dioxygen binding to the heme group is of interest in this chapter and this system is modelled by the FePIm system with dioxygen bound to the remaining axial coordination site of the iron, denoted FePIm-O_2 herein, and shown in Figure 4.1b.

All calculations are performed using the Gaussian 09 program package.[70] Density functional theory methods are used for all calculations. Spin-unrestricted calculations were employed for all calculations, due to the high-spin nature of the FePIm system and

the open-shell singlet nature of the FePIm-O_2 system, where dioxygen has been shown to resemble the superoxide anion, with a low-spin Fe(III) centre antiferromagnetically coupled to the radical superoxide anion.[131] The open-shell singlet nature of the system, as it is commonly referred, may also be considered a broken symmetry singlet. Geometry optimizations and frequency calculations were initially computed for all complexes with the B97-D functional employing a mixed basis set comprised of 6-311+G(f) on iron, 6-311+G(d) on nitrogen, sulfur and oxygen, and 6-31G on carbon and hydrogen.[65] Energies reported herein are corrected to the Gibbs energy at 298 K. Single point calculations were employed for all further calculations. The systems were calculated in the gas phase and no symmetry constraints were applied to the systems.

| (a) | (b) |
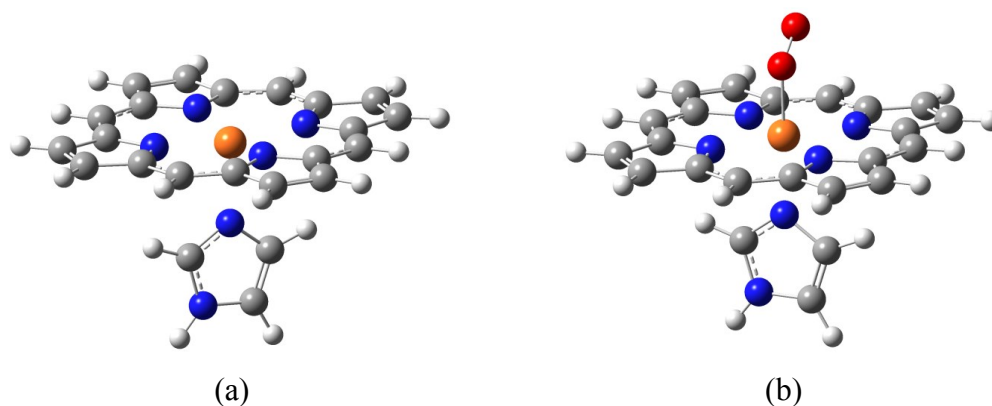
Figure 4.1. The model system for FePIm (a) and FePIm-O_2 (b) used in this study. Carbon, nitrogen, oxygen and hydrogen atoms are shown as grey, blue, red and white spheres, respectively. Iron atom is shown in orange.

In the first part of this study, 11 density functional approximations (DFAs) were compared. These comprise four classes of DFAs: GGAs; BLYP,[53,54] BLYP-D, [53,54,65] B97-D;[65] hybrid GGAs; B3LYP,[54,55] B3LYP-D,[54,55,65] PBE0;[132–134] hybrid meta-GGAs; M06,[68] M06-2X;[68] and range-separated hybrid GGAs: ωB97;[128] ωB97X;[128] ωB97X-D.[127] A number of the functionals also include empirical dispersion corrections, which is often denoted by '-D' in the functional name.[65] The M06 and M06-2X functionals are said to

account for non-covalent interactions, including dispersion, based on parameterization with test sets that include such interactions. It has been shown previously that including dispersion interactions improves calculated binding energies for a variety of transition metal complexes.[135]

Two basis set schemes were employed, both comprised of Pople-type basis sets. The first employs different basis sets for different atoms in the molecule for computational efficiency and allows for a high level calculation on the central region of the system, where the binding interactions occur. This basis set, denoted basis set I, employs 6-311+G(f) on iron, 6-311+G(d) on nitrogen and oxygen, and 6-31G on carbon and hydrogen. This approach has been shown to be successful for heme-containing systems.[136] The second basis set, denoted basis set II, employs 6-311+G(2fg) on iron and 6-311+G(2df,p) for all other atoms. This larger basis set is suitable for single point calculations, but optimizations are not computationally efficient for exploration of the potential energy surface.

In the second part of this study, the effects of including Hartree-Fock (HF) exchange and range-separated corrections on the spin state energetics and dioxygen binding energy of the iron porphine system are investigated. Single point calculations with BLYP-based hybrid functionals were performed where the amount of HF exchange is systematically varied. The previously optimized structures and basis set I are employed.   Addition of HF exchange is accompanied by a corresponding decrease in the amount of DFT exchange. Subsequently, the characteristic length scale of the range-separation, defined by ω, is also systematically varied in a series of LC-BLYP calculations.   The quantum theory of atoms in molecules, denoted QTAIM, was

employed to analyze the topology of the electron density to determine atomic charges and delocalization indices. The AIMAll software was employed to compute these QTAIM properties.[112]

4.3   Results and Discussion

4.3.1   *The Iron Porphine Model System*

The FePIm model system was optimized in the triplet and quintet spin states. The singlet state was not considered as it has been consistently shown to be 4.6-10.6 kcal·mol^{-1} higher in energy than the high-spin states.[85,137] Human deoxy hemoglobin exists in the quintet state,[138] however it is common for density functional approximations to favour lower spin multiplicities, thus incorrectly predicting the ground state. This is well-known error when a given electron configuration gives multiple spin states that are close in energy, which is especially common in transition metal complexes.[7] Thus, the energetics of the spin states are sensitive to the details of the exchange-correlation function and it is useful to consider a functionals performance with respect to the relative energies.

Geometrical parameters for the triplet and quintet states of FePIm are reported in Table 4.1. Experimental data, based on crystallographic studies, for the deoxy forms of myglobin and hemoglobin give a $Fe-N_{Im}$ distance of 2.06-2.15 Å, a $Fe-N_P$ distance of 2.057-2.124 Å and doming from the porphyrin plane by 0.290-0.365 Å.[94,139,140] The computed values are in agreement with the experimental results for the quintet state. Of importance, is the correct increase in doming observed in the high-spin state. Although the doming is slightly underestimated by the B97-D functional, the results are impressive considering the simple model used, lacking the protein environment.

Table 4.1. Geometrical parameters (Å) for the triplet (S = 1) and quintet (S = 2) states of the FePIm system. Changes in distance (Å) between the quintet and triplet state are given such that a negative change indicates a shorter distance in the quintet state.
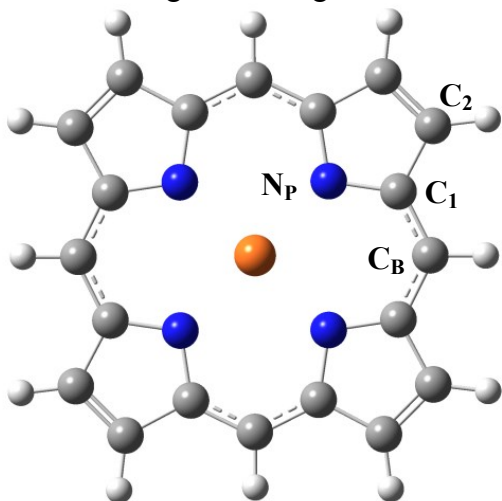
	S = 1	S = 2	Δ
Fe-N_{Im}	2.162	2.128	-0.034
Doming	0.080	0.282	0.202
Fe-N_P	2.014	2.082	0.068
N_P-N_P	4.018	4.137	0.119
N_P-C_1	1.394	1.388	-0.006
C_1-C_2	1.450	1.456	0.006
C_2-C_2	1.375	1.379	0.003
C_1-C_B	1.394	1.406	0.012

B97-D/Fe:6-311+G(f); N:6-311+G(d); C,H:6-31G

Table 4.2. Geometrical parameters (Å) for the FePIm-O_2 system and quintet (S = 2) state of FePIm. Changes in distance (Å) upon O_2 binding are given such that a negative change indicates a shorter distance in the bound state.
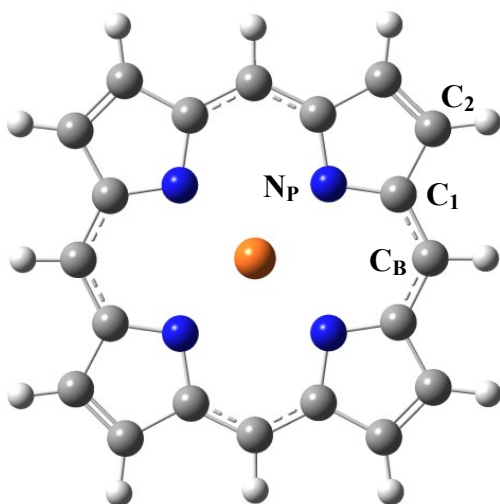
	FePIm-O_2	FePIm, S = 2	Δ
Fe-N_{Im}	2.077	2.128	-0.051
Doming	0.053*	0.282	-0.335
Fe-O	1.846	-	-
O-O	1.275	-	-
∠FeOO	121.0	-	-
Fe-N_P	2.021	2.082	-0.061
N_P-N_P	4.041	4.137	-0.096
N_P-C_1	1.383	1.388	-0.005
C_1-C_2	1.453	1.456	-0.003
C_2-C_2	1.374	1.379	-0.005
C_1-C_B	1.395	1.406	-0.011

*Towards O_2 ligand.

B97-D/Fe:6-311+G(f); N:6-311+G(d); C,H:6-31G

It is well-known that oxyhemoglobin is diamagnetic, having an open shell singlet due to the covalent bonding of unpaired electrons in both iron and oxygen.[141] The geometrical parameters for the oxy-iron porphine model system, along with those for the ground state FePIm system, are shown in Table 4.2. Upon binding, the bond distances shorten, indicating a contracted system in the bound state. The results are in excellent agreement with the experimental results for oxymyoglobin, which report a Fe-N_{Im} distance of 2.06-2.08 Å, O-O distance of 1.24-1.25 Å and Fe-O-O angle of 122-124°.[140,142]

The spin populations, based on QTAIM analysis, are 0.992 au on the iron atom, and -0.367 au and -0.578 au on the proximal and distal oxygen atoms, respectively. The spin density difference plots are shown in Figure 4.2. In the figure, the green surface is arbitrarily chosen to show excess α-spin electron density and the blue surface an excess of β-spin electron density. In this way, the open shell singlet nature of the complex is evident from the localization of a significant portion of the α-spin density on the dioxygen ligand and β-spin density on the iron. There is also a small amount of spin density delocalized over the porphine ring and the coordinating N atom of the imidazole ligand. In addition to spin density difference plots, the highest singly occupied molecular orbitals (SOMO) of α-orbitals and β-orbitals are shown in Figure 4.3. These show the localization of the α-SOMO on the dioxygen and the β-SOMO on the iron and porphine ring. These molecular orbitals have a significant contribution to the excess spin density shown in the spin density difference plots.

(a)   (b)
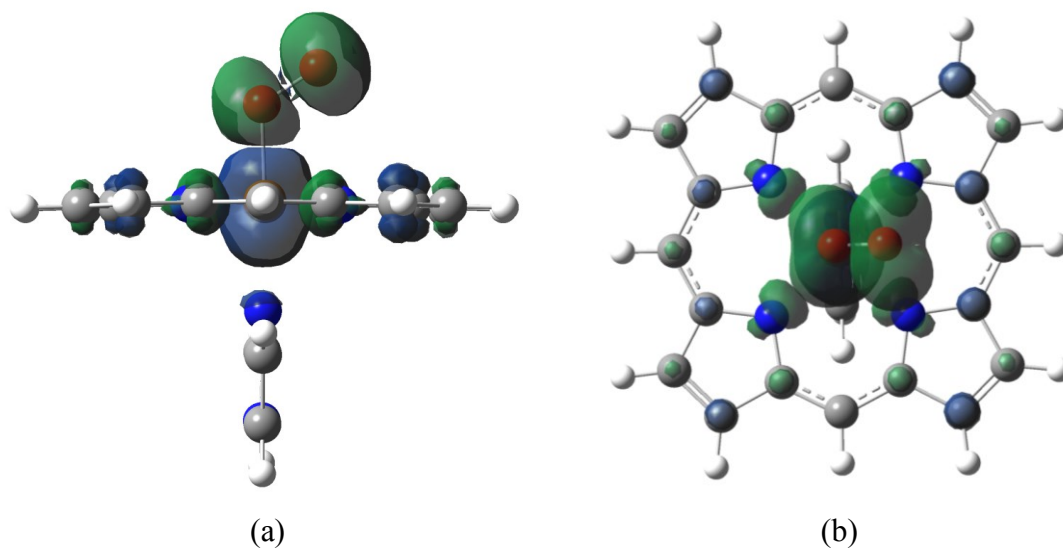
Figure 4.2. Spin density difference plots for FePIm-O_2, with an isosurface of 0.001 au. Two perspectives are shown, showing the axial (a) and equatorial (b) planes. The green surface corresponds to an excess of α-electron density and the blue surface corresponds to an excess of β-electron density.

(a)   (b)
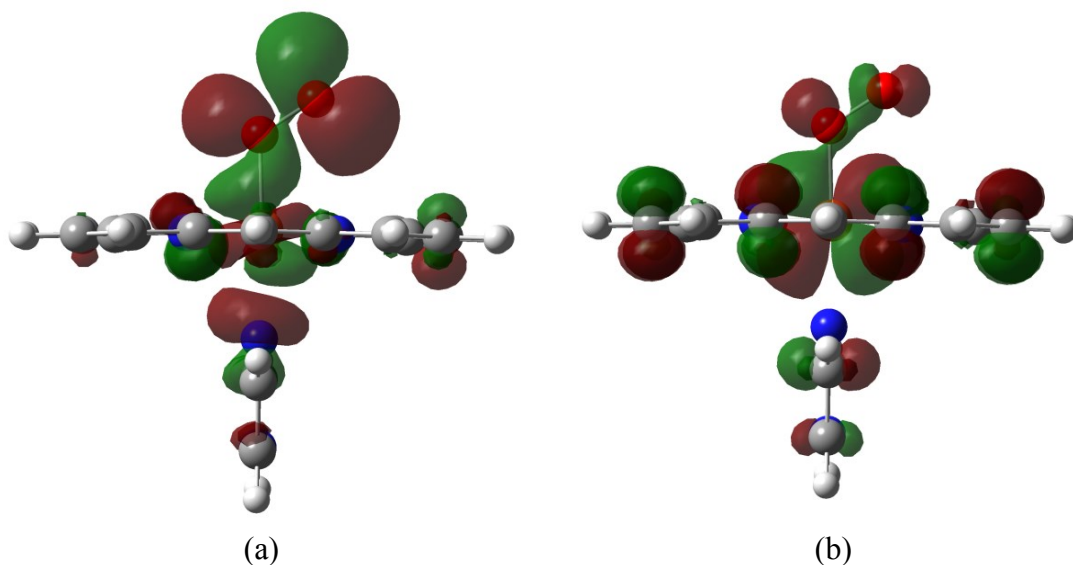
Figure 4.3. The highest energy α (a) and β (b) singly occupied molecular orbitals (SOMO) for FePIm-O_2, with an isosurface of 0.02 au. The positive and negative regions of the molecular orbital are represented as red and green, respectively.

4.3.2 Comparison of Functionals

The energy gap between the triplet and quintet states of FePIm is described by E_S, and is defined as:

$$E_S = E_{triplet} - E_{quintet} \qquad\qquad \textbf{4.2}$$

Thus, a functional that produces a positive value for E_S correctly predicts the quintet ground state for the system.

The binding energy, abbreviated as BE, of O_2 to the porphyrin system is defined as the energy difference between the infinitely separated reactants, the quintet state of FePIm and triplet state of O_2, and the bound system, FePIm-O_2:

$$BE = \left(E_{FePIm} + E_{O_2}\right) - E_{FePIm-O_2} \qquad\qquad \textbf{4.3}$$

Thus, a positive BE indicates favorable O_2 binding and a negative value indicates unfavorable O_2 binding. Table 4.3 reports the results for E_S and BE for all the DFAs investigated in this study.

From these results it is noted that correctly producing both the correct ground state and favored O_2 binding is a challenge for the chosen DFAs. In fact, only one functional, B97-D, is capable of correctly predicting both properties. The relative energy of the triplet and quintet state of FePIm, known as the intermediate and high-spin states, respectively, is not known experimentally; except that the high-spin state is the ground state.[138] Theoretical predictions using CASPT2, a multireference method, estimate the difference to be approximately 10 kcal·mol^{-1}.[143,144] It is known that Hartree-Fock calculations overstablize systems with higher spin multiplicity and it has been shown previously that GGA type DFAs overstabilize lower spin multiplicities, while hybrid

DFAs also overstabilize, but to a lesser extent.[145] From Table 4.3, it is noted that the

BLYP, BLYP-D, B3LYP, B3LYP-D and ωB97 functionals do not predict the correct

ground state, with basis set I. In the case of B3LYP and B3LYP-D the correct ground

state is predicted with the higher bases set: basis set II. Of the DFAs that correctly

predict the high-spin ground state, B97-D is the only functional that also correctly

predicts favourable binding of dioxygen to the iron porphine system.

Table 4.3. Comparison of the differences in energy of the spin states, E_S, and the oxygen binding energies, BE, (kcal·mol^{-1}) computed for the chosen density functionals. The BE is computed relative to the high-spin state of FePIm. For each functional, the fraction of HF exchange is given; for the range-seperated functionals, the value corresponds to the percentage of short-range exact exchange and the ω value is in parentheses. Results are shown for both basis set I and II.

	% HF Exchange	E_S		BE	
		I	II	I	II
B97-D	0	1.46	0.77	9.86	6.01
BLYP	0	-9.15	-9.64	21.74	20.26
BLYP-D	0	-10.93	-11.42	31.96	30.49
B3LYP	20	-0.91	1.84	-9.08	-13.13
B3LYP-D	20	-2.47	0.28	-0.13	-4.18
PBE0	25	4.54	3.79	-18.58	-18.73
M06	27	4.05	3.27	-17.33	-17.84
M06-2X	54	16.53	15.71	-48.18	-48.28
ωB97	0 (0.4)	-0.56	-1.09	-15.75	-16.25
ωB97X	16 (0.3)	1.07	0.54	-24.89	-25.39
ωB97X-D	22 (0.2)	12.36	10.34	-18.23	-18.37
[a]Exp.[146,147]		> 0		8.0	

[a]Gibbs energy change for O_2 binding to myoglobin.
Basis set I: Fe:6-311+G(f); N,O:6-311+G(d); C,H:6-31G
Basis set II: Fe:6-311+G(2fg); N,O,C,H:6-311+G(2df,p)

Only three functionals, B97-D, BLYP and BLYP-D correctly predict favourable binding of O_2 to the iron porphine system. It should be noted that this result does not change, if the binding energy is taken relative to the DFA-predicted ground-state of FePIm. These functionals are all GGA-type density functional approximations, containing no HF exchange component.

From Table 4.3, it is shown that for hybrid functionals the binding energy of oxygen is largely predicted to be negative, or non-bonding. Notably, the M06-2X functional predicts the greatest non-bonding character. It includes 54% HF exchange, the highest amount for the functionals considered herein. This effect will be investigated further is section 4.3.4. The effect of adding dispersion can be seen by comparing BLYP, B3LYP and ωB97X, with the analogous dispersion corrected DFAs: BLYP-D, B3LYP-D and ωB97X-D, respectively. In all cases, the DFA predicts increased binding when dispersion is included. This is not surprising, since including dispersion accounts for interactions between the oxygen atoms and FePIm complex which are important for predicting accurate binding energies. The effects are most clearly shown for the BLYP and B3LYP DFAs and their dispersion corrected analogues, where the dispersion contribution to the binding energy was between 9.0 and 10.2 kcal·mol^{-1}. Comparing ωB97X with ωB97X-D involves varied exchange parameters in addition to the addition of dispersion corrections and so the effect of dispersion cannot be quantified. Dispersion does not have a significant effect on the relative spin-state energies. The M06 and M06-2X functionals are not included in this comparison despite M06-2X being parameterized to include empirical dispersion interactions. This is because the functionals differ in other

ways, such as the amount of HF exchange and the values of optimized parameters.[68] Thus, the differences between them are not solely a result of including dispersion effects.

It is interesting to consider the range-separated DFAs: ωB97, ωB97X, and ωB97X-D which contain 0%, 16% and 22% HF exchange at short-range, respectively. Each enacts 100% HF exchange for long-range electron-electron interactions, for which the interelectronic distance is controlled by ω. The value of ω has been optimized by the developers to 0.4, 0.3, and 0.2 au^{-1}, for the ωB97, ωB97X, and ωB97X-D functionals, respectively. In other words, the ωB97 functional more electron-electron interactions with HF exchange. With only long-range exchange, as with ωB97, the correct ground state is not predicted, as shown in Table 4.3, however, unfavourable binding is predicted. This suggests that the binding energy is more sensitive to the addition of exchange, or sensitive to the addition of HF exchange for long-range electronic interactions. The ωB97X and ωB97X-D functionals predict the correct high-spin ground. The ωB97X-D, with the most short-range HF exchange, predicts a significantly higher value for E_S, or greatest stability for the high-spin state. None of the three range-separated functionals predict binding. The ωB97 functional has the least non-bonding character, or has the least negative *BE* in Table 4.3. Interestingly, the ωB97X-D functional is less non-bonding than the ωB97X functional, despite having a greater amount of short-range exchange. This could be the result of dispersion corrections, which increase binding in other functionals, as mentioned above, or the effect of a decreased ω, thus treating less of the electron-electron interactions with 100% HF exchange.

The effect of basis set size is small. The difference in E_S and BE between basis set I and II is less than 1 kcal·mol^{-1} each for most functionals. In general, the effect of a higher basis set is a decrease in the value of E_S and decreased dioxygen binding, BE.

4.3.3   Effect of Exchange on Spin States

As discussed above, predicting the correct ground state is not a trivial task for density functional approximations. The effect of the percentage of Hartree-Fock exchange added to the BLYP functional on E_S is shown in Figure 4.4. Similarly, the effect of adding HF exchange as a long-range correction on E_S is shown in Figure 4.5. From the results calculated using the BLYP density functional approximation the correct high-spin ground state is predicted when the functional form contains greater than 20% HF exchange, or when ω is greater than 0.4 au^{-1}. This is a relatively large $\frac{1}{r_{12}}$ value, in other words, a short interelectronic distance, r_{12}, with respect to current long-range corrected functionals. The value of ω typically ranges from 0.2 au^{-1} to 0.4 au^{-1}, suggesting exchange is important for the correct ordering of spin states.[127,128,148]

In the HF description of multiple spin states, the energy difference between any two states with the same electron configuration is given by the exchange integral, since they differ only in electron spin. These states yield similar electron densities and since in DFT the exchange-correlation functional depends only on the electron density, the resulting energies in DFT become difficult to determine and are closely dependent on the features of the XC functional.[7] DFT delocalizes the electron density, relative to HF. This has been described as delocalization error, and results in unphysical delocalization of electrons or the unphysical stabilization of delocalized electrons.[123,126]

76
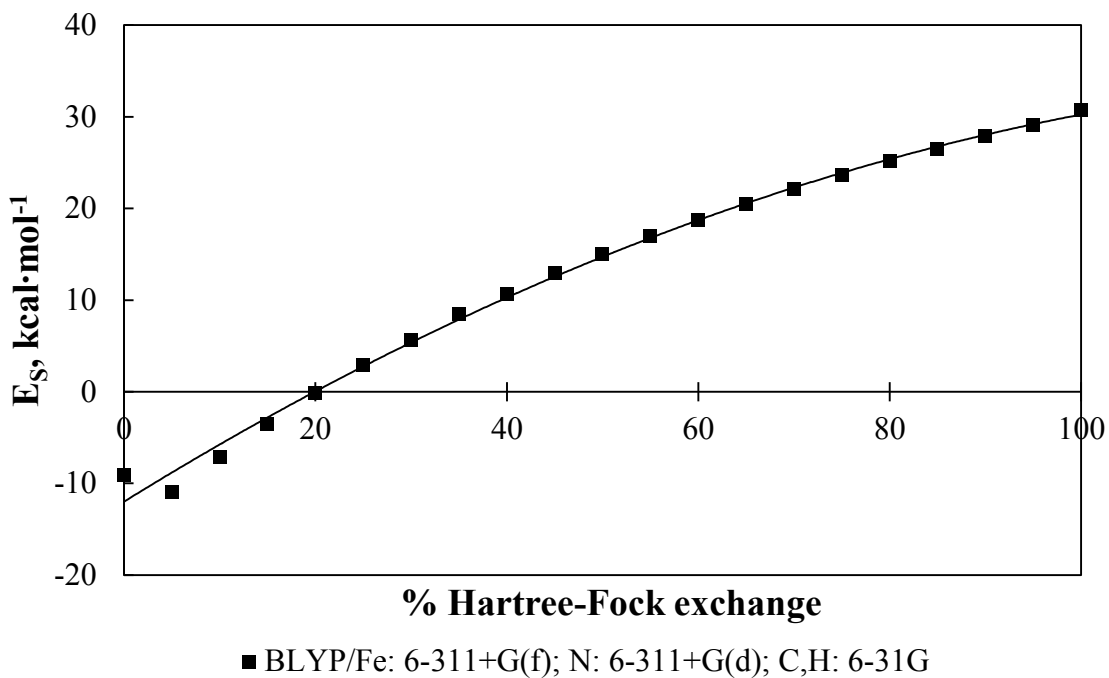
Figure 4.4. The effect of the amount of HF exchange (%) on the relative energy difference between the quintet and triplet spin states of FePIm, denoted E_S (kcal·mol^{-1}).
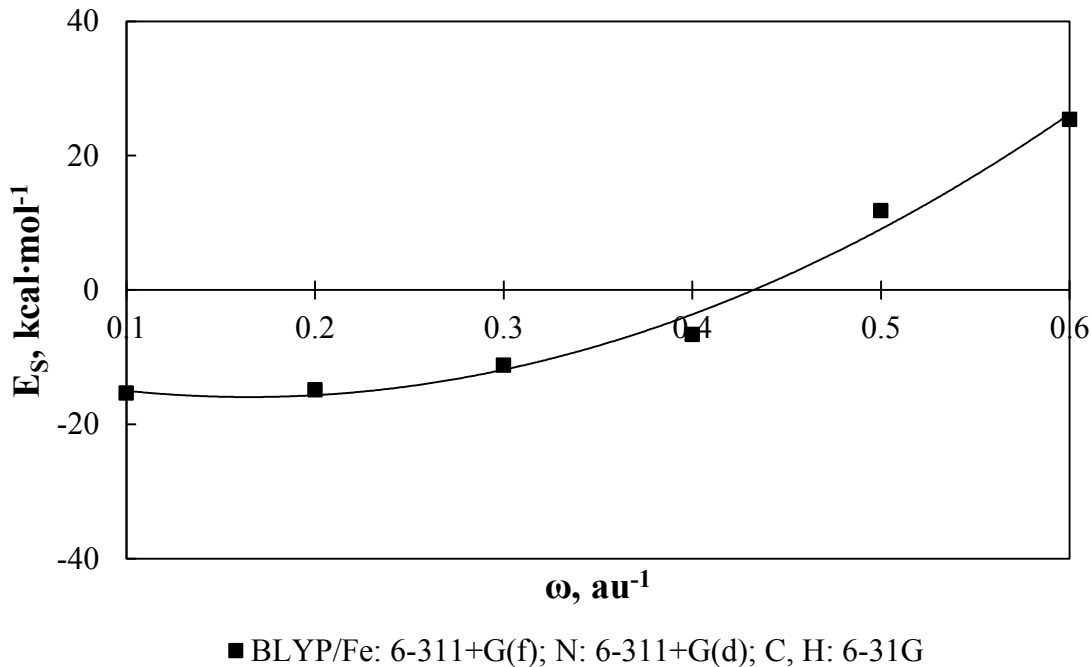
Figure 4.5. The effect of range-separation, denoted by ω (au^{-1}), on the relative energy difference between the quintet and triplet spin states of FePIm, denoted E_S (kcal·mol^{-1}).
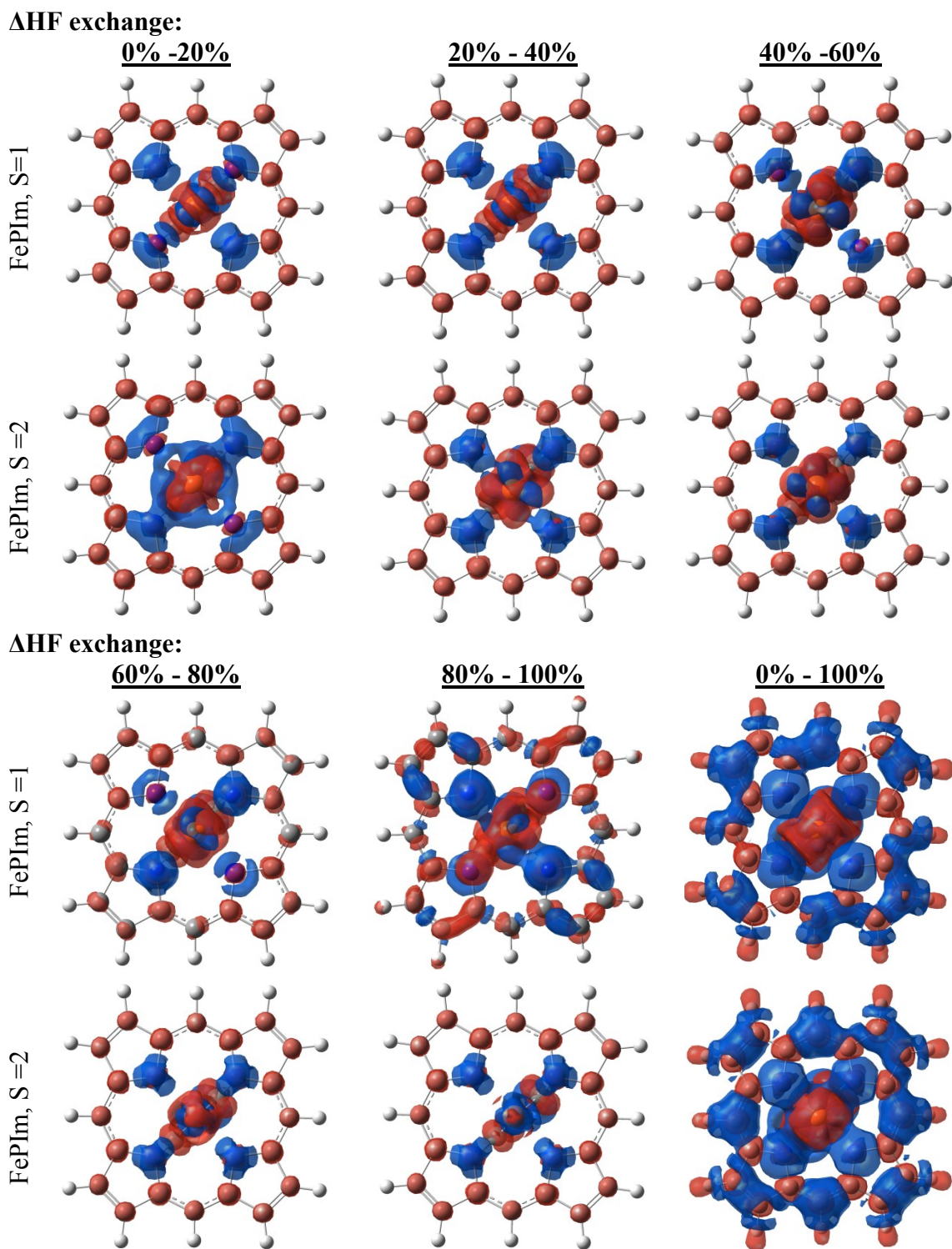
ΔHF exchange:

Figure 4.6. Electron density difference plots for the triplet and quintet state of FePIm in response to increased HF exchange, with an isosurface of 0.001 au. The red surface corresponds to an increase in electron density and the blue surface corresponds to a depletion of electron density.

FePIm, S =1   FePIm, S =2
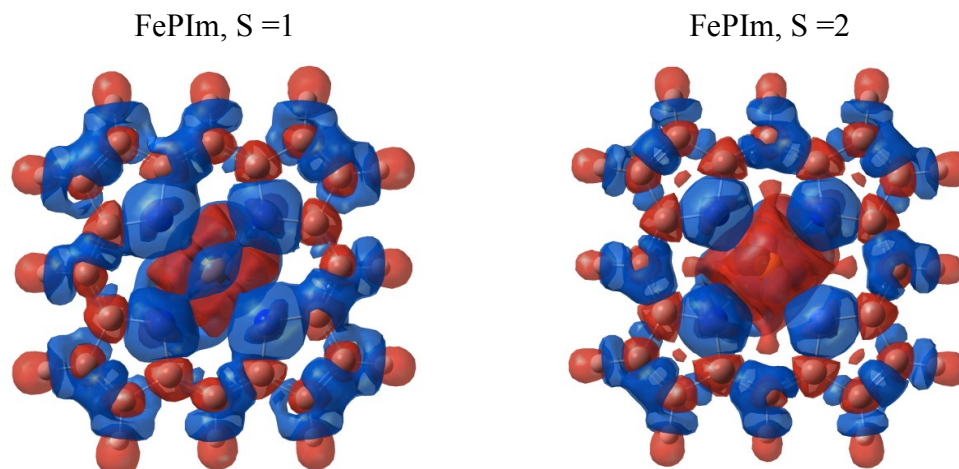
Figure 4.7. Electron density difference plots between ω values of 0.1 and 0.6 au^{-1} for the triplet state and quintet states of FePIm, with an isosurface of 0.0004 au. The red surface corresponds to an increase in electron density and the blue surface corresponds to a depletion of electron density.

$\times$ $\delta(Fe-N_{Im})$, S = 1 $\blacktriangle$ $\delta(Fe-N_P)$, S = 1

$+$ $\delta(Fe-N_{Im})$, S = 2 $\triangle$ $\delta(Fe-N_P)$, S = 2
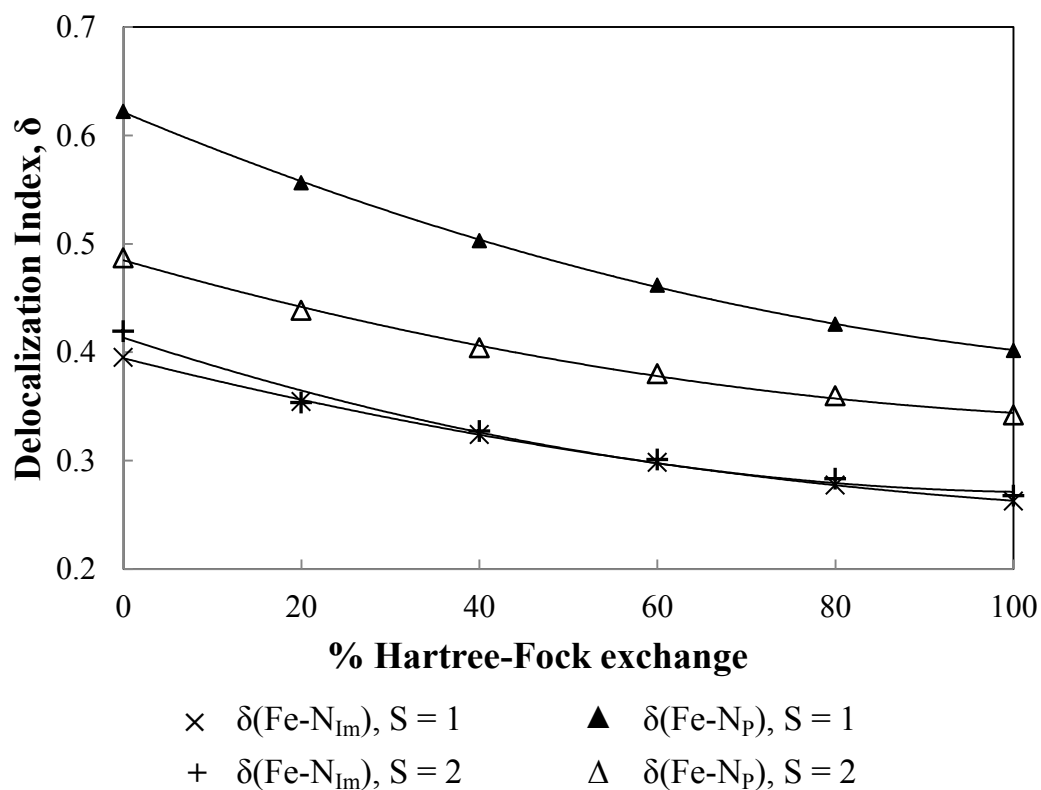
Figure 4.8. The delocalization index, δ, for the Fe-N$_{Im}$ and Fe-N$_P$ bonds for the triplet and quintet states of FePIm with respect to varied HF exchange.

Electron density difference plots for the triplet and quintet states of FePIm with varied increases in the amount of HF exchange are shown in Figure 4.6. Similar results are observed for changes in the value of ω. Electron density difference plots from ω values of 0.1 au^{-1} to 0.6 au^{-1} from the triplet and quintet states of FePIm are shown in Figure 4.7. From these plots it is observed that adding HF exchange results in a decrease in electron density from the π-conjugated system, as shown by the blue surfaces on the porphine ring. Consequently, there is an increase, or localization, of electron density at the atomic centers, most notably in the porphyrin ring, shown by the red surfaces. This effect is also shown in Figure 4.8, which shows the delocalization index for the iron to nitrogen bonds, for both Fe-N$_{Im}$ and Fe-N$_P$, in the triplet and quintet states. In all cases the delocalization index decreases as the amount of HF exchange is increased in the system.

The energy difference in systems with the same electron configuration, differing only in spin state, comes from differences in the number of parallel and opposite spin electrons. Although high-spin state systems have electrons in higher energy orbitals, the parallel spin electrons have increased electron-nuclear attraction energy, as discussed in Chapter 3.[85,98,101] This is the result of Fermi correlation which excludes the possibility of two parallel electrons existing at one place resulting in less screening of the nucleus for parallel spin electrons and is captured by HF exchange. Therefore, it is not surprising that for the triplet and quintet spin states, in the absence of HF exchange, the lower spin state, the triplet state, is favoured. This is because GGAs underestimate the exchange energy. Although this is frequently fortuitously countered by an overestimation of the correlation energy, in the case of the high-spin system the greater number of parallel

electrons are not sufficiently treated with exchange and thus are destabilized relative to the low-spin state.[149,150] This effect can be indirectly observed in Figure 4.8. Overall there is a decrease in delocalization with increasing HF exchange, which is to be expected. The delocalization index for the Fe-N_{Im} bond, δ(Fe-N_{Im}), is effectively independent of the spin state while the delocalization index for the Fe-N_P bond, δ(Fe-N_P), is significantly higher in the triplet state relative to the quintet state for all exchange mixing fractions. This indicates more electron delocalization for the Fe-N_P bonds in the triplet state, consistent. In other words, the inclusion of Fermi correlation, which keeps parallel electrons apart, decreases the effect of localization with addition of HF exchange in the quintet state to a greater extent than in the triplet state.

The stabilization of low-spin states is a known failure of pure DFAs, commonly referred to as either the many-electron self-interaction error or delocalization error, which leads to excessive stabilization of delocalized states. As the amount of HF exchange is added, there is an increase in stabilizing electron exchange energy resulting from the parallel electrons. This is balanced by the destabilizing electronic correlation energy from the electron repulsion energy that results from all electrons, regardless of spin. This is shown in Figure 4.4, whereas the amount of HF exchange is increased, the correct spin state ordering evolves.

4.3.4   *Effect of Exchange on Binding Energy*

The ability of a density functional approximation to predict binding between oxygen and the iron porphine system is also of significant importance. This is a challenge for density functional approximations, as previously demonstrated. As noted above, functionals that include Hartree-Fock exchange, such as a hybrid functional,

predict unfavourable oxygen binding. To more clearly discern this effect, the dioxygen binding energy, *BE*, with respect to the percentage of Hartree-Fock exchange included in the functional is shown in Figure 4.9. Similarly, the effect of adding HF exchange as a long-range correction on BE is shown in Figure 4.10.

From the results calculated using the BLYP density functional approximation binding is favourable only if the amount of HF exchange is less than 15%. Analogously, binding is favoured when ω is less than 0.4 au^{-1}. This suggests that including significant HF exchange character in the DFA is detrimental to predicting favoured dioxygen binding.
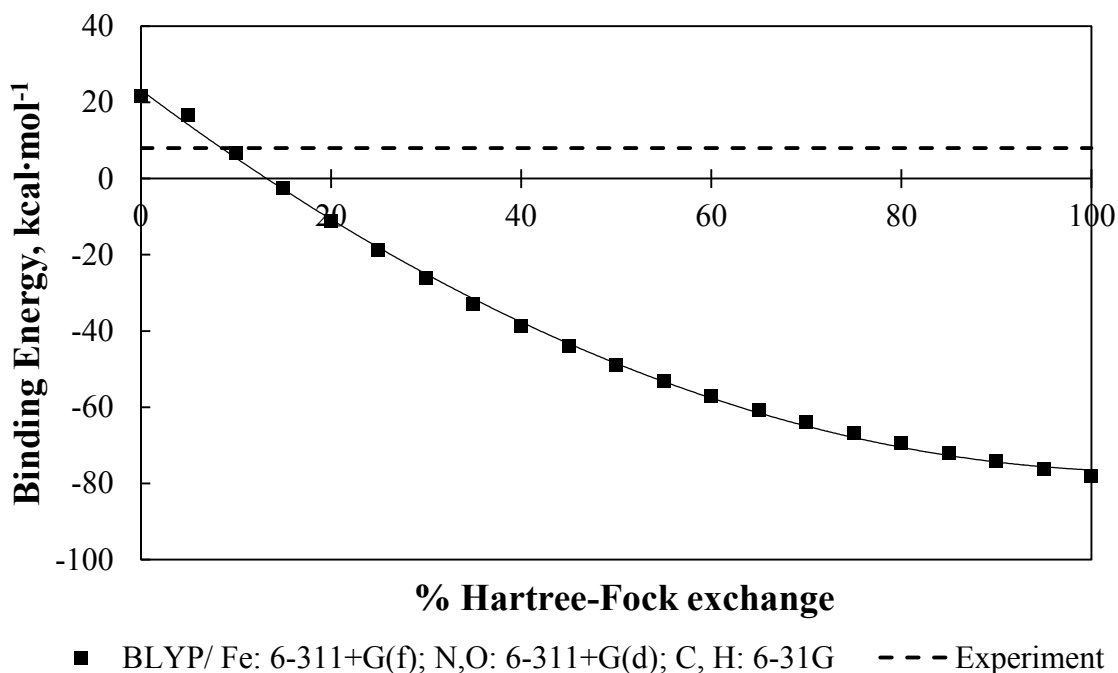
Figure 4.9. The effect of the amount of HF exchange (%) on the dioxygen binding energy of FePIm-O$_2$, denoted *BE* (kcal·mol^{-1}).
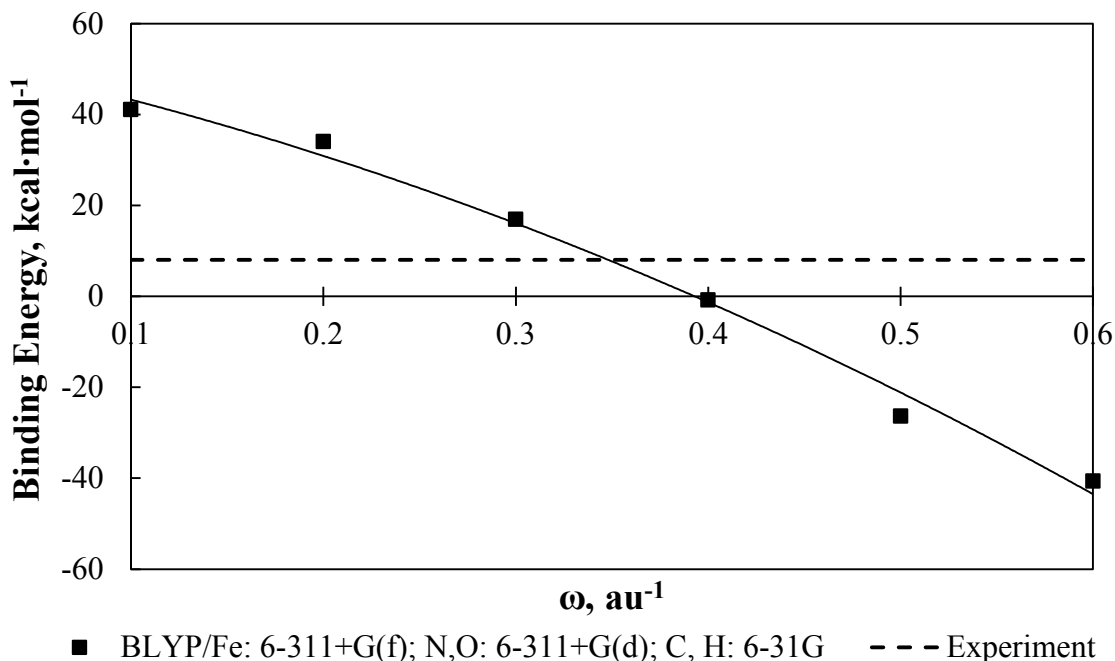
Figure 4.10. The effect of range-separation, denoted by ω (au^{-1}), on the dioxygen binding energy of FePIm-O$_2$, denoted *BE* (kcal·mol^{-1}).

As expected, in the FePIm-O$_2$ system similar effects are observed within the porphine ring. Electron density difference plots are shown for varied HF exchange in Figure 4.11. Again, similar results are obtained for changes in the value of ω. For simplicity, only the electron density difference plot between the ω values of 0.2 and 0.4 au^{-1} is shown in Figure 4.12. As the amount of Hartree-Fock exchange is increased, the electron density becomes more localized on the atomic centers and electron density in the π–system is decreased. However, interestingly, the electron density in the π–system of the dioxygen is increased. This increases the π–character of the O$_2$ ligand, similar to the unbound, free O$_2$ configuration, and leads to a decrease in superoxide character. In other words, the addition of HF exchange destroys the open-shell singlet nature of the system. This is most clearly observed in Figure 4.11 between 0% and approximately 60% HF exchange, which exceeds the amount of HF exchange included in most hybrid

DFAs, and the effect is accentuated in the electron density difference plot showing the change from 0% to 100% HF exchange. Similarly, Figure 4.12 shows the effect of adding HF exchange as a long-range correction. Overall, the increased π–character of the O_2 ligand destabilizes the FePIm-O_2 system, to a greater extent than the destabilization in the FePIm and free oxygen species, leading to unfavourable binding. Thus, increasing the amount of HF, as a percentage or a long-range correction, causes the system to become non-bonding in nature.

ΔHF exchange:

0% -20%   **20% - 40%**   **40% - 60%**

ΔHF exchange:

60% - 80%   **80% - 100%**   **0% - 100%**
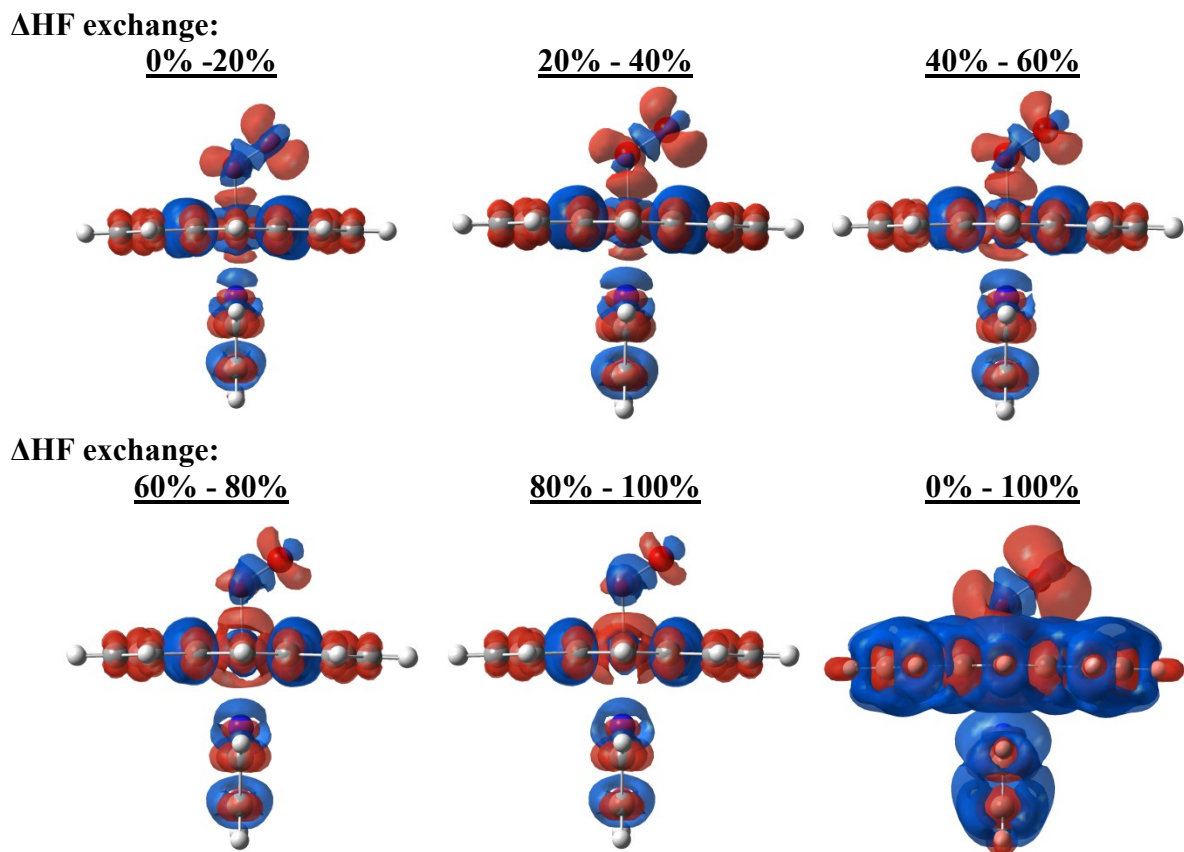
Figure 4.11. Electron density difference plots for FePIm-O_2 in response to increased HF exchange, with an isosurface of 0.001 au. The red surface corresponds to an increase in electron density and the blue surface corresponds to a depletion of electron density.
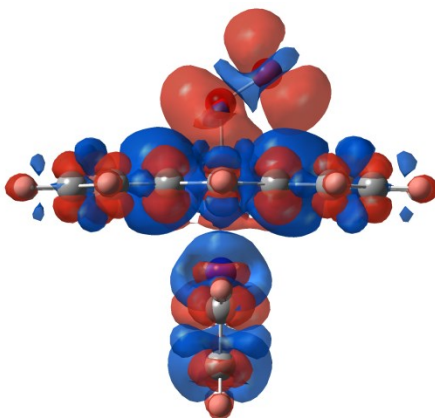
Figure 4.12. Electron density difference plots between ω values of 0.2 and 0.4 au^{-1} for FePIm-O$_2$, with an isosurface of 0.0004 au. The red surface corresponds to an increase in electron density and the blue surface corresponds to a depletion of electron density.

The inability of HF to describe the electron density of the open-shell singlet results from the failure to capture static, or non-dynamical, correlation.[151] The oxygen bound system is a strongly correlated system, where multireference methods are ideal to describe its open-shell singlet nature. Previous multireference analysis suggests that in fact the wave function for the FePIm-O$_2$ system is comprised of a mixture of many configurations, including the Pauling, Weiss and McClure configurations.[152,153] The Pauling configuration is a closed-shell interaction between singlet Fe(II) and singlet O$_2$, the Weiss configuration is the antiferromagnetically coupled interaction between doublet Fe(III) and doublet O$_2^-$ and the McClure configuration is the interaction between triplet Fe(II) and triplet O$_2$. Thus, the ground state of the FePIm-O$_2$ system is complex. HF and DFT methods are based on single determinants, and thus cannot adequately capture static correlation. Although neither HF nor DFT methods are multireference, the tendency of GGAs to give a localized exchange-correlation hole, leading to delocalization error, means that they are fortuitously able to describe the binding of O$_2$ in this case.

This can be briefly described by considering the exchange hole for an electron. The exchange hole is conceptually a hole of electron density that excludes the possibility of another electron existing within it and appropriately normalizes to one electron. In the HF method the exchange hole is too delocalized and is static, thus independent of any reference point. This leads to underbinding descriptions of many systems. GGA-type density functional approximations have a localized exchange-correlation hole. Thus, the exchange-correlation hole is dynamic giving a better description of the nature of the hole. The nature of O_2 binding to the iron porphyrin system, forming a dioxygen moiety with superoxide character, is a type of charge-transfer interaction. In a charge-transfer interaction, an electron is transferred relatively far from the initial system.[154] However, GGA-type density functional approximations neglect long-range effects and incorrectly model the long-range hole behaviour leading to overestimated charge transfers and overbinding in these types of complexes. [151] Essentially, as the reference electron moves away from the system, the exchange hole is too delocalized.[151] Hybrid methods, in short, combine these traits to provide better results. However, in the case of O_2 binding to FePIm, the overbinding property of the GGA, resulting from the localized exchange-correlation hole is necessary to capture the open-shell singlet nature of the bound system. In other words, it is fortuitous delocalization of electron density by the GGA-type DFA that results is favourable binding in the system. A measure of the delocalization observed in the FePIm-O_2 system is shown in Figure 4.13.
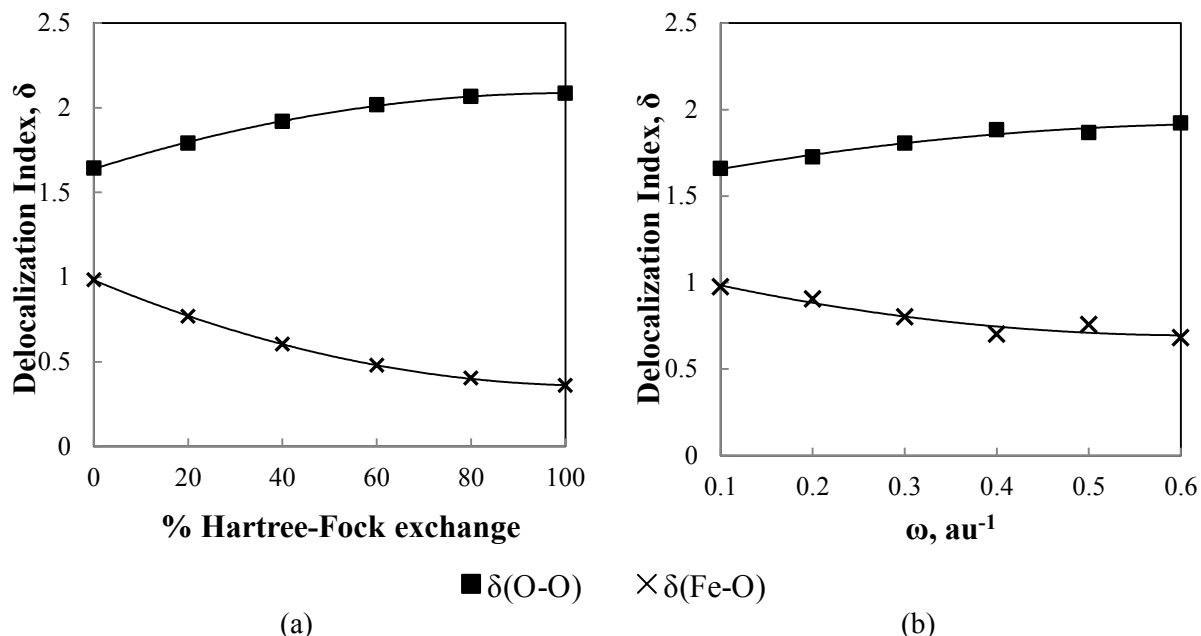
Figure 4.13. The delocalization index, δ, for the O-O and Fe-O bonds in FePIm-O$_2$. with respect to varied HF exchange, shown in (a), and varied ω, shown in (b).

In Figure 4.13, the electron delocalization index is shown for the O-O and Fe-O bonds as the amount of HF exchange and value of ω is varied. The delocalization index, denoted by δ, is the number of electrons delocalized between two atoms. As exchange is added, there are fewer electrons between Fe and O, shown in Figure 4.13a as δ(Fe-O) decreases from 0.98 to 0.36 as HF exchange increases from 0% to 100%. Similarly, in Figure 4.13b, δ(Fe-O) decreases from 0.98 to 0.68 as ω increases from 0.1 au^{-1} to 0.6 au^{-1}. Concurrently, there is a localization of electrons between O-O. Also shown in Figure 4.13, δ(O-O) increases from approximately 1.6 to 2.0 over the range of HF and ω investigated. This generates an unfavourable bonding picture, as the bond between the iron porphine system and the dioxygen weakens, while the O-O bond strengthens, towards a free dioxygen representation. The atomic charges also show these effects. As the amount of exchange in the calculation increases the Fe, proximal O and distal O atoms become more electropositive. This is a result of the localization of electron density

87

on the iron atom, and to the dioxygen ligand. As electron density is localized on the dioxygen, it approaches free dioxygen character, where the atoms have no formal atomic charge. Overall, the addition of HF exchange leads to a non-bonding picture of the system and a decrease in the superoxide description of the oxy-iron porphine system.

These results are summarized with respect to binding energy in Figure 4.14. The effect of varied HF exchange is shown, however, the trend is analogous for varied ω. It follows from the discussion above that favourable binding, or those points in Figure 4.14 on the positive side of the x-axis, result from a system where there is delocalization of electron density between the O-O bond and a localization of electron density between the Fe-O bond. This results in more negatively charged oxygen atoms and a less positively charged iron atom. These results clearly illustrate the relationship between including HF exchange and the binding of dioxygen to FePIm.
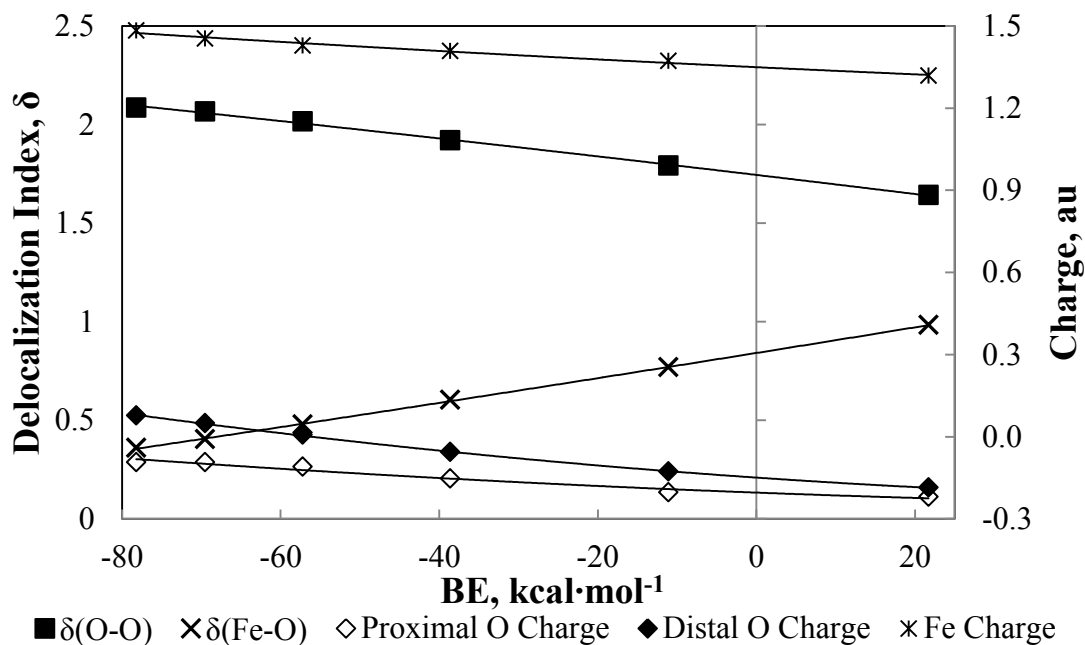
Figure 4.14. Delocalization indices and atomic charges for FePIm-O_2 with respect to varied HF exchange showing the effect on binding energy.

4.4   Conclusions

The results presented herein have shown that the addition of HF exchange provides the correct ground state for the imidazolium ligated iron porphyrin system, yet destabilizes the oxygen bound system. This is a result of the non-bonding description of the system and decrease in the superoxide character by Hartree-Fock exchange. These effects show the fine balance necessary to obtain the correct behaviour from a DFA with the iron porphyrin system, yielding a significant challenge in choosing an appropriate functional to investigate this system. Analysis of the delocalization index, computed using QTAIM, as well as density difference plots are shown to be useful tools to analyze both chemical bonding and errors in DFAs.

It should be noted, that the multireference character of the FePIm-O_2 system is indicative of a system where strong correlation is important. A strongly correlated system is one where the contribution from static correlation is dominant, as opposed to dynamic correlation. None of the functionals studied, or the vast majority of available density functional approximations are designed to handle such systems.

In conclusion, from the functionals studied herein, and the insight gained from the types of density functional approximations studied, the B97-D density functional approximation is a reasonable functional to study oxygen binding to the iron porphyrin system. In the current study, it provides the best performance as the only functional that predicts both the correct ground spin state and favoured binding of dioxygen to the iron porphine system.

Chapter 5 : Modifying Oxygen Affinity in Iron Porphine via Substitution of Amino Acid Ligands at the Proximal Histidine

5.1   Introduction

Metal-centred tetrapyrrole macrocycles, known as metalloporphyrins, are vital components to the active sites of many biological proteins and are responsible for a vast array of chemical processes including oxygen transport, catalysis, electron transfer and active membrane transport.   Thus, they represent a significant area of research for diagnostic and therapeutic purposes acting as imaging agents, photosensitizers, and superoxide dismutase mimics for the treatment of oxidative stress.[117–119] In particular, iron-centred systems have attracted much interest due to their relevance in biological systems such as in the oxygen-carrying proteins hemoglobin and myoglobin as well as in enzymes such as cytochromes, peroxidases and catalases.[120–122,156]

Hemoglobin has four subunits, each containing one heme active site. Upon binding of one oxygen molecule the protein undergoes a conformational change such that the oxygen affinity of the other heme sites increases by as much as 300 times.[92,106] This allosteric mechanism of hemoglobin is facilitated by the displacement of iron from the porphyrin ring towards the proximal histidine residue in deoxy-hemoglobin. The iron is located in the plane of the porphyrin ring in oxy-hemoglobin therefore the proximal

histidine is pulled closer to the porphyrin upon binding causing the conformational change. The magnitude of doming has been shown to be a consequence of both the spin state of the iron and the presence of an axial ligand.[85,98–100] Deoxy-hemoglobin has high-spin Fe(II) centres while oxy-hemoglobin has open shell singlet centres, where the oxygen has been shown to resemble the superoxide anion, with a low-spin Fe(III) centre antiferromagnetically coupled to the radical superoxide anion.[131]

The binding of dioxygen to the heme group of myoglobin and hemoglobin is vital to respiration, but also plays an important role in regulatory pathways of many enzymes that also contain heme groups. The binding of O_2 to heme activates the complex towards further reaction; due to the back donation of electron density from the heme group into the antibonding orbitals of O_2 which both increases electron density and weakens the O-O bond. The increased electron density of O_2 makes it an ideal oxidant allowing for catalytic oxidation of molecules involved in the generation of ATP, a key part of energy generation within the body. In addition, O_2 is an ideal oxidant for synthetic processes due to its low cost and lack of toxic by-products.[157]

The porphyrin ring is axially coordinated to the protein backbone via an amino acid residue. In myoglobin and hemoglobin, the iron centre is coordinated to a histidine residue, however, the histidine is not essential to the stabilization of the heme protein.[158] In fact, in cytochrome *c*, heme is coordinated to a cysteine residue. Additionally, the electron transport capability of the protein has been shown to be maintained upon ligand mutagenesis of the axial ligand to an arginine[159] or tyrosine group.[160] Tyrosine coordination occurs naturally in the catalase protein, responsible for catalysing the decomposition of hydrogen peroxide to water and oxygen.[161] Methoinine coordination

has been observed in bacterial systems.[162,163] Thus, substitution at the axial site is reasonable and has been explored using protein engineering.

In this study, the effect of changing the substituent at the axial position of the iron porphyrin system was investigated. Seven amino acids were chosen based on their prevalence in similar biological systems: arginine, cysteine, glutamic acid, histidine, methionine and tyrosine. The electronic properties of the substitution and the effect on the porphyrin system are investigated. These substitutions are of interest in protein design and have the potential to guide site-directed mutagenesis of proteins for the purpose of catalysis[160] or design of therapeutics.

5.2   Computational Methods

Porphine, the simplest unsubstituted porphyrin ring, is used to model the porphyrin ring of the heme group. It is a common model for the iron porphyrin system since it retains the central feature of the porphyrin structure that is involved in binding to the iron center. Also, it is more computationally efficient than modelling the entire heme group. The iron porphine model framework is shown in Figure 5.1, where the iron is coordinated to four nitrogen atoms of the porphine defined as the equatorial positions. The iron porphine has two remaining axial coordination sites. In this chapter, the deoxy system is denoted FePL, where L is the ligand used to model the amino acid residue in one of the axial positions and the oxy-iron porphine system is denoted FePL-O_2. The ligands used to model the chosen amino acids are defined to have a negative displacement, relative to the plane of the porphyrin ring and dioxygen is defined to be in the positive direction, as shown in Figure 5.2.
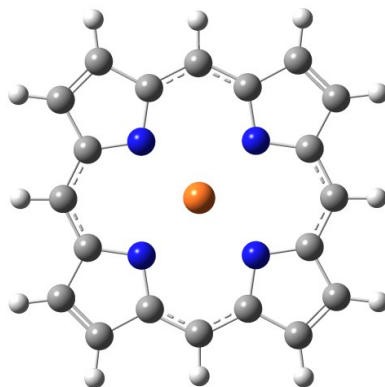
Figure 5.1. The model system for FePL used in this study. Iron, carbon, nitrogen and hydrogen atoms are shown as orange, grey, blue and white spheres, respectively.
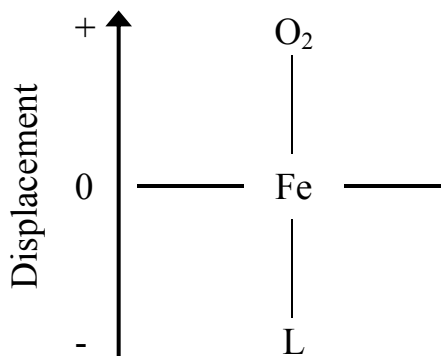
Figure 5.2. The bold lines represent the plane of the porphyrin ring and L the axial ligand. The direction of doming is defined such that doming towards the ligand denoted L is negative and doming towards dioxygen is positive.

In this chapter, all calculations were performed using the Gaussian 09 program package.[70] Geometry optimizations and frequency calculations were computed for all stationary points. The relative energies reported are corrected to the Gibbs energy (ΔG) and enthalpy (ΔH) at 298 K. Spin-unrestricted density functional theory was used for all calculations. The systems studied either have a spin multiplicity greater than 1, in other words, the spin angular momenta does not equal zero ($S \neq 0$), or are open-shell singlets, as in the case of FePIm-O_2. These methods have been shown to be efficient and accurate for iron porphyrins as well as other iron containing complexes.[102,130,164] It has been shown previously that including dispersion interactions improves calculated binding

energies for a variety of transition metal complexes.[135] Following from the previous chapter, the B97-D[65] density functional approximation has been employed to investigate the effect of various amino acids in the axial position on the binding of dioxygen with the iron porpyrhin system. Since multiple spin states of all structures are considered, single point calculations are employed with the ωB97X-D[127] density functional approximation to determine the ground state. The ωB97X-D functional closely predicted the spin state difference between the triplet and quintet spin state of the heme model system, relative to CASPT2 results,[143] as discussed in Chapter 4.

Pople-type basis sets were employed: 6-311+G(f) on iron, 6-311+G(d) on nitrogen, sulfur and oxygen, and 6-31G on carbon and hydrogen. The use of different basis sets within the complex was employed for computational efficiency, allowing for optimization of the geometries, while allowing for higher level calculation on the central region on the system, where the bonding interactions occur. This approach has been shown to be successful for heme-containing systems.[136]

The quantum theory of atoms in molecules analysis, denoted QTAIM, of the optimized systems was employed to calculate atomic charges and evaluate bond strength from the electron density at the bond critical points. The AIMAll software was employed to compute the QTAIM properties.[112]

5.3   Results and Discussion

5.3.1 Iron Porphine System

In this chapter, the deoxy-iron porphine system with an imidazole ligand is denoted FePHis, since the imidazole ligand is a model system for the histidine residue.

This system is of significant interest because it most closely models myoglobin and hemoglobin, which have been extensively studied experimentally. The triplet and quintet states were considered, as the singlet state has consistently been shown to be 4.6-10.6 kcal·mol^{-1} higher in energy than the high-spin states.[135,137,138] The B97-D functional approximation predicts a quintet ground state, lying 1.5 kcal·mol^{-1} lower in energy than the triplet state. This results is qualitatively correct based on experimental studies of human deoxy hemoglobin.[65]

Table 5.1. Experimental and theoretical structural parameters (Å) for FePHis.

	Fe-His	Doming	Fe-N$_P$	N$_P$-N$_P$
B97-D: triplet	2.16	-0.080	2.014	4.018
B97-D: quintet	2.13	-0.282	2.082	4.137
^{a}Exp.[139]	2.15(1)	-0.290(18)	2.057(14)	
^{a}Exp.[140]	2.14(2)	-0.363(11)	2.07(3)	
^{b}Exp.[94]	2.06(2)	-0.36(5)	2.12(4)	

^{a}Crystal structure data from sperm-whale myoglobin. ^{b}Crystal structure data from human deoxy-hemoglobin.

Geometrical parameters for the triplet and quintet states of FePHis are reported in Table 5.1 along with experimental results. The theoretical bond length between the iron and nitrogen of the imidazole ligand, denoted Fe-His falls between the experimental bond length for myoglobin and hemoglobin, which shows some variance between the myoglobin and hemoglobin structures. The average bond length between the Fe and the nitrogen atoms of the porphyrin ring, denoted Fe-N$_P$ is overestimated. This is expected as the calculations are in the gas phase whereas the experimental data is from X-ray crystallographic studies of the solid state. In general, the solid state experiences crystal packing forces which lead to shorter bond lengths relative to the gas and liquid phases. It

is likely that the Fe-N_P distance for the triplet state is also overestimated since a decrease in doming would be accompanied by a shorter distance between the iron and the ring.

Both structures exhibit negative displacement, in other words, the iron is domed towards the bound imidazole ligand. However, the doming in the triplet state is small, with a contracted pocket in the porphine ring, evident from the decrease in N_P-N_P distance. The quintet state exhibits the characteristic doming observed in the heme active site. Again the experimental data shows some variance, but overall greater doming than predicted theoretically.

Table 5.2. Structural parameters (distances in Å, angles in °) for FePHis-O_2 compared to experimental and other theoretical results.

	Fe-His	∠FeOO	O-O	Doming	Fe-N_P	Fe-O	N_P-N_P
B97-D	2.077	121.0	1.275	0.053	2.021	1.846	4.041
[a]**Exp.**[140]	2.06(1)	122(1)	1.24(2)	0.024(6)	2.01(2)	1.81(1)	
[a]**Exp.**[142]	2.08	124	1.25		1.98	1.83	
[b]**Theoretical**[141]	2.032	120.8	1.310		2.038	1.868	
[c]**Theoretical**[130]	2.076	117.9	1.345	0.013		1.891	

[a]Crystal structure data from sperm-whale oxy-myoglobin. [b]Theoretical values are from a QM/MM study employing B3LYP. [c]Data from theoretical study with same model system employing B3LYP.

As discussed above, it is well-known that oxy-hemoglobin is diamagnetic and exists as an open shell singlet due to bonding interactions between unpaired electrons in both iron and oxygen.[141] Geometrical parameters for the optimized geometry FePHis-O_2 are compared to experimental results in Table 5.2. The results are in better agreement with the experimental values than results from theoretical studies of the system employing B3LYP.[130,141] This is especially true with the geometry of the iron and oxygen distances and angles. In the FePHis-O_2 system the doming is small and towards the oxygen ligand. This is consistent with the known allosteric mechanism of

96

hemoglobin, where the binding of oxygen causes the iron atom to move away from the imidazole into the plane of the porphyrin ring.

Overall, the structural changes between the deoxy- and oxy- model systems are a decrease in the Fe-His, Fe-N_P and N_P-N_P bond lengths, indicating a contraction of the porphyrin ring upon bonding with O_2. It is interesting to note that the O-O bond length of the oxyheme model system, 1.275 Å, falls between the computed bond lengths of dioxygen, 1.216 Å, and superoxide, 1.360 Å. This is to be expected since back donation from the iron porphyrin system into the oxygen increases the O-O bond length to give the superoxide character, thus activating the oxygen.

The binding energy, abbreviated as BE, of O_2 to the porphyrin system is defined as the energy difference between the infinitely separated reactants and the bound system:

$$BE = \left(E_{FePL} + E_{O_2} \right) - E_{FePL-O_2} \qquad\qquad \textbf{5.1}$$

In this way, a positive value of BE indicates favourable binding of O_2 to the FePL model system.

The binding energies computed herein are compared to the experimental binding energies determined from dissociation barriers and temperature dependence studies for myoglobin. The experimental Gibbs binding energy (ΔG) and enthalpy change (ΔH) at 298 K are determined to be 8.0 kcal·mol^{-1} and 12.6 kcal·mol^{-1}, respectively.[146,147] For the heme model system, the oxygen binding energy is computed to be exergonic by 9.9 kcal·mol^{-1} and exothermic by 12.7 kcal·mol^{-1}. This is in excellent agreement with the experimental results, just slightly overestimating the oxygen binding to heme. It should be noted that no protein environment is included in our system. The heme pocket in myoglobin and hemoglobin is hydrophobic with the exception of the distal histidine

which is thought to have a stabilizing effect on the binding energy of O_2 via a hydrogen bond. Thus, the protein effect is largely attributed to the stabilizing effect of the distal histidine residue. The effect has been estimated from experimental studies to be 2.5-3.8 kcal·mol^{-1}.[146,165] Even when the computed results are corrected for the protein effect, the B97-D density functional approximation is still in excellent agreement with the experimental results. This study focuses on the relative binding energies upon substitution at the axial amino acid ligand, thus the protein effect is assumed to be consistent, therefore no corrections are used herein.

5.3.2 *Amino Acid Substitution*

The seven amino acids chosen for substitution at the axial ligand site in the porphyrin system are: arginine (Arg), cysteine (Cys), glutamic acid (Glu), histidine (His), methionine (Met) and tyrosine (Tyr). The abbreviation used herein is given in parentheses. The optimized structures for the deoxy- and oxy-iron porphine systems are shown in Figure 5.3. In the case of arginine, cysteine, histidine and tyrosine, the deprotonated forms of the amino acid are studied. This is consistent with physiological conditions where the metal cation, hydrophobic environment and the helical macrodipole of the protein environment can all act to lower the pKa value of the side chain resulting in the presence of the deprotonated species *in vivo*.[82,166–171] For computational efficiency, the protein backbone of the amino acid has not been included. It has been previously shown that exclusion of the amine and carboxylic acid groups does not significantly impact the structure or binding energies of these systems.[155]
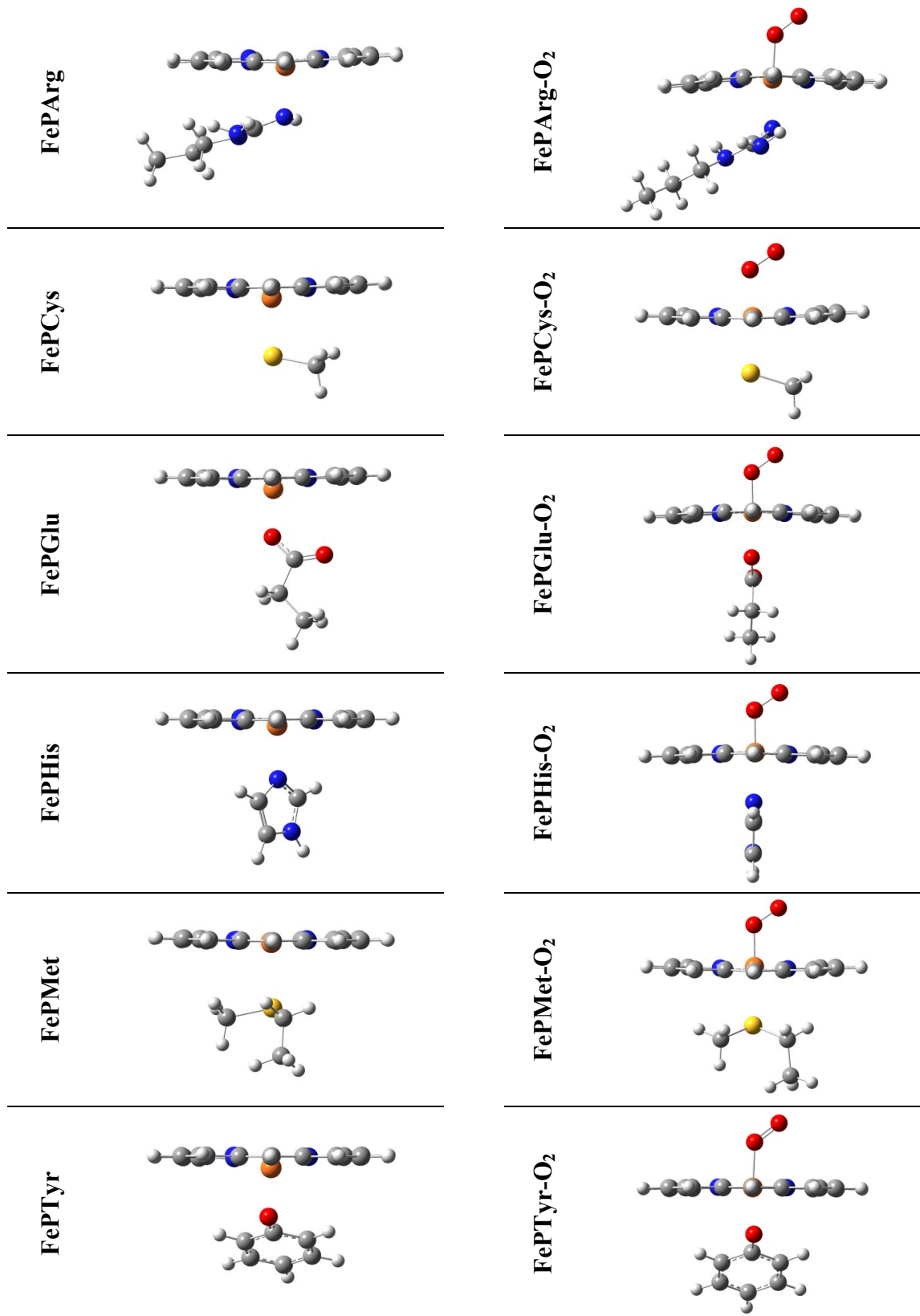
Figure 5.3. Optimized geometries for the FePL and FePL-O$_2$ model systems.

As shown in Chapter 4, range-separated functional approximations are better at predicting the correct ground state for the iron porphine system. Thus, the ωB97X-D density functional approximation was employed to assist with determining the correct ground state in the amino acid substituted systems. For each of the FePL systems, three spin states were computed, S = 0, 1 and 2. For all systems, the singlet states are significantly higher in energy, and do not represent the ground state. Interestingly, between the triplet and quintet state of the deoxy systems the spin state whose structure exhibits the greatest doming was always found to be the ground state. The quintet state is the ground state for the Arg, Cys, Glu, His and Tyr systems. The triplet is the ground state for the Met systems. The high-spin ground state of the Cys system is supported by experimental evidence for cytochrome P450cam, where cysteine acts as the axial ligand to the heme system.[172,173] It should be noted that in all cases the triplet and quintet states are close in energy, within 5 kcal·mol^{-1} of each other. Therefore, the ground state may be incorrectly predicted for some systems since the presence of solvent or the protein environment would have an effect on the ground state of these systems.

Structural parameters for the deoxy-systems are shown in Table 5.3 and are compared with experimental results, where available, in Table 5.4. The theoretical data from another study that employed the B3LYP density functional approximation, uses the same model system to model the histidine residue and a simpler model system for cysteine, with a thiol group in the axial position.[130] Relative to the results obtained with B3LYP, the B97-D functional yields good predictions for the histidine and cysteine systems. The only exception is the under-predicted doming for histidine, where B3LYP over-predicts the doming. However, the doming may be influenced by the protein

environment, as the calculated result is in excellent agreement with the doming reported for myoglobin. The under predicted doming is not ubiquitous, as the doming is over predicted for the cysteine and tyrosine systems. In general, the computed Fe-L bond lengths are longer than experiment which is to be expected since the calculations are in gas phase and the experimental data are from crystallographic data.

Table 5.3. Structural parameters (Å) for the deoxy-iron porphyrin systems.

L in FeP-L	Fe-L	Doming	Fe-N_P	N_P-N_P
Arg	2.13	-0.319	2.09	4.14
Cys	2.35	-0.432	2.11	4.14
Glu	1.98	-0.425	2.11	4.13
His	2.13	-0.282	2.08	4.14
Met	2.60	-0.127	2.01	4.01
Tyr	1.94	-0.448	2.11	4.13

Table 5.4. Comparison of theoretical structural parameters (Å) to experimental results for analogous naturally occurring systems.

	Fe-L	Doming
FePHis	2.128	-0.282
[a]**Exp.**[94]	2.06(2)	-0.36(5)
[b]**Exp.**[139]	2.15(1)	-0.290(18)
[c]**Theoretical – FePHis**[130]	2.168	-0.408
FePCys	2.348	-0.432
[d]**Exp.**[174]	2.20	-0.40
[e]**Theoretical – FeP-SH**[130]	2.480	-0.595
FePTyr	1.94	-0.448
[e]**Exp.**[175]	1.77(1)	-0.24(2)

[a]Crystal structure of human deoxy-hemoglobin. [b]Crystal structure of sperm- whale myoglobin. [c]Data from a theoretical study employing B3LYP. [d]Crystal structure of cytochrome P450cam. [e]Crystal structure of human erythrocyte catalase.

As previously noted, the magnitude of the doming is dependent upon spin state, and increases from the triplet to the quintet states. There is no correlation between the

donor atom: either N, O, or S; and the magnitude of the doming. Larger doming is correlated with longer Fe-N$_P$ bonds, which is to be expected. The size of the iron pocket, defined by the N$_P$-N$_P$ distance, is most greatly affected by the spin state. In the Met system, with a triplet ground state, there is a smaller N$_P$-N$_P$ distance. All other systems have quintet ground states and larger N$_P$-N$_P$ distances.   The bond distance between the coordinating atom of the amino acid ligand and the iron centre of the porphyrin does correlate with the donor atm. The systems from shortest to longest Fe-L bond are: Tyr, Glu, His, Arg, Cys then Met. In other words, the oxygen coordinating systems have the shortest Fe-L bonds, while the sulphur coordinating systems have the longest Fe-L bonds and the N coordinating system are between these bond lengths. This ordering is to be expected based on van der Waals radii of the atoms. Bond length should not be confused with bond strength, which is assessed by evaluating the electron density at the bond critical point between the bonded atoms, shown in Table 5.5. The doming does show correlation to the bond strength. Doming is largest in systems with the strongest bonds to the amino acid ligand, characterized by a greater electron density at the Fe-L bond critical point. This supports previous conclusions in Chapter 3 that doming is largely an effect of the interaction between the iron and the axial ligand.[85] The electron density at the Fe-N$_P$ bond critical point is correlated to the Fe-N$_P$ bond distances in Table 5.3, with the triplet system, Met, having the shortest bonds and greatest electron density.

Table 5.5. QTAIM atomic charges (au) and electron density at the bond critical points, ρ_{BCP} (au), for the deoxy-iron porphyrin systems.

L in FePL	Charge		ρ_{BCP}	
	Fe	L	Fe-L	Fe-N$_P$
Arg	1.41	-1.11	0.0664	0.0761
Cys	1.34	-0.05	0.0707	0.0722
Glu	1.45	-1.11	0.0833	0.0708
His	1.41	-1.07	0.0663	0.0768
Met	1.17	-0.04	0.0423	0.0860
Tyr	1.45	-1.08	0.0926	0.0711

The atomic charges calculated using QTAIM, reported in Table 5.5, show that iron is least electropositive in the Met system, the only ground state triplet system. In other words, in this system more electron density is transferred to the iron. By comparing to the other ligands, this electron density appears to be coming from the porphine ring, as there is the greatest electron density between the porphine and the iron (Fe-N$_P$) for Met, while less electron density is coming from the ligand interaction, with the least electron density between the iron and the coordinating atom (Fe-L) for Met. Thus, Met interacts more strongly with the porphine ring, and is weakly interacting with the ligand. The other systems, which are high-spin, have a greater interaction with the ligand. Cysteine in an interesting case, despite the anionic nature of the ligand the charge of the ligand is among the least negative. Thus, a significant amount of electron density must be transferred to the iron and porphine ring via the ligand interaction.

For the oxygen bound systems, the Cys, Glu, His and Met substituted systems have a singlet ground state. The Arg and Tyr substituted systems have a triplet ground state. To determine these ground states oxygen stretching frequencies, which should

approach the superoxide stretching frequency, chemical intuition, and comparison with higher basis set calculations, were employed to determine the most likely ground state. In the case of arginine, this is supported by experimental evidence of high-spin six-coordinated heme systems with an arginine axial ligand.[176] As previously discussed, the open shell singlet ground state of the histidine system is also supported experimentally. Structural parameters for the oxy-systems are shown in Table 5.6.   The same trend between the Fe-L distance and the coordinating atom observed in the deoxy system, exists in the oxy systems.   In other words, the oxygen coordinating systems have the shortest Fe-L bonds, following by nitrogen and then sulphur coordinating systems, consistent with the van der Waals radii of the atoms. This trend is not observed for the Fe-O distances. The shortest Fe-O distances are for the Glu, His and Met systems, which all have different coordinating atoms. In all cases, there is minimal doming in the oxy system, with all systems now domed towards the oxygen atom by less than 0.1 Å. Other similarities include the iron pocket, with all systems having Fe-N_P and N_P-N_P distances that are only vary by 0.01 Å with respect to one another.

Table 5.6. Structural parameters (distances in Å, angles in °) for the oxy-iron porphine systems. Dioxygen and superoxide are also included for comparison.

L in FePL-O_2	Fe-L	Fe-O	O-O	∠FeOO	Doming	Fe-N_P	N_P-N_P
Arg	2.10	1.86	1.27	131.3	0.018	2.01	4.04
Cys	2.31	1.95	1.29	121.2	0.035	2.02	4.05
Glu	1.99	1.79	1.29	125.1	0.039	2.02	4.05
His	2.08	1.85	1.28	121.0	0.053	2.02	4.04
Met	2.45	1.77	1.27	123.4	0.078	2.02	4.04
Tyr	1.95	1.89	1.29	129.9	0.007	2.02	4.05
O_2			1.22				
O_2^-			1.36				

The electron density analysis and atomic charges, calculated using QTAIM for the oxy systems, are reported in Table 5.7. There is a direct correlation between the electron density at the bond critical point between iron and oxygen and the Fe-O distances reported in Table 5.3, with greater electron density resulting in shorter bonds. The electron density between the iron and the ring, characterized by ρ_{BCP} at Fe-N, is very similar for all systems. This supports the observation from the bond distances that all systems, upon binding oxygen, had similar iron pocket geometries and interactions. The electron density between the coordinating atom of the amino acid and iron gives an indication of the interaction strength. The amino acid ligands in order of increasing interaction strength with iron are: Met, Arg, Cys, His, Glu, Tyr. Again, this is not the ordering of Fe-L distances from Table 5.6, where the distance varied based on atom type.

The oxygen activation ability of a system is related to the electron density at the bond critical point between the two oxygen atoms, ρ_{BCP}, with a lower electron density corresponding to the greater oxygen activation. This is evident from the values reported for dioxygen and superoxide in Table 5.7. It is interesting to note that the correct trend of oxygen activation is reproduced for the histidine and cysteine systems. It is known that the cysteine system is a better oxygen activator, due to its role in the cytochrome system and other experimental evidence[122,156,160] and this is shown in Table 5.7 where the oxygen activation of cysteine is greater than the histidine model system. It has been previously suggested that a weaker Fe-L bond leads to greater superoxide character, however, this is not consistently observed in this study even when comparing ligands with the same coordinating atom-type.[137]

Table 5.7. QTAIM charges (au) and electron density at the bond critical points, ρ_{BCP} (au), for the oxy-iron porphine systems. Dioxygen and superoxide are also included for comparison.

L in FePL-O_2	Charge				ρ_{BCP}			
	Fe	L	O^a	O^b	Fe-L	Fe-N	Fe-O	O-O
Arg	1.30	-1.06	-0.25	-0.17	0.0698	0.0841	0.1105	0.442
Cys	1.22	-0.34	-0.28	-0.25	0.0708	0.0827	0.0932	0.423
Glu	1.35	-1.05	-0.25	-0.25	0.0788	0.0832	0.1400	0.425
His	1.32	-1.07	-0.23	-0.17	0.0736	0.0840	0.1230	0.443
Met	1.24	-0.01	-0.20	-0.18	0.0486	0.0845	0.1499	0.448
Tyr	1.35	-1.01	-0.29	-0.26	0.0826	0.0885	0.1054	0.420
O_2			0.00	0.00				0.524
O_2^-			-0.5	-0.5				0.349

O^a is the proximal oxygen atom. O^b is the distal oxygen atom.

The oxygen coordinating systems, Glu and Tyr, have strong interactions with the iron, characterized by greater ρ_{BCP} at Fe-L. This corresponds to an increased ability to activate the O_2, evident from the low value of ρ_{BCP} for the Fe-O and O-O bonds, relative to most of the other systems. The lower electron density at the O-O bond critical point is indicative of superoxide character, as shown in the difference between O_2 and O_2^-, also shown in Table 5.7. This corresponds to longer O-O bonds, as shown in Table 5.6, and greater negative charge on the oxygen atoms, as shown in Table 5.7. These characteristics are observed in the Glu and Tyr systems. Interestingly, Cys also exhibits these characteristics making it an excellent candidate for increased oxygen activation. The other sulphur coordinating system, Met, as well as Arg, have oxygen activation properties similar to the histidine reference system.

The binding energy, denoted *BE*, for the amino acid substituted systems is calculated as shown in Equation 5.1. The calculated values are reported in Table 5.8.

106

The Gibbs energy, ΔG, and enthalpy change, ΔH, are reported for comparison with experimental results. The results are in good agreement with the histidine model system, as previously discussed.

Table 5.8. Calculated Gibbs binding energy and enthalpy change for oxygen binding to FePL at 298 K (kcal·mol^{-1}). The binding of O_2 is exergonic and exothermic, however the values are shown as positive quantities as is convention.

L	Binding Energy	
	ΔG	ΔH
Arg	6.7	7.2
Cys	10.2	13.0
Glu	3.2	6.1
His	9.9	12.7
Met	3.6	8.2
Tyr	6.7	9.0
[a]Exp.[147]	8.0	12.6

[a]O_2 binding to native myoglobin.

It is useful to consider structural changes between the deoxy- and oxy-iron porphine systems and these changes are reported in Table 5.9. The changes are from the deoxy to the oxygen bound system, thus, negative changes indicate a decrease in distance upon binding. It is also useful to consider changes in the QTAIM properties between the deoxy- and oxy-iron porphine systems. These are shown in Table 5.10 and are taken as changes upon dioxygen binding to the porphyrin, thus a negative change in electron density indicates an increase in electron density upon binding. In this way, negative changes for charge indicate more negative atomic charges and for ρ_{BCP} stronger bonding interactions.

Relative to the histidine model system, it is interesting to note that cysteine, in addition to being better at activating the oxygen molecule, has a greater binding affinity for oxygen, albeit only 0.3 kcal·mol^{-1} greater. Glutamic acid has similar properties, to a lesser extent. Tyrosine and arginine exhibit similar oxygen affinity, approximately 3 kcal·mol^{-1} less than histidine, yet exhibit different oxygen activation abilities as discussed above. Glutamic acid has a lower oxygen affinity, despite having significant oxygen activation ability. Methionine also has a lower oxygen affinity relative to histidine, which is counterintuitive since it forms the strongest interaction with oxygen, shown in Table 5.7. This can be explained as an entropic effect since the enthalpy change, ΔH, for binding is significantly greater. Methionine has the weakest interaction with iron and the porphine ring, shown in Table 5.5, and upon binding this interaction is strengthened.

Table 5.9 shows that the magnitude of the decrease for Fe-L distance is greatest for methionine. Methionine has the weakest interaction with the porphine ring in the deoxy system, however, the interaction is strengthened upon binding, shown by the $\Delta \rho_{BCP}$ for the Fe-L distance in Table 5.10. However, this interaction appears to be at the expense of the electron density within the porphine ring as it is the only system that exhibits an increase in porphine ring geometry upon binding, exhibiting positive changes for Fe-N_P and N_P-N_P in Table 5.9. Accordingly, there is a decrease in electron density at the $\Delta \rho_{BCP}$ for the Fe-N_P bonding interaction, in Table 5.10. These differences, relative to the other systems, may contribute to the greater entropy change experienced by the methionine system upon oxygen binding, evident from the large difference in ΔH and ΔG for binding. The decrease in electron density explains the high electron density at the

Fe-O bond critical point, as methionine exhibits the strongest interaction with dioxygen, as previously mentioned.

Table 5.9. Changes in the structural properties upon oxygen binding to FePL. The changes are represented as the difference in distance (Å) and the percent change (%). A negative change indicates a decrease in the distance upon binding with O_2. Systems are shown in order of increasing BE, based on the Gibbs energy change, ΔG.

	Δ Fe-L		Δ Doming		Δ Fe-N$_P$		Δ N$_P$-N$_P$	
L	Å	%	Å	%	Å	%	Å	%
Glu	0.01	0.4	-0.39	-91	-0.08	-3.9	-0.08	-2.0
Met	-0.10	-3.8	-0.05	-38	0.02	0.8	0.03	0.6
Arg	-0.04	-1.7	-0.30	-95	-0.10	-4.9	-0.10	-2.3
Tyr	0.01	0.4	-0.44	-98	-0.07	-3.4	-0.09	-2.1
His	-0.05	-2.4	-0.23	-81	-0.06	-2.4	-0.10	-2.3
Cys	-0.03	-1.5	-0.40	-92	-0.10	-3.7	-0.09	-2.2

Table 5.10. Changes in the QTAIM charges (au) and electron density at the bond critical points, ρ_{BCP} (au), upon oxygen binding to FePL. A negative change indicates an increase in electron density upon binding with O_2. Systems are shown in order of increasing BE, based on the Gibbs energy change, ΔG.

	Δ Charge			Δ ρ_{BCP}	
L	Fe	L	N$_P$	Fe-L	Fe-N$_P$
Glu	-0.10	0.05	0.07	0.0045	-0.0124
Met	0.07	0.04	0.01	-0.0062	0.0015
Arg	-0.11	0.05	0.07	-0.0034	-0.0080
Tyr	-0.10	0.07	0.07	0.0100	-0.0174
His	-0.10	0.03	0.07	-0.0066	-0.0076
Cys	-0.12	0.13	0.07	-0.0039	-0.0105

In the case of Arg, Cys, and His, upon binding oxygen there is shift of electron density away from the N$_P$ and L coordinating atoms to the iron centre. This is evident from the changes in atomic charge, shown in Table 5.10, where the L and N$_P$ atoms

become more positive and iron more negative. This corresponds to a greater electron density at the Fe-L and Fe-N_P bond critical points and accordingly, shorter Fe-L, Fe-N_P, and N_P-N_P bonding interactions, exhibited by negative changes in Table 5.9. The shorter bond distances are likely a result of stronger electrostatic interactions between the atoms. Not surprisingly, these systems exhibit similar activation of oxygen.

The amino acid ligands with oxygen coordinating atoms, Glu and Tyr, exhibit different affects upon oxygen binding. Upon binding oxygen, electron density shifts away from the L and N_P atoms and there is an increase in negative charge on the iron atom, as with Arg, Cys and His. However, this weakens the Fe-L bonding interaction and significantly strengthens the interactions with the porphine ring. This differs from the Arg, Cys and His systems where these interactions were all strengthened. Despite modest binding energies, Glu and Tyr yield significant superoxide character in the bound oxygen and, thus, have great oxygen activation potential. These systems must provide accessibility of electron density to the dioxygen to facilitate the oxygen activation.

In order to further evaluate the binding energy, it is useful to consider the occupied molecular orbitals that participate in bonding. Within DFT, the Kohn-Sham orbitals have been shown to provide qualitative insight to aid in the explanation of chemical phenomena.[177] The deoxy-iron porphine systems are all open shell, with triplet or quintet multiplicities in the ground state, thus it is useful to consider the highest energy singly-occupied molecular orbitals. The highest energy singly-occupied molecular orbital and second highest energy singly-occupied molecular orbital, denoted SOMO and SOMO-1, respectively, are shown in Figure 5.4. Also of interest is the highest energy SOMO of the oxy-iron porphine systems which are shown in Figure 5.5.

110
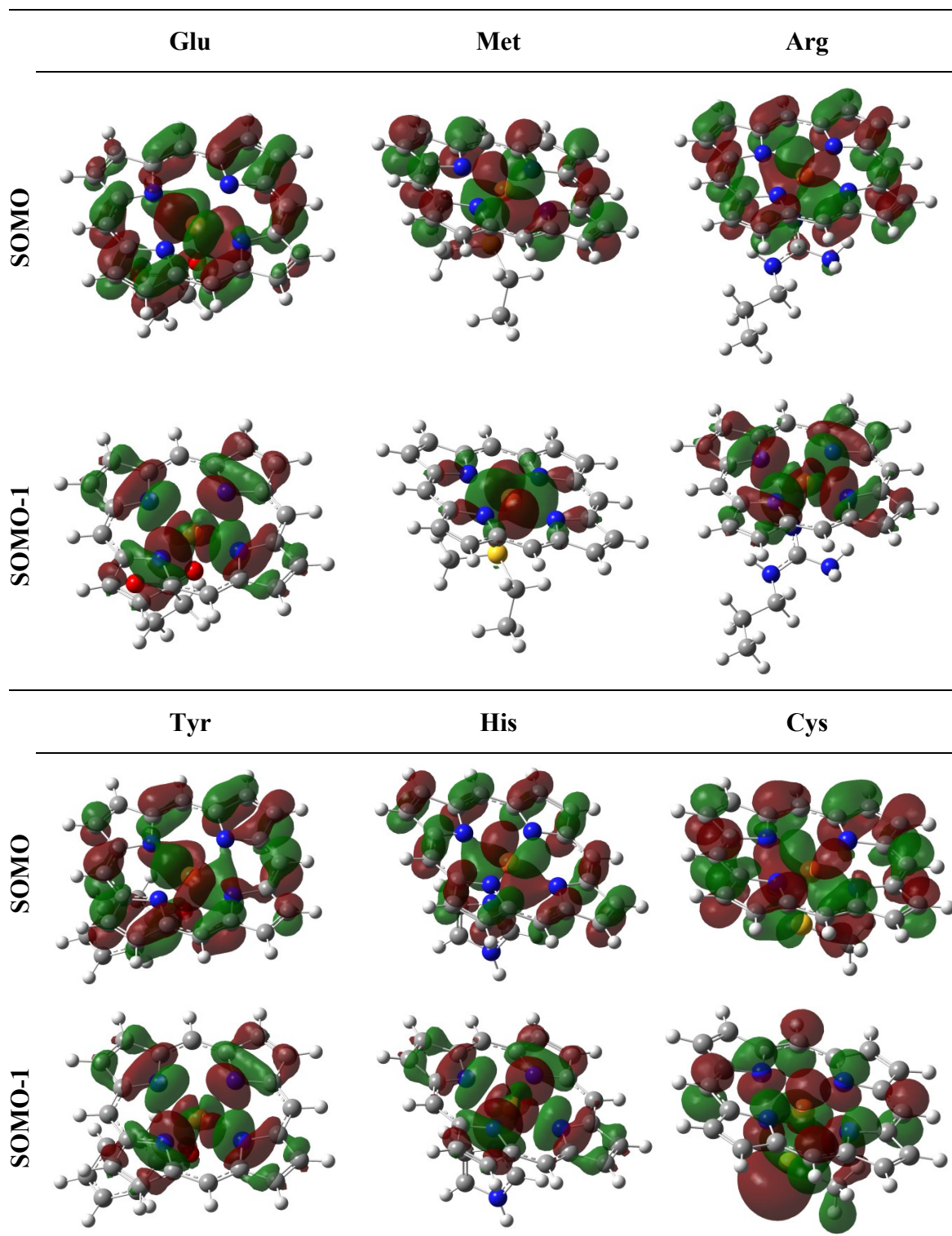
Figure 5.4. Highest energy singly-occupied molecular orbital (SOMO) and second highest energy singly-occupied molecular orbital (SOMO-1) for the FePL systems, with an isosurface of 0.02 au. The positive and negative regions of the molecular orbital are represented as red and green, respectively. Systems are shown in order of increasing BE, based on the Gibbs energy change, ΔG.
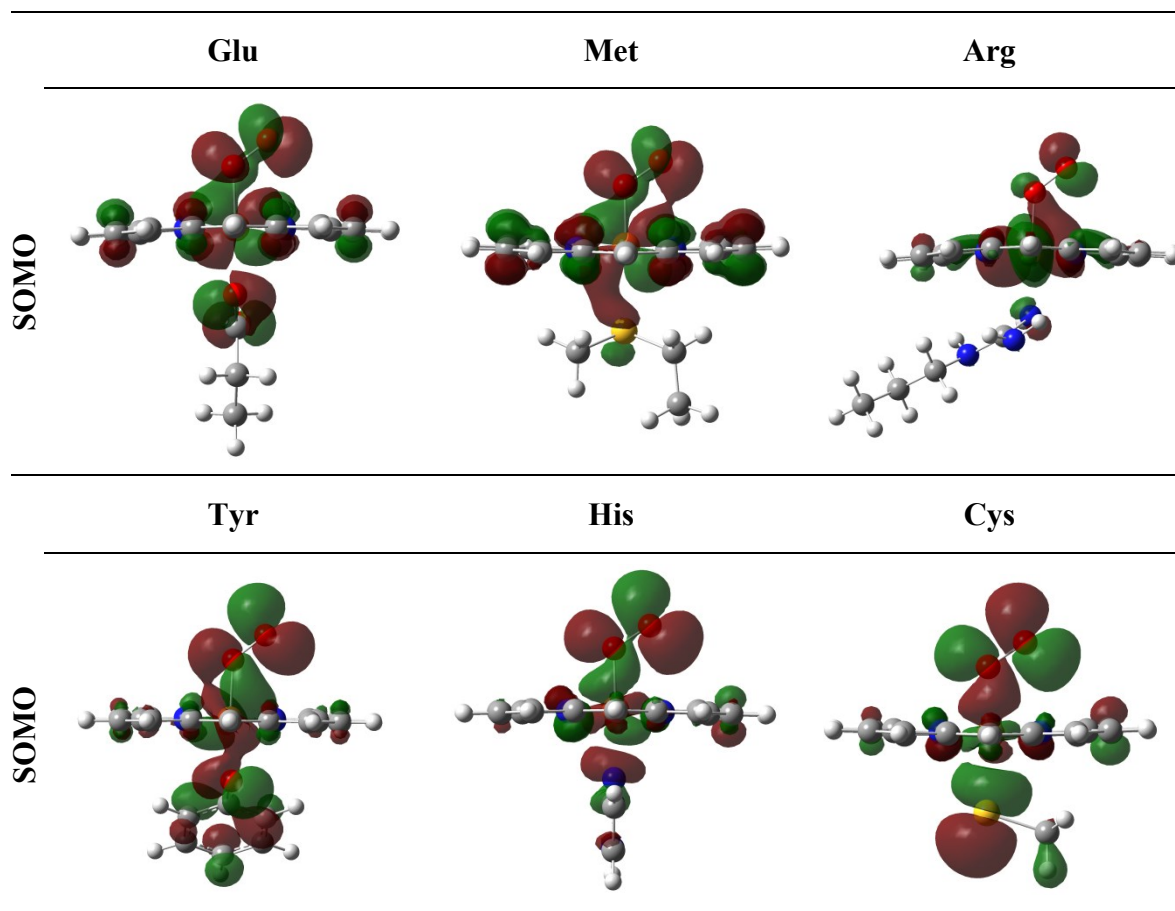
Figure 5.5. Highest energy singly-occupied molecular orbital (SOMO) for the FePL-O$_2$ systems, with an isosurface of 0.02 au. The positive and negative regions of the molecular orbital are represented as red and green, respectively. Systems are shown in order of increasing BE, based on the Gibbs energy change, ΔG.

As discussed above, upon binding to oxygen Arg, His and Cys have similar electronic and structural affects. Not surprisingly, the SOMO of all three systems, shown in Figure 5.4, are similar. The orbitals are largely delocalized over the porphine ring and the *d*-orbital on the iron atom that has a positive and negative lobe positioned towards the oxygen binding site. The SOMO-1 for Arg and His are also similar, with the *d*-orbital on the iron positioned towards the nitrogen atoms of the porphine ring. In the SOMO-1 the *d*-orbital is contracted with greater orbital contribution coming from the porphine ring. However, in the Cys system the SOMO-1 has a d_{z^2}-orbital positioned towards the

oxygen binding site. This explains the stronger *BE* for the Cys system and the ability of Cys to more successfully activate oxygen. This can be seen in Figure 5.5, where the SOMO for Cys and His have a large anti-bonding orbital localized on the oxygen, leading to decreased electron density at the ρ_{BCP} for the O-O bonding interaction. In the case of Arg, the orbital on the oxygen is smaller and there is interaction between the orbital on the proximal oxygen and iron. This suggests that there is more electron density contributed to the Fe-O interaction and less contributing to the antibonding O-O interaction, leading to decreased activation in the Arg system.

In the case of Met, the SOMO is similar to the other systems, largely delocalized over the porphine ring and having a *d*-orbital on the iron atom that has a positive and negative lobe positioned towards the oxygen binding site. However, the SOMO-1 is localized on the iron atom having lobes pointed towards the nitrogen atoms of the porphine ring. Upon binding this leads to modest overlap with the binding oxygen and significant overlap between the iron and the ligand, shown in the SOMO of the oxy-iron system in Figure 5.5. This supports the previous discussion from the electronic and structural results for Met. There is also orbital overlap between the oxygen and the ring, leading to decreased oxygen activation as in Arg.

The SOMO of the Glu and Tyr systems are similar. This is not surprising considering the similarities in electron density and geometric changes upon binding between these systems. The SOMO for both systems is again largely delocalized over the porphine ring, however, the *d*-orbital on the iron atom is not aligned directly toward the oxygen binding axis. Instead, the orbital is tilted with the negative and positive lobes positioned between the plane of the porphine ring and the oxygen binding axis, as shown

113

in Figure 5.4. The SOMO-1 for both Glu and Tyr is similar to the Arg and His systems, with the lobes of the orbital on iron facing the nitrogen atoms. The orbital contribution from iron is significantly contracted, relative to the SOMO, and thus there is greater orbital contribution in the SOMO-1 from the porphine ring.

Upon binding, the SOMO of the oxygen bound Glu and Tyr systems, shown in Figure 5.5, exhibit similar interactions to the Arg and Met systems, where the orbitals on the oxygen interact modestly with the iron and porphine ring. However, there is only orbital overlap between the iron and the closest oxygen, and not the distal oxygen atom as is observed in Met. It is interesting to note that in the oxygen bound systems, the three best oxygen activators, Cys, Glu and Tyr, all exhibit significant orbital contribution from the ligand in the SOMO. This supports the idea that the ligand plays an important role in electron density transfer to the oxygen, and thus oxygen activation. In contrast, Arg, His, and Met show a greater orbital contribution in the SOMO from the porphine ring, as oppose to the ligand, and exhibit weaker oxygen activation properties. Also in support of this idea is that of the three best oxygen activators, Glu is the weakest and also exhibits the weakest oxygen binding. In comparing the SOMO of Cys, Glu and Tyr, in Figure 5.5, the Glu system has the smallest contribution from the ligand. It is also the system that most resembles the Arg, His and Met systems, with respect to orbital contribution from the porphine ring. Overall, the superior oxygen activating ability of Cys and Tyr is evident from the large, well-defined anti-bonding orbitals on the oxygen for these systems, pictured in Figure 5.5.

A previous study of oxygen binding to porphyrin systems with ligated imidazole analogues concluded that O_2 binding is favoured when the coordinating atom of the axial

ligand carries more negative charge.[130] The proposed explanation is that more electron density is available to the porphyrin system and thus to the O_2 molecule, making the oxygen more active and allowing for an increase in back-donation to the Fe-O bond. This study looked at neutral nitrogen-containing ligands and the anionic thiol group. Our results are consistent in showing that the thiol group has a greater affinity for oxygen; however, the Glu and Tyr systems are also anionic but have significantly lower affinity for oxygen. Furthermore, the binding energy and oxygen activation ability do not correlate. In fact, systems with similar binding energies have very different activation abilities. Thus, the charge of the ligand is not the only factor affecting binding energy and oxygen activation. In fact, even the results presented here for the nitrogen containing systems are not consistent. Instead, the arginine system shows a weaker affinity for oxygen despite a more negative charge on the coordinating nitrogen atom of the ligand, as shown in Table 5.5. Thus, more electron density on the axial ligand does not necessarily ensure this transfer. It is recognized that these systems are more structurally diverse than the systems studied in previously.[130] Nonetheless, it is evident that simply correlating the charge on the coordinating atom to binding energy may suffice for both structurally and electronically analogous systems, however, this cannot be extended to larger more diverse ligands.

It should be noted that an experimental study assessing the catalytic effect of substituting cysteine and tyrosine for the proximal histidine in human myoglobin concluded that cysteine enhances heterolytic O-O bond cleavage, whereas tyrosine has little effect on the catalytic activity relative to histidine.[160] Based on the results presented here, this effect must be due to the increased oxygen activation of cysteine. Both Cys and

His have similar oxygen binding energies, with cysteine exhibiting only a slight increase in oxygen affinity, while Tyr has a lower binding affinity. However, both Cys and Tyr show significant oxygen activation ability as evident from the charge transfer to the oxygen. Thus, the balance of increased oxygen activation and decreased binding affinity in Tyr yields no significant change in the catalytic activity of tyrosine. It follows that the Cys system, which exhibits a binding affinity similar to the His system, and an increased oxygen activation ability would produce an increase in catalytic activity.

5.4   Conclusions

For the systems studied here there is no clear correlation between charge, interaction strength, or changes in structural or electronic features of the iron porphine systems with oxygen activation or binding energy. Instead, multiple components and features of the binding reaction must be considered in order to explain the results computed. These include interaction strength between the ligand and iron porphine system, electron density transfer between the ligand, iron, porphine ring, and oxygen, and molecular orbital contributions from the orbitals involved in the binding reaction. Overall, it is hypothesized that a balance between a sufficiently strong bond with the axial ligand while maintaining the ability of the iron to transfer electron density to the O_2 molecule is critical for these systems *in situ*.

One of the goals of this study was to provide inspiration for the design and modification of proteins, or smaller synthetic analogues to mimic their function, for a range of applications, including catalysis and therapeutics. In experimental methods it is often difficult to rationally design a protein for a specific function due to the multitude of existing functions and complexity of protein structure that have accumulated through

116

evolution. It is the hope that computational studies can elucidate the observed effects of site-directed mutagenesis and guide further exploration, while contributing to the principles of the growing field of protein engineering. As such, a number of amino acid substitutions are noteworthy. Relative to the histidine system, Glu, Tyr and Cys provide increased oxygen activation ability making them ideal candidates where oxidants are sought. This is a common target in catalysis where, for example, the activated O_2 can abstract a hydrogen atom. Cysteine provides an interesting modification to the histidine system of myoglobin and hemoglobin. It has a greater binding affinity for oxygen and upon binding, activates the oxygen with significant superoxide character. Similarly, tyrosine provides great oxygen activation ability, while maintaining similar affinity for oxygen as the myoglobin or hemoglobin systems. If instead decreased oxygen affinity and activation is targeted, methionine is a suitable candidate.

Chapter 6 : A Computational Investigation of Nitric Oxide Induced Oxidation of Oxyhemoglobin

6.1   Introduction

The benefits of artificial blood substitutes are numerous. Issues of blood type compatibility and blood borne diseases, such as HIV, do not exist for artificial blood substitutes. Issues such as cold storage and short shelf life would no longer be limiting, enabling blood transfusions to be performed in remote locations and at trauma sites. A synthetic blood substitute may also aid those whose religious beliefs prohibit them from accepting donor blood. Ultimately, the development of an artificial blood substitute would reduce the overwhelming and unmet demand for donors.

The central aim in developing cell-free blood substitutes (CFBS) is to mimic hemoglobin's ability to bind oxygen. Despite decades of research in the field, the development of CFBSs is plagued by two problems: oxidation damage and vasoconstriction.[178,179] Oxidation occurs because hemoglobin degrades without the protective antioxidant enzymes present in the membrane of the red blood cell. Upon oxidation, hemoglobin breaks into two subunits that are cytotoxic. Several successful approaches to stabilize hemoglobin include: polymerizing hemoglobin molecules together via glutaraldehyde;[179] binding many polyethylene glycol molecules to a hemoglobin molecule to keep it from dissociating;[179] and conjugating hemoglobin to superoxide dismutase and catalase to protect it from potential oxidizers by reacting with superoxides and hydroxyl radicals.[180,181]

The latter problem of vasoconstriction remains a significant hurdle for the development of CFBSs. Although the effect is typically mild, it can induce heart attack

for those receiving emergency medicine. This shortcoming has been the failure of a number of CFBSs at clinical trials.[179] Many studies have shown that a depletion of nitric oxide from the wall of the vasculature results in constriction of the arterioles.[181–185] Since CFBSs are much smaller than red blood cells they can closely approach the surface of the vascular smooth muscle, binding irreversibly with nitric oxide, causing this depletion. Although both deoxy- and oxyhemoglobin have a high affinity for nitric oxide, oxyhemoglobin is the predominant form in arteries and thus has a more significant effect on nitric oxide scavenging.[182,186,187] Furthermore, the reaction of oxyhemoglobin with nitric oxide results in the formation of methemoglobin and nitrate. This ferric form of hemoglobin cannot transport oxygen, rendering the CFBS inactive. Despite its physiological importance, this reaction is poorly understood.[188]

Not surprisingly, myoglobin, whose structure closely resembles an individual subunit of hemoglobin has been found to act as a nitric oxide scavenger in the body. Oxy-myoglobin reacts with NO. resulting in an oxidized Fe (III) centre which is reduced by metMb reductase, thus acting as a catalyst in this cycle.[189–191] It has been suggested that the intermediate involves a peroxynitrite species bound to the iron centre.[187,192]

Experimental studies show the presence of free iron (III) porphyrin complexes in solution increases the rate of peroxynitrite decomposition to nitrate, at physiologically relevant temperature and pH.[193] Studies involving oxy-myoglobin and oxy-hemoglobin showed the presence of an iron (III)-peroxynitrite complex.[194,195] These studies detect neither a free peroxynitrite species nor an oxidized oxo-Fe(IV) species. Instead it is suggested that the peroxynitrite complex rearranges to nitrate without prior dissociation.

Experimental evidence, which employs protein engineering, showed limited success in modifying the distal pocket to inhibit the NO induced oxidation reaction.[187] Multiple amino acid substitutions where made to generate steric hindrance in the distal pocket, which led to moderate success in the α subunits of hemoglobin, while no inhibition was observed in β subunits. It is likely that the varied results for α and β subunits are due to the unequilvalent environment around the heme group. In the β subunit some amino acid residues overlap with the ligand binding site to a larger extent than in the α subunit, giving rise to different rate constants for some of the reactions of hemoglobin. In addition, it has been shown that the distal histidine residue plays an important role in discrimination between O_2 and CO.[146,165] Thus, additional caution must be taken in modification of the distal histidine to preserve O_2 specificity which provides an added challenge with this approach.

Ultimately, a greater understanding of the heme system is necessary in the development of future CFBSs. One route to overcome the problem of vasoconstriction would be to alter the reactivity of heme, allowing for the selective inhibition of unfavourable oxidation reactions, while maintaining moderate O_2 affinity. In this study, the effect of amino acid substitutions at the proximal histidine residue on the binding affinity of O_2 and NO with heme is investigated to gain insight into the electronics governing this region of the heme system.

6.2 Computational Methods

The model system employed in this chapter is analogous to that of previous chapters in this thesis. This not only provides consistency and continuity with the previous studies but is also computationally efficient for the chosen models employed

herein. One of the axial positions on the iron atom is occupied by dioxygen and the other by the ligand used to model the amino acid residue, which is denoted by L, as in the previous chapter. This system is shown in Figure 6.1 and is denoted as FePL-O_2, as in Chapter 5. The distal histidine is excluded and therefore the results represent the low-pH case, where the histidine is protonated and therefore does not participate in a hydrogen bond within the active site.
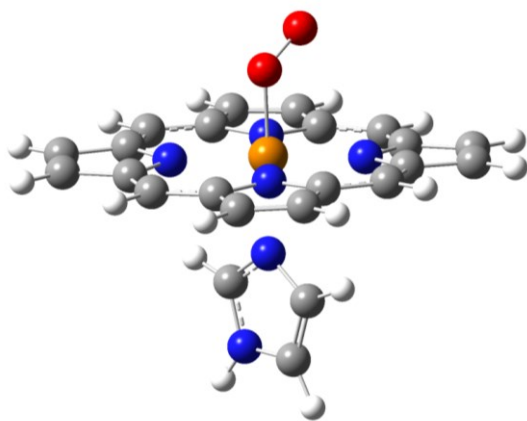
Figure 6.1. The oxy-iron porphine model system, shown here has a histidine ligand and thus is denoted FePHis-O_2. Carbon, nitrogen, oxygen and hydrogen atoms are shown as grey, blue, red and white spheres, respectively. The iron atom is shown in orange.

The ligands chosen to model the amino acid residue are also consistent with Chapter 5: arginine (Arg), cysteine (Cys), glutamic acid (Glu), histidine (His), methionine (Met) and tyrosine (Tyr). The abbreviation used herein is given in parentheses. In the case of arginine, cysteine, histidine and tyrosine, the deprotonated forms of the amino acid are studied. This is consistent with physiological conditions, as discussed in the previous chapter.

In this chapter, all calculations employing density functional theory methods were performed using the Gaussian 09 program package.[70] Geometry optimizations and frequency calculations were computed for all stationary points. The relative energies reported are corrected to the Gibbs energy (ΔG) at 298 K. Spin-unrestricted density

functional theory was used for all calculations, as all systems are either open-shell singlet or have a spin multiplicity greater than 1. Following from the previous chapter, the B97-D[65] density functional approximation has been employed to investigate the reaction mechanism of oxy-hemoglobin and NO yielding methemoglobin and nitrate. Direct methods for locating transition states (e.g. TS, QST2, QST3 options in Gaussian 09) as well as potential energy scans were used to probe the potential energy surface. The B97-D[65] density functional approximation was also employed for the second part of this study to investigate the effect of various amino acids in the axial position on the first step of this mechanism.

Pople-type basis sets were employed: 6-311+G(f) on iron, 6-311+G(d) on nitrogen, sulfur and oxygen, and 6-31G on carbon and hydrogen. The use of different basis sets within the complex was employed for computational efficiency, allowing for optimization of the geometries, while allowing for higher level calculation on the part of the system where binding occur.

The quantum theory of atoms in molecules, denoted QTAIM, which uses the integral of the electron density to map the chemical topology of a system, was used to explore the nature of the bonding environment. More specifically, atomic charges and the electron density at bond critical points were computed using the AIMAll software package.[112]

6.3   Results and Discussion

6.3.1 Reaction Mechanism

As previously discussed the mechanism for the nitric oxide induced oxidation of oxyhemoglobin is poorly understood. To investigate the mechanism of reaction between

oxy-hemoglobin and nitric oxide to form methemoglobin and nitrate, three potential mechanisms were probed based on experimental evidence. These three mechanisms are shown in Figure 6.2. The first step in all three mechanisms involves the addition of nitric oxide to the oxygen bound iron porphine systems, resulting in an iron (III)-peroxynitrite complex, which has been characterized experimentally.[182,192,194–196] This is analogous to the reaction of superoxide with nitric oxide.[197] This is consistent with the superoxide character of O_2 in oxyhemoglobin that has been reported theoretically herein and elsewhere[198] and experimentally.[199]

Mechanism 1 involves the subsequent generation of a free peroxynitrite species, suggested to exist in some experimental studies.[192] Although this pathway has been discounted in another study, this was under alkaline conditions, with a pH of 8.1, thus under physiological conditions free peroxynitrite may form.[187] For this reason, the formation of free peroxynitrite will not be excluded in this study.

Mechanism 2 investigates a potential isomerization of the peroxynitrite ligand while still interacting with the iron porphine system. This mechanism would also support the absence of an oxo-Fe(IV) complex in the reaction. Mechanism 3 proceeds via a oxo-Fe(IV) species, as suggested by experimental studies of iron porphyrin compounds in solution.[193,200] Despite the oxo-Fe(IV) species not being detected in stopped-flow spectrophotometric experiments with hemoglobin,[187,194,195] this mechanism has been suggested by others[201] and the oxo-Fe(IV) species is known to occur in accepted mechanisms for that family of cytochrome P450 enzymes.[202–204]
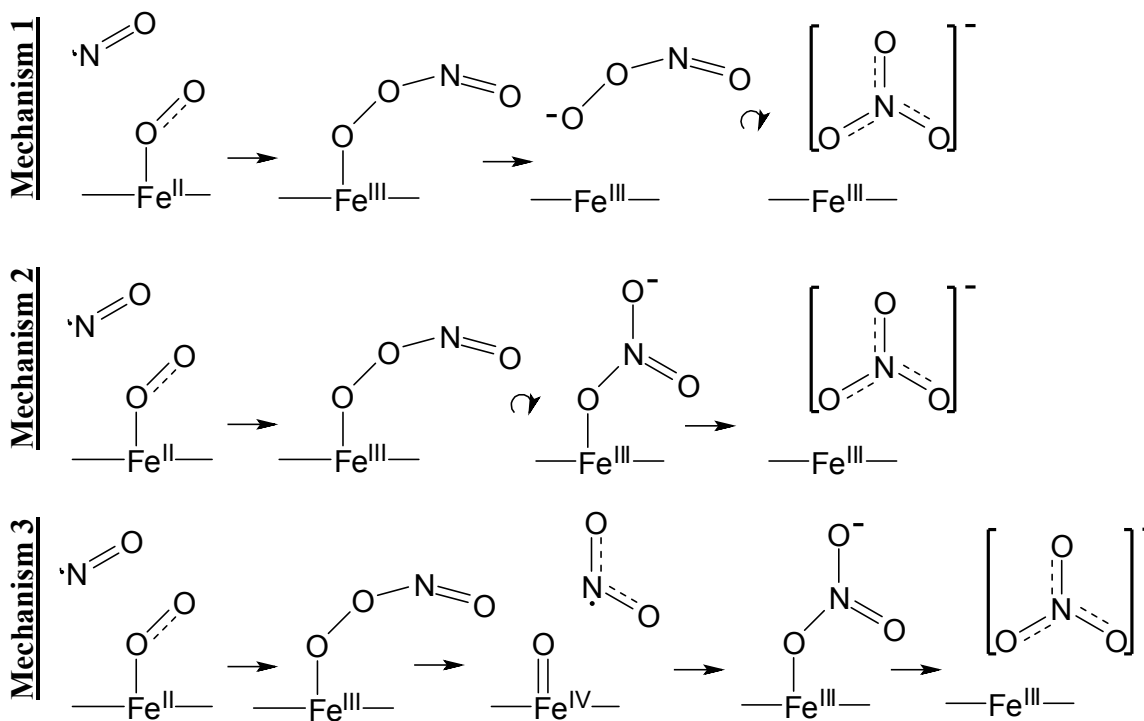
Figure 6.2. The three potential reaction mechanisms investigated for nitric oxide induced oxidation of oxy-hemoglobin. The porphyrin structure and histidine axial ligand are omitted for simplicity.

After considerable computational effort, a free peroxynitrite mechanism, as shown in mechanism 1 of Figure 6.2, was unable to be located on the potential energy surface. If dissociation between the peroxynitrite species and the iron porphine is attempted the favoured reaction pathway is the exchange of O_2 with NO to give the NO bound iron porphine, nitrosylhemoglobin, and free oxygen. This reaction has an estimated barrier of 9 kcal·mol^{-1} and is exergonic by approximated 14 kcal·mol^{-1}. However, these reactions are not significantly observed experimentally, nor are they the focus of this study.[196] The reaction between NO and oxy-hemoglobin is rapid and known to give stoichiometric quantities of methemoglobin and nitrate. In fact, O_2 replacement by nitric oxide is very low, even when patients are exposed to modest levels of NO.[205]

Also, peroxynitrite is a strongly oxidizing and nitrating species, however it was noted in the experimental results of Herold that only trace amounts of nitrated species were found, which suggests that a free peroxynitrite mechanism is likely not the primary mechanism.[195] It should be noted that peroxynitrite can form from the reaction between nitric oxide and molecular oxygen, albeit the reaction between nitric oxide and oxy-hemoglobin is estimated to be approximately 26 times faster.[196] Thus, free peroxynitrite may originate it this way.

On the mechanism where isomerization of the peroxynitrite ligand proceeds in a concerted manner, with no Fe(IV) species found, no feasible mechanism could be obtained. Scans of the potential energy surface gave large barriers to isomerization, ranging from 53 to over 500 kcal·mol^{-1}. It is possible that larger, more complex modelling may yield a lower barrier to isomerization. This may suggest interactions between the bound peroxynitrite species and the amino acid residues in the distal pocket. However, these effects are not captured in the current study.

A plausible concerted mechanism could not be obtained, in contrary to the experimental studies where no Fe(IV) species is detected. Thus, provided our model is sufficient, it must be the case that the Fe(IV) species must react too fast to be detected, thus does not accumulate above the detectable limit of the experiment.[194,195] This hypothesis is supported by the energetics of this step of the reaction, which has a very low barrier. Thus, mechanism 3 is the only plausible mechanism and the reaction profile is shown in Figure 6.3. The abbreviations used for the species involved in the mechanism are shown in Figure 6.4 and is used to report the energetics of the reaction in Table 6.1.
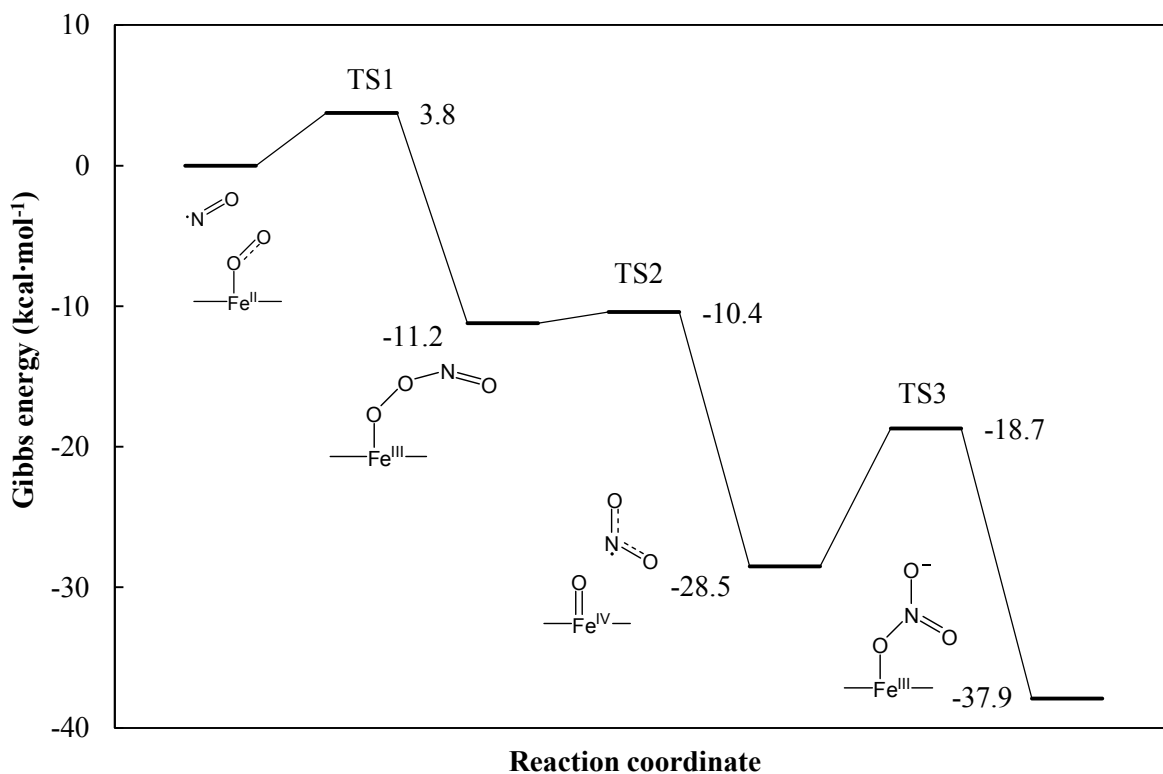
Figure 6.3. Gibbs energy surface for mechanism 3. Energies (kcal·mol^{-1}) are reported relative to the reactants.
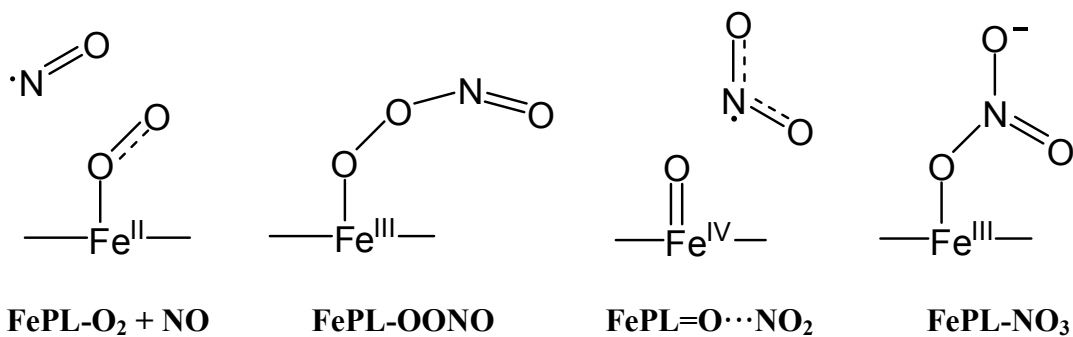
Figure 6.4. Minimum structures on the potential energy surface for the proposed reaction mechanism, with abbreviations used herein.

In the first step of the proposed reaction mechanism, the open-shell singlet FePHis-O$_2$ species exhibits superoxide character and reacts with the NO radical to form the peroxynitrite bound intermediate, FePHis-OONO. For the hemoglobin model, where

the axial ligand is imidazole, the reaction is exergonic by 11.2 kcal·mol^{-1}. The reaction

barrier for this reaction is 3.8 kcal·mol^{-1}, which results from the entropic barrier since the

transition state has an enthalpy 5.6 kcal·mol^{-1} lower than the reactants. Thus, at 298K the

entropic barrier is 9.4 kcal·mol^{-1} and the change in entropy from the reactants to bound

product is 10.7 kcal·mol^{-1}. Previous theoretical studies were not able to locate a

transition state for this step of the reaction pathway and thus estimated, from the

peroxynitrite bound intermediate species, that the entropic barrier would be

approximately 10.4 kcal·mol^{-1}.[206] This is in excellent agreement with the value reported

herein. It should be noted that both the *cis* and *trans* conformations of the peroxynitrite

bound species were explored. Consistent with previous studies,[207] (the *Z* or *cis*)

conformer was found to be favoured by 2.6 kcal·mol^{-1}.

Table 6.1. The change in Gibbs energy, ΔG, enthalpy, ΔH, and entropy, ΔS, at 298 K for
the stationary points of mechanism 3. Energies reported relative to the reactants, FePL-O$_2$
+ NO.

	ΔG, kcal·mol^{-1}	ΔH, kcal·mol^{-1}	-TΔS, kcal·mol^{-1}	ΔS, cal·mol^{-1}·K^{-1}
FePL-O$_2$ + NO	0	0	0	0
TS1	3.8	-5.6	9.3	-31.3
FePL-OONO	-11.2	-21.7	10.5	-35.3
TS2	-10.4	-21.6	11.3	-37.8
FePL=O···NO$_2$	-28.5	-35.0	6.5	-21.7
TS3	-18.7	-25.9	7.1	-23.9
FePL-NO$_3$	-37.9	-48.8	10.9	-36.5

In the second step of this mechanism, the O-O bond is homolytically cleaved to

yield the oxo-Fe(IV) species and the NO$_2$ radical, FePHis=O···NO$_2$. This step of the

reaction is exergonic by 17.3 kcal·mol^{-1}, and has a very small reaction barrier of 0.8

kcal·mol^{-1}. It should be noted that the local nature of the GGA exchange-correlation hole leads to failures in non-equilibrium, or stretched, geometries where a non-local description of the exchange hole is necessary. In other words, reaction barriers are underestimated by GGA-type density functional approximations. Nonetheless, a discussion of the reaction barriers relative to one another is valuable for understanding the mechanism. As a comparison, the barrier for this step of the reaction was reported to be 6.7 kcal·mol^{-1} in an investigation that employed a hybrid density functional approximation, B3LYP, and a similar model system.[206]

It should be noted that at low pH the peroxynitrite species is not observed.[194,195] Under these conditions, the distal histidine in the heme pocket is protonated and does not play a role in stabilizing species bound in the active site. The current model is effectively modelling these conditions, since the distal histidine is not included. Thus, it is reasonable to assume from the low reaction barrier reported here that the peroxynitrite intermediate decays too fast to be detected, and faster than the rate of formation of the intermediate, making it very difficult to detect experimentally.

The third step of the mechanism involves the combination of the NO$_2$ radical with the oxo-Fe(IV) species to give a bound nitrate ligand. This step of the reaction is exergonic by 9.4 kcal·mol^{-1}, and has a reaction barrier of 9.8 kcal·mol^{-1}. The reaction barrier for this step of the reaction is the highest, thus, does not support the notion that the oxo-Fe(IV) species reacts too fast to be detected. Based on the results it is expected that the rate of formation would be greater than the rate of decay. Since this study does not include the distal histidine group, known to stabilize dioxygen by 2.5-3.8 kcal·mol^{-1},[146,165] it is possible that the distal histidine plays a role in varying degrees of stabilization along

the reaction pathway. This is supported by experimental evidence that the rate of nitrate production increases with decreasing pH, thus without stabilization from the distal histidine the reaction proceeds faster. Another theoretical study on the effects of the distal histidine group on this reaction pathway has shown that the barriers are increased upon inclusion of the distal histidine and have a greater effect on TS2 than TS3.[206] However, this study employs a different model system and choice of density functional approximation, thus, further computational investigation would be most appropriate to provide insight on the effects of the distal histidine residue.

6.3.2 Amino Acid Substitution

The first step of the mechanism has been investigated further to determine if the electronic effects of the amino acid in the proximal site are significant enough to have an effect of the affinity of NO for the oxygen bound species. The first step is chosen since the first step in unchanged for each of the proposed mechanisms. This step involves the generation of the iron (III)-peroxynitrite complex, FePL-OONO, from the reaction between the nitric oxide radical and the open-shell singlet species, FePHis-O_2. To determine the effect of the amino acid residue on the nitric oxide affinity of oxy-iron porphyrin systems, substitutions at the proximal histidine residue are investigated. The seven amino acids chosen for substitution are: arginine (Arg), cysteine (Cys), glutamic acid (Glu), histidine (His), methionine (Met) and tyrosine (Tyr). The abbreviation used herein is given in parentheses. Model systems of these amino acid residues are employed, which exclude the protein backbone. The structures of these ligands have been shown previously, in Figure 5.3 of Chapter 5. The minimum structures for the first step of the mechanism for the histidine model system, the reaction between FePHis-O_2

and nitric oxide to form the iron (III)-peroxynitrite complex, FePHis-OONO, are shown

in Figure 6.5.

<center>(a)   (b)</center>
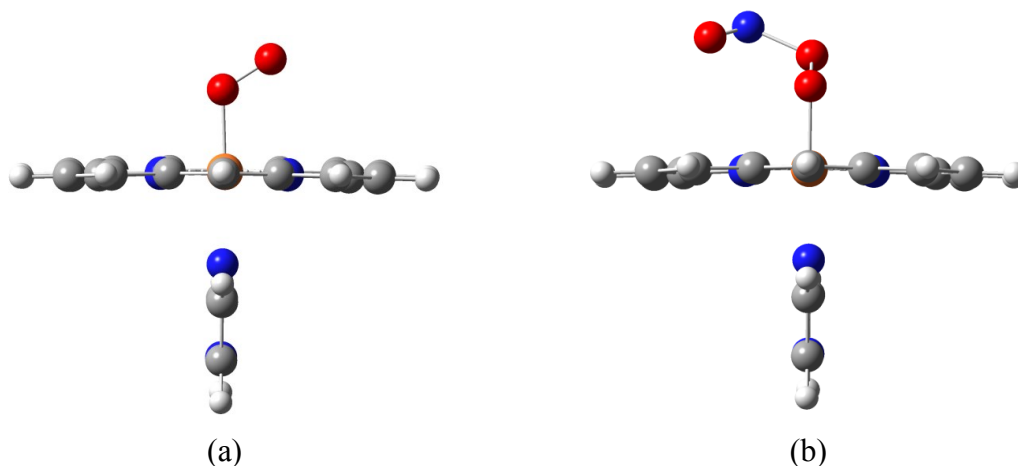
Figure 6.5. Optimized geometries for FePHis-O_2, shown in (a), and FePHis-OONO, shown in (b).

     The geometry of the heme pocket is defined by the six atoms coordinating to the

iron atom. The equatorial ligands, the four nitrogen atoms of the porphine ring, have the

same geometry in the case of each substitution, with an average Fe-N distance of 2.02 Å

and an average N-N distance of 2.86 Å. The axial ligands are the coordinating atom of

the amino acid model system, denoted L, and the coordinating oxygen atom of the

OONO ligand. The distances for the axial ligands are given in Table 6.2. The Fe-L

distances vary based on the type of coordinating atom and its van der Waals radius, with

sulfur coordinating systems having the longest Fe-L distance, followed by the nitrogen

and then oxygen systems. Interestingly, the Fe-O distances, shown in Table 6.2, do not

exhibit this trend.

Table 6.2. Structural parameters (distances in Å, angles in °) for the FePL-OONO systems. The bond distances in the peroxynitrite ligands are denoted using the image to the right of the table.

L	Fe-L	Fe-O	A	B	C
Arg	2.07	1.86	1.38	1.60	1.16
Cys	2.27	1.96	1.39	1.52	1.18
Glu	1.95	1.87	1.42	1.48	1.18
His	2.03	1.84	1.38	1.59	1.16
Met	2.42	1.85	1.37	1.62	1.16
Tyr	1.92	1.90	1.41	1.49	1.18
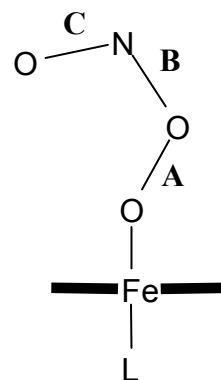
Table 6.3. Bond distances for Fe-O and N-O compared with the NO stretching frequency (distances in Å, angles in °) for the FePL-OONO systems.

L	Fe-O	N-O	NO stretching frequency, cm^{-1}
Arg	1.857	1.161	1743
Cys	1.962	1.180	1645
Glu	1.869	1.180	1647
His	1.843	1.161	1743
Met	1.854	1.158	1760
Tyr	1.901	1.180	1647
Free NO		1.157	1904

Not surprisingly, there is a correlation between the distance of B, or the interaction between the nitric oxide and the oxygen with the distance at A and C, as shown in Table 6.2. The trend is such that the systems with shorter B lengths, have longer A and C lengths. Thus, a stronger interaction between the nitric oxide and the dioxygen weakens the original O-O bond of dioxygen and the original N-O bond of nitric

oxide. The frequency of the N-O bond is reported in Table 6.3. As expected, there is a correlation with the strength of the N-O bond, such that the systems exhibiting greater interaction with nitric oxide, or longer N-O bond distance, exhibit the longest Fe-O bond distances. These are the Cys, Glu and Tyr systems. It is interesting to note that these are the systems that exhibited the greater superoxide change in the oxy-iron porphine systems shown in Chapter 5. This suggests that electron density for the interaction with nitric oxide may also be coming from both the superoxide species and the iron centre. To investigate this assertion, analysis of the electron density is necessary. Conversely, systems with shorter N-O bonds, which are closer to the free nitric oxide bond length, exhibit a higher stretching frequency, again closer to the free nitric oxide.

The atomic charge and electron density at the bond critical points for the FePL-OONO systems, as evaluated using QTAIM, are shown in Table 6.4 and Table 6.5, respectively. T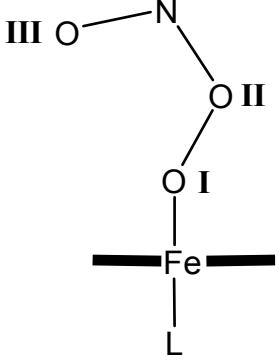he trend observed in the bond lengths where systems with shorter B lengths, have longer A and C lengths, is also observed in the electron density. From Table 6.5, systems with greater electron density at the BCP, or stronger interaction, for B, are accompanied with lower electron density at the BCP, or weaker interaction, for A and C. Analogously, the Fe-O interaction strength shows correlation with the strength of the N-O bond, such that the systems exhibiting greater interaction with nitric oxide, noted above as Cys, Glu and Tyr, exhibit the weakest Fe-O interactions.

Table 6.4. Atomic charges (au) evaluated using QTAIM for the FePL-OONO systems. The oxygen atoms are denoted using the image to the right of the table.
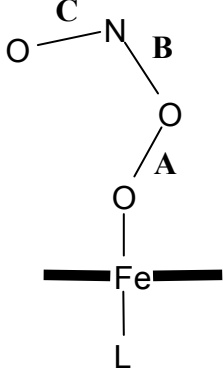
L	Charge					
	Fe	L	I	II	N	III
Arg	1.33	-1.06	-0.37	-0.20	0.48	-0.41
Cys	1.23	-0.30	-0.42	-0.20	0.41	-0.45
Glu	1.38	-1.03	-0.41	-0.20	0.44	-0.44
His	1.34	-1.06	-0.37	-0.20	0.49	-0.41
Met	1.26	0.01	-0.36	-0.19	0.49	-0.41
Tyr	1.37	-0.99	-0.42	-0.20	0.43	-0.44
OONO-						

Table 6.5. The electron density at the bond critical points, ρ_{BCP} (au), for the FePL-OONO systems, evaluated using QTAIM analysis.

L	ρ_{BCP}				
	Fe-L	Fe-O	A	B	C
Arg	0.074	0.117	0.333	0.195	0.576
Cys	0.081	0.088	0.324	0.240	0.551
Glu	0.087	0.111	0.293	0.263	0.552
His	0.080	0.121	0.329	0.197	0.577
Met	0.057	0.118	0.341	0.183	0.581
Tyr	0.096	0.102	0.306	0.254	0.552
OONO-					

The binding energy for nitric oxide to FePL-O_2 is denoted as BE_{NO}, and is defined as the energy difference between the bound system and the infinitely separated reactants:

$$BE_{NO} = \left(E_{FePL-O_2} + E_{NO}\right) - E_{FePL-OONO} \qquad 6.1$$

In this way, a positive value of BE_{NO} indicates favourable binding.

The computed values for BE_{NO} are shown in Table 6.6. For comparison, the binding energies reported for dioxygen to the deoxy-iron porphine system, denoted as BE_{O_2} and computed in Chapter 5, are also shown. From the results presented above, it is reasonable to expect that the Cys, Glu and Tyr systems would exhibit the greatest nitric oxide binding energy, BE_{NO}, due to the greater superoxide character of their FePL-O$_2$ complex and strongest NO interaction as discussed above. However, just as these systems did not exhibit a greater BE_{O_2}, as discussed in Chapter 5, they did not exhibit an increase in NO affinity. This again highlights the complexity of the amino acid systems with respect to reactivity. Overall, there is no correlation between oxygen and nitric oxide affinity.

Table 6.6. Calculated Gibbs binding energy for nitric oxide binding to FePLO$_2$ at 298 K (kcal·mol^{-1}). The reaction is exergonic, however the values are given as positive quantities for simplicity. Oxygen binding energies, from Chapter 5, are also included for comparison.

L	BE_{O_2}, kcal·mol^{-1}	BE_{NO}, kcal·mol^{-1}
Arg	6.7	9.1
Cys	10.2	10.9
Glu	3.2	13.5
His	6.9	11.2
Met	3.6	12.2
Tyr	6.7	10.9

Arginine is interesting because it exhibits a similar affinity for oxygen as the His reference systems, yet a different nitric oxide affinity. The Arg system exhibits a modest decrease in NO affinity relative to the reference His system. The lower NO affinity is likely a result of the low nature of the highest energy singly-occupied molecular orbital

(SOMO), shown in Figure 5.5 of Chapter 5. The arginine species had little superoxide character and the SOMO showed delocalization of the molecular orbital onto the iron atom, whereas the other systems showed a larger contribution of the SOMO from the dioxygen species. The low NO affinity of the Arg system makes it a potential mutant of interest in the field of CFBSs.

Table 6.7. Changes in the structural properties upon NO binding to FePL-O_2. The changes are represented as the difference in distance (Å) and the percent change (%). A negative change indicates a decrease in the distance upon NO binding. Systems are shown in order of increasing, BE_{NO}.

L	Δ Fe-L		Δ Fe-O		Δ O-O		Δ ∠Fe-O-O	
	Å	%	Å	%	Å	%	°	%
Arg	-0.025	-1.2	-0.004	-0.21	0.105	8.25	-14.1	-10.7
Tyr	-0.033	-1.7	0.015	0.80	0.117	9.06	-13.8	-10.6
Cys	-0.042	-1.8	0.011	0.56	0.097	7.51	-5.0	-4.1
His	-0.045	-2.2	-0.003	-0.16	0.109	8.55	-4.6	-3.8
Met	-0.077	-3.1	0.087	4.92	0.101	7.95	-6.6	-5.3
Glu	-0.037	-1.9	0.081	4.53	0.136	10.56	-9.7	-7.8

Table 6.8. Changes in the QTAIM charges (au) and electron density at the bond critical points, ρ_{BCP} (au), upon oxygen binding to FePL. A negative change indicates an increase in electron density upon binding with O_2. Systems are shown in order of increasing, BE_{NO}.

L	Δ Charge				Δ ρ_{BCP}		
	Fe	L	O (I)	O (II)	Fe-L	Fe-O	O-O
Arg	0.03	0.00	-0.12	-0.02	-0.004	-0.006	0.109
Tyr	0.02	0.02	-0.13	0.06	-0.013	0.003	0.144
Cys	0.01	0.03	-0.15	0.05	-0.007	0.006	0.099
His	0.02	0.01	-0.14	-0.03	-0.008	0.002	0.114
Met	0.02	0.02	-0.16	-0.01	-0.008	0.032	0.107
Glu	0.03	0.02	-0.16	0.05	-0.013	0.003	0.114

O (I) and O (II) are the proximal and distal oxygen atoms to the iron atom, respectively.

To further discuss the reported NO binding energies, it is useful to consider the effects of NO binding on the systems. The changes in structural and electronic properties upon NO binding are shown in Table 6.7 and Table 6.8, respectively. The Fe-N and N-N distances are not given in Table 6.7 as there is negligible change in structure upon binding, with all changes less than 0.01 Å. Similarly, there is negligible change in the electron density at the BCP for these interactions, where all changes are less than 0.001 au. Thus, these values are not reported in Table 6.8.

The three systems with the strongest NO interaction discussed above, Cys, Glu and Tyr, are the only systems that show the distal oxygen atom becoming more electropositive. These systems exhibit the greater superoxide character in the oxy-porphyrin form, allowing the greater interaction with the approaching NO radical. Thus, the superoxide character of the FePL-O_2 species affects the nature of the NO binding.

It is interesting to note that upon nitric oxide binding, the iron and coordinating atom of the ligand, denoted in Table 6.8 as Fe and L, respectively, become more electropositive. Conversely, the proximal oxygen atom, denoted O (I) in Table 6.8, gains electron density, becoming more negative. Without further probing of the electron density it may be assumed that electron density is transferred from the iron system and ligand to the dioxygen upon binding. However, surprisingly, there is both a decrease in the Fe-L interaction length and an increase in electron density between the atoms, shown in Table 6.7 and Table 6.8, respectively. Thus, binding of NO strengthens the Fe-L interaction and is accompanied by a weakening of the Fe-O interaction, except in the Arg system, and in the O-O interaction in all cases. In other words, the interaction with NO

136

relies on the transfer of electron density from the Fe-O and O-O interactions. There is negligible transfer of electron density from the ligand and porphine ring.

As expected, there is a significant decrease in electron density from the O-O bond upon NO binding, relative to the Fe-L and Fe-O bond. The weakening of the O-O bond results in an increase in negative charge on the proximal oxygen atom. However, despite a greater electrostatic interaction between the iron and proximal oxygen, the Fe-O interaction is weakened as a result of the removed electron density. Nonetheless, the greater electrostatic interaction would be a barrier to free-peroxynitrite formation.

This is not the case in Arg, where the Fe-O interaction is strengthened. This would act as a driving force in the next step of the reaction, where the O-O bond is homolytically cleaved to yield the oxo-Fe(IV) species and the NO_2 radical. This step has been studied for the His system, as discussed above, which is exergonic and has a very low barrier of 0.8 kcal·mol^{-1}. Thus, the Arg system may potentially have an even lower barrier for this reaction. However, this system also has the weakest affinity for NO, thus further investigation of the mechanism is required in order to more conclusively assess the effects of Arg substituent.

The weakening of the O-O is also a driving force for the second step of the reaction, since it is the bond cleaved to form the oxo-Fe(IV) species and the NO_2 radical. The cysteine system has the smallest change in electron density, in other words, is the least weakened upon NO binding. Thus, this system is a potential system where this step would be inhibited. However, there is experimental evidence for the presence of the oxo-Fe(IV) complex in numerous cytochrome pathways.[202–204] Cytochrome P450

systems contain a heme group coordinated to the enzyme via a cysteine residue, thus the Cys ligand is an unlikely inhibitor of this step of the reaction pathway.

6.4   Conclusions

Overall, the systems with substituted amino acid ligands exhibit very similar affinity for the NO ligand. It has been shown that the electron density from the ligand has little involvement on the binding on NO to the dioxygen species. Thus, tuning the NO affinity relies more heavily on the electronics of the oxygen bound system, which were shown to exhibit dependence on the ligand in Chapter 5. Systems exhibiting the greater superoxide character show the strongest interaction with NO, although not necessarily the greatest nitric oxide binding energy. It is the nature of the interaction, rather than the binding energy that differs between the systems. These may affect the reaction mechanism for the oxidation of the iron porphyrin and generation of nitrate, however, future work is required to investigate this hypothesis. The reaction mechanism should be investigated further to elucidate the effects of amino acid substitution on the reaction barriers and mechanism.

Chapter 7 : Conclusions and Future Direction

7.1   Conclusions

The initial computational study pursued as part of this thesis is presented in Chapter 3. This chapter highlights the powerful nature of computational techniques, including QTAIM and DFT, to explain experimental observations. The atomic size of high-spin iron within the porphyrin structure is computed and explained as a consequence of the quantum mechanical interpretation of Hund's multiplicity rule. Instead the doming observed in this system is attributed to the nature of the molecular orbitals and resulting interactions with the porphyrin ring.

As further studies of the porphyrin system were initiated, the intricate nature of iron porphyrin systems was realized. Overall, the computational investigation of the heme system is a complex and surprisingly demanding task. Others have described the task of computing diatomic binding energies to heme as "more difficult than expected"[208] and "well beyond routine quantum mechanical modeling."[143] This thesis has supported these notions and has shown the complexity of the iron porphyrin system and some significant hurdles when studying this system as well as analogous systems with density functional theory. The conclusions of the benchmarking and exchange study in Chapter 4 call for the development of better density functional methods that are feasible with reasonable computational resources. Currently, the ideal computational approaches for this system are not practical. In particular, the work in this thesis should alert researchers in this field to use extra caution when selecting their computational methodology.

Chapters 5 and 6 further establish the complexity of the porphyrin system, but provide guidance of the electron nature of some biologically relevant substitutions on the

iron porphine system. Specifically, the effect on the binding of O_2 is determined and cysteine and tyrosine are highlighted as interesting modifications to the heme system. More specifically, these substituents provide significant oxygen activation ability; generating significant superoxide character in the O_2 bound complexes. Methionine is noted as a deactivator, decreasing both oxygen affinity and activation.

Subsequent reaction of these complexes with NO, show that the effect of amino acid substitution has little effect of the generation of the peroxynitrite intermediate. Analysis of the electron density upon formation of the peroxynitrite bound complex shows little transfer of electron density from the ligand, and instead the nature of the dioxygen moiety plays a greater role in NO affinity. However, these results are not conclusive of the effects of the substitutions on the full reaction mechanism.

Overall, interesting electronic properties of the iron porphyrin system are presented in this thesis. The complexity and intricacies of the electronic nature calls for careful consideration of the computational approaches used to study these systems. Accurate quantum mechanical methods are essential for the study of reactions with these systems.

7.2   Future Direction

7.2.1   Functional Development

Further study of the nature of the iron porphyrin system is essential as emphasized throughout this thesis. Although there are numerous extensive benchmarking studies of the iron porphine system, most lack insight on the characteristics of the functional form and how they manifest as benefits or errors specifically in the iron porphine

system.[136,137,143,144,209] Further studies as well as functional development are needed in this area. Specifically functionals that can describe strong correlation and charge transfer interactions should be targeted to study the binding of small molecules to metalloporphyrin complexes.

7.2.2   Oxygen Binding Energies

The oxygen binding energies reported in Chapter 5 are based on a model system of the iron porphyrin framework found in hemoglobin. Further work could be done to include more of the porphyrin framework, ideally employing quantum mechanical methods. Previous theoretical studies that include the distal histidine have shown only small effects on the energetics on the reaction pathway investigated herein.[206] Nonetheless, inclusion of the distal pocket would allow for further investigation of substitutions in this region.   This may also provide insight into the failures of experimental methods to inflict changes in binding affinity upon substitution of this distal histidine group of hemoglobin.[187]

7.2.3   Effects of NO on Oxyhemoglobin

Further investigation of the reaction mechanism proposed in Chapter 6 is of significant interest. The results in Chapter 6 only present the effects of amino acid substitution on the first step of the reaction and thus, are not conclusive of the effects of the substitutions on the full reaction mechanism. Although the effect of amino acid substitution has little effect on the first step of the investigated mechanism, the generation of the peroxynitrite intermediate, the effect may vary for the other steps of the reaction. The formation of the peroxynitrite intermediate is not the rate-determining step of the reaction, as it proceeds only via an entropic barrier. Thus, barrier heights for the

subsequent reaction steps are essential for determining the effects of the amino acid substitutions and to give a more complete explanation and picture of the effects of NO on oxyhemoglobin.

7.2.4 Metalloporphyrin Systems

Metalloporphyrins are incorporated into protein structure ubiquitously in nature. The most well-known and abundant example is the iron-containing class of proteins known as heme proteins, which have been the focus of this thesis. Another well-known metalloporphyrin is chlorophyll, which is a magnesium (II) porphyrin responsible for the absorption of energy from light, transferring it to the reaction centers of plants. The incorporation of metal ions is crucial for many proteins as it provides the catalytic and electron transfer functionality. Over one-third of natural proteins containing at least one metal ion, making the understanding of metal behaviour and the role of specific metal ions in these systems essential to the design of metalloenzymes for specialized processes.

Although considerable attention in metalloporphyrin chemistry is focussed on iron, magnesium and cobalt due to their biological significance, synthetic routes to synthesize a wide array of metalloporphyrin species is possible. These developments allow for a library of metalloporphyrin species to be generated with different structure and reactivity related to differences in character of the metal involved. The heme system is considered one of the most versatile groups in metalloproteins, making metalloporphyrins the focus of many research efforts. A simple iron porphine system was first used to effect the stereospecific olefin epoxidation and alkane hydroxylation in 1979.[210] The system was designed to mimic cytochrome P450, using iodosylbenzene as an oxygen-transfer agent. Manganese porphyrins have since been shown to have high

reactivity for these reactions.[211–214] Group 3 through 6 metals have also been incorporated into the porphyrin framework and studied extensively.[215]

The design of enzymes for both biological and alternative-energy applications is the ultimate challenge in the understanding of metalloprotein function. In the recent literature there have been successful reports of the modification of the metalloprotein structure to achieve efficient catalytic activity for the reduction of O_2 to H_2O as well as other biologically relevant hydrolysis reactions.[216–218] A recent study has proposed a solid state heme protein mimic with the ability to tune functionality by modification of the porphyrin structure and the organic linkers at the proximal and distal heme pocket sites.[219] This calls for further understanding of the porphyrin structure and key interactions that contribute to protein function. These properties have the potential to provide inspiration for the design of smaller synthetic analogues to mimic their function. They can also aid larger scale investigations where advanced computational methods have allowed for rational design of enzyme function.[218,220–224]

Preliminary work has been done to look at the structural and electronic properties of metalloporphyrins containing Sc, Ti, V, Cr and Mn at the central position. Chemically relevant oxidations states of each metal in three multiplicity states were investigated, employing a model system that comprises the metal within a porphine ring and an axial imidazole ligand. Structural and electronic properties such as geometry, charge, atomic volume, bond critical point electron density, as well as binding energies were computed. Computational methods were employed analogous to Chapter 5, where the B97-D functional is employed for binding properties and ωB97X-D for spin state energetics. No clear conclusions could be drawn from the study and it became increasingly clear that the

density functional approximations employed were not reliable for determining the properties sought.

The results shown in Chapter 4 of this thesis show the importance of including HF exchange in density functional approximations for the correct prediction of spins states; however, it is reasonable to assume that the precise amount varies based on the functional employed. The optimal amount of HF exchange may also vary based on the system studied. In other words, the current methods are not robust enough to apply broadly to metalloporphyrin systems. It follows that it is not reasonable to assume that the density functional approximation chosen in this thesis for the study of iron porphyrin systems is suitable for other metalloporphyrin systems. Future studies should be initiated to explore the performance of density functional methods for other metalloporphyrin systems. Experimental data is essential to clearly elucidate the characteristics of an optimal density functional approximation. As shown herein, the quality of spin state energetics and binding energies of dioxygen, show different dependence on the inclusion of HF exchange, thus both should be explored for the metalloporphyrin systems.

References

(1)   *The Porphyrin Handbook*; Kadish, K.; Smith, K. M.; Guilard, R., Eds.; Vol. 1-.; Academic Press: Boston, Massachusetts, 1999.

(2)   Milgrom, L. R. *The Colours of Life: An Introduction to the Chemistry of Porphyrins and Related Compounds*; Oxford University Press: Cambridge, UK, 1997.

(3)   Ghosh, A. Electronic Structure of Porphyrins and Metalloporphyrins: Past, Present and Future. *J. Porphyins Phthalocyanines* **2000**, *4*, 380–381.

(4)   Falk, J. E. *Porphyrins and Metalloporphyrins*; Smith, K. M., Ed.; Elsevier Scientific Publishing Company: Amsterdam, 1975.

(5)   Cramer, C. J. *Essentials of Computational Chemistry: Theories and Models*; 2nd ed.; John Wiley and Sons: West Sussex, England, 2004.

(6)   Leach, A. *Molecular Modelling: Principles and Applications*; 2nd ed.; Pearson Education Limited: Essex, England, 2001.

(7)   Jensen, F. *Introduction to Computational Chemistry*; 2nd ed.; John Wiley and Sons: West Sussex, England, 2007.

(8)   Planck, M. Ueber das Gesetz der Energieverteilung im Normalspectrum. *Ann. Phys.* **1901**, *4*, 553–563.

(9)   Einstein, A. Über einen die Erzeugung und Verwandlung des Lichtes betreffenden heuristischen Gesichtspunkt. *Ann. Phys.* **1905**, *17*, 132–148.

(10)   Koch, W.; Holthausen, M. C. *A Chemist's Guide to Density Functional Theory*; 2nd ed.; Wiley-VCH: Weinheim, Germany, 2001; Vol. 3.

(11)   McQuarrie, D. A. *Quantum Chemistry*; Murdzek, J., Ed.; 2nd ed.; University Science Books: Sausalito, California, 2008.

(12)   Levine, I. N. *Quantum Chemistry*; Challice, J., Ed.; 5th ed.; Prentice-Hall, Inc.: Upper Saddle River, New Jersey, 2000.

(13)   Hartree, D. R. The Wave Mechanics of an Atom with a Non-Coulomb Central Field. Part I. Theory and Methods. *Proc. Camb. Philol. Soc.* **1928**, *24*, 89–110.

(14)   Pipkin, F. M.; Ritter, R. C. Precision Measurements and Fundamental Constants. *Science* **1983**, *219*, 913–921.

(15)   Henrion, M.; Fischhoff, B. Assessing Uncertainty in Physical Constants. *Am. J. Phys.* **1986**, *54*, 791–798.

(16)   Schrödinger, E. Quantisierung als Eigenwertproblem. *Ann. Phys.* **1926**, *79*, 361–376.

(17)   Born, M.; Oppenheimer, R. Zur Quantentheorie der Molekeln. *Ann. Phys.* **1927**, *84*, 457–484.

(18)   Slater, J. C. The Theory of Complex Spectra. *Phys. Rev.* **1929**, *34*, 1293–1322.

(19)   Slater, J. C. Cohesion in Monovalent Metals. *Phys. Rev.* **1930**, *35*, 509–529.

(20)   Hartree, D. R. The Wave Mechanics of an Atom with a Non-Coulomb Central Field. Part II. Some Results and Discussion. *Proc. Camb. Philol. Soc.* **1928**, *24*, 111–132.

(21)   Gaunt, J. A. A Theory of Hartree's Atomic Fields. *Proc. Camb. Philol. Soc.* **1928**, *24*, 328–342.

(22)   Slater, J. C. The Self Consistent Field and the Structure of Atoms. *Phys. Rev.* **1928**, *32*, 339–348.

(23)   Slater, J. C. Note on Hartree's Method. *Phys. Rev.* **1930**, *35*, 210–211.

(24)   Fock, V. Naherungsmethode zur Lösung des Quantenmechanischen Mehrkörper-Problems. *Z. Phys.* **1930**, *61*, 126–148.

(25)   Hartree, D. R.; Hartree, W. Self-Consistent Field, with Exchange, for Beryllium. *Proc. R. Soc. London A* **1935**, *150*, 9–33.

(26)   Koopmans, T. A. Über die Zuordnung von Wellenfunktionen und Eigenwerten zu den Einzelnen Elektronen Eines Atoms. *Physica* **1934**, *1*, 104–113.

(27)   Roothaan, C. C. J. New Developments in Molecular Orbital Theory. *Rev. Mod. Phys.* **1951**, *23*, 69–89.

(28)   Hall, G. G. The Molecular Orbital Theory of Chemical Valency. VIII. A Method of Calculating Ionization Potentials. *Proc. R. Soc. London A* **1951**, *205*, 541–552.

(29)   Slater, J. C. Atomic Shielding Constants. *Phys. Rev.* **1930**, *36*, 57–64.

(30)   Boys, S. F. Electron Wave Functions I. A General Method of Calculation for the Stationary States of Any Molecular System. *Proc. R. Soc. London A* **1950**, *200*, 542–554.

(31) Hehre, W. J.; Stewart, R. F.; Pople, J. A. Self-Consistent Molecular-Orbital Methods. I. Use of Gaussian Expansions of Slater-Type Atmoic Orbitals. *J. Chem. Phys.* **1969**, *51*, 2657–2664.

(32) Ditchfield, R.; Hehre, W. J.; Pople, J. A. Self-Consistent Molecular Orbital Methods. IX. An Extended Gaussian-Type Basis for Molecular Orbital Studies of Organic Molecules. *J. Chem. Phys.* **1971**, *54*, 724–728.

(33) Binkley, J. S.; Pople, J. A.; Hehre, W. J. Self-Consistent Molecular Orbital Methods. 21. Small Split-Valence Basis Sets for First-Row Elements. *J. Am. Chem. Soc.* **1980**, *102*, 939–947.

(34) Dunning, T. H. J. Gaussian Basis Functions for Use in Molecular Calculations. I. Contraction of (9s5p) Atomic Basis Sets for the First-Row Atoms. *J. Chem. Phys.* **1970**, *53*, 2823–2833.

(35) Dunning, T. H. J. Gaussian Basis Sets for Use in Correlated Molecular Calculations. I. The Atoms Boron through Neon and Hydrogen. *J. Chem. Phys.* **1989**, *90*, 1007–1023.

(36) Schäfer, A.; Horn, H.; Ahlrichs, R. Fully Optimized Contracted Gaussian Basis Sets for Atoms Li to Kr. *J. Chem. Phys.* **1992**, *97*, 2571–2577.

(37) Schäfer, A.; Huber, R.; Ahlrichs, R. Fully Optimized Contracted Gaussian Basis Sets of Triple Zeta Valence Quality for Atoms Li to Kr. *J. Chem. Phys.* **1994**, *100*, 5829–5835.

(38) Ratner, M. A.; Schatz, G. C. *An Introduction to Quantum Mechanics in Chemistry*; Prentice-Hall, Inc.: Upper Saddle River, New Jersey, 2001.

(39) Møller, C.; Plesset, M. S. Note on an Approximation Treatment for Many-Electron Systems. *Phys. Rev.* **1934**, *46*, 618–622.

(40) Löwdin, P. O. Twenty-Five Years of Sanibel Symposia: A Brief Historic and Scientific Survey. *Int. J. Quantum Chem.* **1985**, *28*, 19–37.

(41) Thomas, L. H. The Calculation of Atomic Fields. *Proc. Camb. Philol. Soc.* **1927**, *23*, 542–548.

(42) Fermi, E. Un Metodo Statistico per la Determinazione di alcune Priorietà dell'Atomo. *Rend. Accad. Naz. Lincei.* **1927**, *6*, 602–607.

(43) Dirac, P. A. M. The Quantum Theory of the Electron. *Proc. R. Soc. London A* **1928**, *117*, 610–624.

(44)	Slater, J. C. A Simplification of the Hartree-Fock Method. *Phys. Rev.* **1951**, *81*, 385–390.

(45)	Hohenberg, P.; Kohn, W. Inhomogeneous Electron Gas. *Phys. Rev.* **1964**, *136*, B 864–871.

(46)	Kohn, W.; Sham, L. J. Self-Consistent Equations Including Exchange and Correlation Effects. *Phys. Rev.* **1965**, *140*, A 1133–1138.

(47)	*Theory and Applications of Computational Chemistry: The First Forty Years*; Dykstra, C. E.; Frenking, G.; Kim, K. S.; Scuseria, G. E., Eds.; Elsevier: Amsterdam, NL, 2005.

(48)	Grimme, S. Semiempirical Hybrid Density Functional with Perturbative Second-Order Correlation. *J. Chem. Phys.* **2006**, *124*, 034108.

(49)	Sim, F.; St-Amant, A.; Papai, I.; Salahub, D. R. Gaussian Density Functional Calculations on Hydrogen-Bonded Systems. *J. Am. Chem. Soc.* **1992**, *114*, 4391–4400.

(50)	Hamann, D. R. Generalized Norm-Conserving Pseudopotentials. *Phys. Rev. B* **1989**, *40*, 2980–2987.

(51)	Riley, K. E.; Op't Holt, B. T.; Merz, K. M. J. Critical Assessment of the Performance of Density Functional Methods for Several Atomic and Molecular Properties. *J. Chem. Theory Comput.* **2007**, *3*, 407–433.

(52)	Kohanoff, J. Exchange and Correlation in DFT: Approximations and Their Performances. In *Electronic Structure Calculations for Solids and Molecules*; Cambridge University Press: Cambridge, UK, 2006; pp. 75–122.

(53)	Becke, A. D. Density-Functional Exchange-Energy Approximation with Correct Asymptotic Behavior. *Phys. Rev. A* **1988**, *38*, 3098–3100.

(54)	Lee, C.; Yang, W.; Parr, R. G. Development of the Colle-Salvetti Correlation-Energy Formula into a Functional of the Electron Density. *Phys. Rev. B* **1988**, *37*, 785–789.

(55)	Becke, A. D. Density Functional Thermochemistry. III. The Role of Exact Exchange. *J. Chem. Phys.* **1993**, *98*, 5648–5652.

(56)	Dion, M.; Rydberg, H.; Schröder, E.; Langreth, D. C.; Lundqvist, B. I. van der Waals Density Functional for General Geometries. *Phys. Rev. Lett.* **2004**, *92*, 246401.

(57)   Dion, M.; Rydberg, H.; Schröder, E.; Langreth, D. C.; Lundqvist, B. I. Erratum: van der Waals Density Functional for General Geometries. *Phys. Rev. Lett.* **2005**, *95*, 109902.

(58)   von Lilienfeld, O. A.; Tavernelli, I.; Rothlisberger, U.; Sebastiani, D. Optimization of Effective Atom Centered Potentials for London Dispersion Forces in Density Functional Theory. *Phys. Rev. Lett.* **2004**, *93*, 153004.

(59)   Becke, A. D.; Johnson, E. R. Exchange-Hole Dipole Moment and the Dispersion Interaction. *J. Chem. Phys.* **2005**, *122*, 154104.

(60)   Becke, A. D.; Johnson, E. R. A Density-Functional Model of the Dispersion Interaction. *J. Chem. Phys.* **2005**, *123*, 154101.

(61)   Johnson, E. R.; Becke, A. D. A Post-Hartree–Fock Model of Intermolecular Interactions. *J. Chem. Phys.* **2005**, *123*, 024101.

(62)   Becke, A. D.; Johnson, E. R. Exchange-Hole Dipole Moment and the Dispersion Interaction: High-Order Dispersion Coefficients. *J. Chem. Phys.* **2006**, *124*, 014104.

(63)   Johnson, E. R.; Becke, A. D. A Post-Hartree-Fock Model of Intermolecular Interactions: Inclusion of Higher-Order Corrections. *J. Chem. Phys.* **2006**, *124*, 174104.

(64)   Grimme, S. Accurate Description of van der Waals Complexes by Density Functional Theory Including Empirical Corrections. *J. Comput. Chem.* **2004**, *25*, 1463–1473.

(65)   Grimme, S. Semiempirical GGA-Type Density Functional Constructed with a Long-Range Dispersion Correction. *J. Comput. Chem.* **2006**, *27*, 1787–1799.

(66)   Grimme, S.; Antony, J.; Ehrlich, S.; Krieg, H. A Consistent and Accurate *ab Initio* Parametrization of Density Functional Dispersion Correction (DFT-D) for the 94 Elements H-Pu. *J. Chem. Phys.* **2010**, *132*, 154104.

(67)   Zhao, Y.; Schultz, N. E.; Truhlar, D. G. Design of Density Functionals by Combining the Method of Constraint Satisfaction with Parameterization for Thermochemistry, Thermochemical Kinetics, and Noncovalent Interactions. *J. Chem. Theory Comput.* **2006**, *2*, 364–382.

(68)   Zhao, Y.; Truhlar, D. G. The M06 Suite of Density Functionals for Main Group Thermochemistry, Thermochemical Kinetics, Noncovalent Interactions, Excited States, and Transition Elements: Two New Functionals and Systematic Testing of Four M06-Class Functionals and 12 Other Function. *Theor. Chem. Acc.* **2008**, *120*, 215–241.

(69) Johnson, E. R.; Mackie, I. D.; DiLabio, G. A. Dispersion Interactions in Density-Functional Theory. *J. Phys. Org. Chem.* **2009**, *22*, 1127–1135.

(70) Gaussian 09. Revision C.01, Frisch, M. J.; Trucks, G. W.; Schlegel, H. B.; Scuseria, G. E.; Robb, M. A.; Cheeseman, J. R.; Scalmani, G.; Barone, V.; Mennucci, B.; Petersson, G. A.; Nakatsuji, H.; Caricato, M.; Li, X.; Hratchian, H. P.; Izmaylov, A. F.; Bloino, J.; Zheng, G.; Sonnenberg, J. L.; Hada, M.; Ehara, M.; Toyota, K.; Fukuda, R.; Hasegawa, J.; Ishida, M.; Nakajima, T.; Honda, Y.; Kitao, O.; Nakai, H.; Vreven, T.; Montgomery Jr., J. A.; Peralta, J. E.; Ogliaro, F.; Bearpark, M.; Heyd, J. J.; Brothers, E.; Kudin, K. N.; Staroverov, V. N.; Kobayashi, R.; Normand, J.; Raghavachari, K.; Rendell, A.; Burant, J. C.; Iyengar, S. S.; Tomasi, J.; Cossi, M.; Rega, N.; Millam, J. M.; Klene, M.; Knox, J. E.; Cross, J. B.; Bakken, V.; Adamo, C.; Jaramillo, J.; Gomperts, R.; Stratmann, R. E.; Yazyev, O.; Austin, A. J.; Cammi, R.; Pomelli, C.; Ochterski, J. W.; Martin, R. L.; Morokuma, K.; Zakrzewski, V. G.; Voth, G. A.; Salvador, P.; Dannenberg, J. J.; Dapprich, S.; Daniels, A. D.; Farkas, O.; Foresman, J. B.; Ortiz, J. V; Cioslowski, J.; Fox, D. J. Gaussian Inc., Wallingford CT, USA, 2009.

(71) Schlegel, H. B. Optimization of Equilibrium Geometries and Transition Structures. *J. Comput. Chem.* **1982**, *3*, 214–218.

(72) Bader, R. F. W. *Atoms in Molecules: A Quantum Theory*; Oxford University Press: USA, 1990.

(73) Popelier, P. L. A. *Atoms in Molecules: An Introduction*; Prentice-Hall, Inc.: London, 2000.

(74) *The Quantum Theory of Atoms in Molecules: From Solid State to DNA and Drug Design*; Matta, C. F.; Boyd, R. J., Eds.; Wiley-VCH: Weinheim, Germany, 2007.

(75) Löwdin, P. O. Quantum Theory of Many-Particle Systems. I. Physical Interpretations by Means of Density Matrices, Natural Spin-Orbitals, and Convergence Problems in the Method of Configurational Interaction. *Phys. Rev.* **1955**, *97*, 1474–1489.

(76) Poater, J.; Solà, M.; Duran, M.; Fradera, X. The Calculation of Electron Localization and Delocalization Indices at the Hartree-Fock, Density Functional and Post-Hartree-Fock Levels of Theory. *Theor. Chem. Acc.* **2002**, *107*, 362–371.

(77) Fradera, X.; Austen, M. A.; Bader, R. F. W. The Lewis Model and Beyond. *J. Phys. Chem. A* **1999**, *103*, 304–314.

(78) Chesnut, D. B.; Bartolotti, L. J. The Pair Density Description of Aromaticity in Some Substituted Cyclopentadienyl Systems: A Comparison of AIM and ELF Bonding Descriptors. *Chem. Phys.* **2000**, *257*, 175–181.

(79)   Kar, T.; Ángyán, J. G.; Sannigrahi, A. B. Comparison of *ab Initio* Hartree-Fock and Kohn-Sham Orbitals in the Calculation of Atomic Charge, Bond Index, and Valence. *J. Phys. Chem. A* **2000**, *104*, 9953–9963.

(80)   Baerends, E. J. Exact Exchange-Correlation Treatment of Dissociated H2 in Density Functional Theory. *Phys. Rev. Lett.* **2001**, *87*, 133004.

(81)   Dobado, J. A.; Martínez-García, H.; Molina, J.; Sundberg, M. R. Chemical Bonding in Hypervalent Molecules Revised. 3. Application of the Atoms in Molecules Theory to Y_3X-CH_2 (X = N, P, or As; Y = H or F) and H_2X-CH_2 (X = O, S, or Se) Ylides. *J. Am. Chem. Soc.* **2000**, *122*, 1144–1149.

(82)   Ploegman, J. H.; Drent, G.; Kalk, K. H.; Hol, W. G. J. The Structure of Bovine Liver Rhodanese: II. The Active Site in the Sulfur-Substituted and the Sulfur-Free Enzyme. *J. Mol. Biol.* **1979**, *127*, 149–162.

(83)   Bader, R. F. W. Bond Paths Are Not Chemical Bonds. *J. Phys. Chem. A* **2009**, *113*, 10391–10396.

(84)   Bader, R. F. W. A Bond Path: A Universal Indicator of Bonded Interactions. *J. Phys. Chem. A* **1998**, *102*, 7314–7323.

(85)   Walker, V. E. J.; Castillo, N.; Matta, C. F.; Boyd, R. J. The Effect of Multiplicity on the Size of Iron(II) and the Structure of Iron(II) Porphyrins. *J. Phys. Chem. A* **2010**, *114*, 10315–10319.

(86)   Campbell, M. K. *Biochemistry*; 3rd ed.; Harcourt Brace and Company: Philadelphia, PA, 1999.

(87)   Lamoen, D.; Parrinello, M. Geometry and Electronic Structure of Porphyrins and Porphyrazines. *Chem. Phys. Lett.* **1996**, *248*, 309–315.

(88)   Matsuzawa, N.; Ata, M.; Dixon, D. A. Density Functional Theory Prediction of the Second-Order Hyperpolarizability of Metalloporphines. *J. Phys. Chem.* **1995**, *99*, 7698–7706.

(89)   Reynolds, C. H. An AM1 Theoretical Study of the Structure and Electronic Properties of Porphyrin. *J. Org. Chem.* **1988**, *53*, 6061–6064.

(90)   Loew, G. H.; Harris, D. L. Role of the Heme Active Site and Protein Environment in Structure, Spectra, and Function of the Cytochrome P450s. *Chem. Rev.* **2000**, *100*, 407–420.

(91)   Li, X.-Y.; Zgierski, M. Z. Iron Motion in a Five-Coordinated Heme Model. *Chem. Phys. Lett.* **1992**, *188*, 16–20.

(92) Hu, X.; Rodgers, K. R.; Mukerji, I.; Spiro, T. G. New Light on Allostery: Dynamic Resonance Raman Spectroscopy of Hemoglobin Kempsey. *Biochemistry* **1999**, *38*, 3462–3467.

(93) Perutz, M. F.; Wilkinson, A. J.; Paoli, M.; Dodson, G. G. The Stereochemical Mechanism of the Cooperative Effects in Hemoglobin Revisited. *Annu. Rev. Biophys. Biomol. Struct.* **1998**, *27*, 1–34.

(94) Fermi, G.; Perutz, M. F.; Shaanan, B. The Crystal Structure of Human Deoxyhaemoglobin at 1.74 Å Resolution. *J. Mol. Biol.* **1984**, *175*, 159–174.

(95) Reedy, C. J.; Gibney, B. R. Heme Protein Assemblies. *Chem. Rev.* **2004**, *104*, 617–650.

(96) Hoard, J. L.; Hamor, M. J.; Hamor, T. A.; Caughey, W. S. The Crystal Structure and Molecular Stereochemistry of Methoxyiron(III) Mesoporphyrin-IX Dimethyl Ester. *J. Am. Chem. Soc.* **1965**, *87*, 2312–2319.

(97) Countryman, R.; Collins, D. M.; Hoard, J. L. Stereochemistry of the Low-Spin Iron Porphyrin, Bis(imidazole)-α,β,γ,δ-tetraphenylporphinatoiron(III) Chloride. *J. Am. Chem. Soc.* **1969**, *91*, 5166–5167.

(98) Boyd, R. J. Relative Sizes of High and Low Spin States of Atoms. *Nature* **1974**, *250*, 566–567.

(99) Pichou, F.; Huetz, A.; Joyez, G.; Landau, M.; Mazeau, J. Electron Impact Excitation of Helium: Absolute Differential Cross Sections of the n=2 and 3^3S States from Threshold to 3.6 eV above. *J. Phys. B Atom. Mol. Phys.* **1976**, *9*, 933–944.

(100) Ugalde, J. M.; Dunietz, B. D.; Dreuw, A.; Head-Gordon, M.; Boyd, R. J. The Spin Dependence of the Spatial Size of Fe(II) and of the Structure of Fe(II)-Porphyrins. *J. Phys. Chem. A* **2004**, *108*, 4653–4657.

(101) Boyd, R. J. A Quantum Mechanical Explanation for Hund's Multiplicity Rule. *Nature* **1984**, *310*, 480–481.

(102) Rovira, C.; Kunc, K.; Hutter, J.; Ballone, P.; Parrinello, M. Equilibrium Geometries and Electronic Structure of Iron-Porphyrin Complexes: A Density Functional Study. *J. Phys. Chem. A* **1997**, *101*, 8914–8925.

(103) Dunietz, B. D.; Dreuw, A.; Head-Gordon, M. Initial Steps of the Photodissociation of the CO Ligated Heme Group. *J. Phys. Chem. B* **2003**, *107*, 5623–5629.

(104) Kaim, W.; Schwederski, B. *Bioinorganic Chemistry: Inorganic Elements in the Chemistry of Life*; J. Wiley and Sons: New York, 1994.

(105) Scheidt, W. R.; Reed, C. A. Spin-State/Stereochemical Relationships in Iron Porphyrins: Implications for the Hemoproteins. *Chem. Rev.* **1981**, *81*, 543–555.

(106) Housecroft, C. E.; Sharpe, A. G. *Inorganic Chemistry*; Prentice-Hall, Inc.: Essex, England, 2001.

(107) Shao, Y.; Molnar, L. F.; Jung, Y.; Kussmann, J.; Ochsenfeld, C.; Brown, S. T.; Gilbert, A. T. B.; Slipchenko, L. V; Levchenko, S. V; O'Neill, D. P.; DiStasio, R. a; Lochan, R. C.; Wang, T.; Beran, G. J. O.; Besley, N. a; Herbert, J. M.; Lin, C. Y.; Van Voorhis, T.; Chien, S. H.; Sodt, A.; Steele, R. P.; Rassolov, V. a; Maslen, P. E.; Korambath, P. P.; Adamson, R. D.; Austin, B.; Baker, J.; Byrd, E. F. C.; Dachsel, H.; Doerksen, R. J.; Dreuw, A.; Dunietz, B. D.; Dutoi, A. D.; Furlani, T. R.; Gwaltney, S. R.; Heyden, A.; Hirata, S.; Hsu, C.-P.; Kedziora, G.; Khalliulin, R. Z.; Klunzinger, P.; Lee, A. M.; Lee, M. S.; Liang, W.; Lotan, I.; Nair, N.; Peters, B.; Proynov, E. I.; Pieniazek, P. a; Rhee, Y. M.; Ritchie, J.; Rosta, E.; Sherrill, C. D.; Simmonett, A. C.; Subotnik, J. E.; Woodcock, H. L.; Zhang, W.; Bell, A. T.; Chakraborty, A. K.; Chipman, D. M.; Keil, F. J.; Warshel, A.; Hehre, W. J.; Schaefer, H. F.; Kong, J.; Krylov, A. I.; Gill, P. M. W.; Head-Gordon, M. Advances in Methods and Algorithms in a Modern Quantum Chemistry Program Package. *Phys. Chem. Chem. Phys.* **2006**, *8*, 3172–3191.

(108) McMahon, B. H.; Stojković, B. P.; Hay, P. J.; Martin, R. L.; García, A. E. Microscopic Model of Carbon Monoxide Binding to Myoglobin. *J. Chem. Phys.* **2000**, *113*, 6831–6850.

(109) Kozlowski, P. M.; Spiro, T. G.; Bérces, A.; Zgierski, M. Z. Low-Lying Spin States of Iron(II) Porphine. *J. Phys. Chem. B* **1998**, *102*, 2603–2608.

(110) Dunietz, B. D.; Beachy, M. D.; Cao, Y.; Whittington, D. A.; Lippard, S. J.; Friesner, R. A. Large Scale *ab Initio* Quantum Chemical Calculation of the Intermediates in the Soluble Methane Monooxygenase Catalytic Cycle. *J. Am. Chem. Soc.* **2000**, *122*, 2828–2839.

(111) Ricca, A.; Bauschlicher, C. W. J. Theoretical Study of $Fe(CO)_n{}^-$. *J. Phys. Chem.* **1995**, *99*, 5922–5926.

(112) AIMAll, Version 14.04.17, Keith, T. A. TK Gristmill Software, Overland Park, KS, USA, 2014 (aim.tkgristmill.com).

(113) AIM2000, Version 2.0, Biegler-König, F.; Schönbohm, J. SBK Software, Bielefeld, DE, 2002 (aim2000.de).

(114) Boyd, R. J.; Coulson, C. A. Coulomb Hole in Some Excited States of Helium. *J. Phys. B Atom. Mol. Phys.* **1973**, *6*, 782–793.

(115) Boyd, R. J.; Choi, S. C. Hydrogen Bonding Between Nitriles and Hydrogen Halides and the Topological Properties of Molecular Charge Distributions. *Chem. Phys. Lett.* **1986**, *129*, 62–65.

(116) Knop, O.; Boyd, R. J.; Choi, S. C. S-S Bond Lengths, or Can a Bond Length Be Estimated from a Single Parameter? *J. Am. Chem. Soc.* **1988**, *110*, 7299–7301.

(117) Ethirajan, M.; Chen, Y.; Joshi, P.; Pandey, R. K. The Role of Porphyrin Chemistry in Tumor Imaging and Photodynamic Therapy. *Chem. Soc. Rev.* **2011**, *40*, 340–362.

(118) Chandra, R.; Tiwari, M.; Kaur, P.; Sharma, M.; Jain, R.; Dass, S. Metalloporphyrins - Applications and Clinical Significance. *Indian J. Clin. Biochem.* **2000**, *15*, 183–199.

(119) Sheng, H.; Chaparro, R. E.; Sasaki, T.; Izutsu, M.; Pearlstein, R. D.; Tovmasyan, A.; Warner, D. S. Metalloporphyrins as Therapeutic Catalytic Oxidoreductants in Central Nervous System Disorders. *Antioxid. Redox Signal.* **2014**, *20*, 2437–2464.

(120) Sun, Y.; Chen, K.; Jia, L.; Li, H. Toward Understanding Macrocycle Specificity of Iron on the Dioxygen-Binding Ability: A Theoretical Study. *Phys. Chem. Chem. Phys.* **2011**, *13*, 13800–13808.

(121) Ali, E.; Sanyal, B.; Oppeneer, P. M. Electronic Structure, Spin-States, and Spin-Crossover Reaction of Heme-Related Fe-Porphyrins: A Theoretical Perspective. *J. Phys. Chem. B* **2012**, *116*, 5849–5859.

(122) Tsuchida, E.; Sou, K.; Nakagawa, A.; Sakai, H.; Komatsu, T.; Kobayashi, K. Artificial Oxygen Carriers, Hemoglobin Vesicles and Albumin-Hemes, Based on Bioconjugate Chemistry. *Bioconjug. Chem.* **2009**, *20*, 1419–1440.

(123) Mori-Sánchez, P.; Cohen, A. J.; Yang, W. Localization and Delocalization Errors in Density Functional Theory and Implications for Band-Gap Prediction. *Phys. Rev. Lett.* **2008**, *100*, 146401.

(124) Zheng, X.; Liu, M.; Johnson, E. R.; Contreras-García, J.; Yang, W. Delocalization Error of Density-Functional Approximations: A Distinct Manifestation in Hydrogen Molecular Chains. *J. Chem. Phys.* **2012**, *137*, 214106.

(125) Ruzsinszky, A.; Perdew, J. P.; Csonka, G. I.; Vydrov, O. A.; Scuseria, G. E. Spurious Fractional Charge on Dissociated Atoms: Pervasive and Resilient Self-Interaction Error of Common Density Functionals. *J. Chem. Phys.* **2006**, *125*, 194112.

(126) Johnson, E. R.; Mori-Sánchez, P.; Yang, W. Delocalization Errors in Density Functionals and Implications for Main-Group Thermochemistry. *J. Chem. Phys.* **2008**, *129*, 204112.

(127) Chai, J.-D.; Head-Gordon, M. Long-Range Corrected Hybrid Density Functionals with Damped Atom-Atom Dispersion Corrections. *Phys. Chem. Chem. Phys.* **2008**, *10*, 6615–6620.

(128) Chai, J.-D.; Head-Gordon, M. Systematic Optimization of Long-Range Corrected Hybrid Density Functionals. *J. Chem. Phys.* **2008**, *128*, 084106.

(129) Akinaga, Y.; Ten-no, S. Range-Separation by the Yukawa Potential in Long-Range Corrected Density Functional Theory with Gaussian-Type Basis Functions. *Chem. Phys. Lett.* **2008**, *462*, 348–351.

(130) Sun, Y.; Hu, X.; Li, H.; Jalbout, A. F. Metalloporphyrin-Dioxygen Interactions and the Effects of Neutral Axial Ligands. *J. Phys. Chem. C* **2009**, *113*, 14316–14323.

(131) Caughey, W. S.; Barlow, C. H.; Maxwell, J. C.; Volpe, J. A.; Wallace, W. J. Reactions of Oxygen with Hemoglobin, Cytochrome c Oxidase and Other Hemeproteins. *Ann. N. Y. Acad. Sci.* **1975**, *244*, 1–8.

(132) Perdew, J. P.; Burke, K.; Ernzerhof, M. Generalized Gradient Approximation Made Simple. *Phys. Rev. Lett.* **1996**, *77*, 3865–3868.

(133) Perdew, J. P.; Burke, K.; Ernzerhof, M. Errata: Generalized Gradient Approximation Made Simple. *Phys. Rev. Lett.* **1997**, *78*, 1396.

(134) Adamo, C.; Barone, V. Toward Reliable Density Functional Methods without Adjustable Parameters: The PBE0 Model. *J. Chem. Phys.* **1999**, *110*, 6158–6169.

(135) Siegbahn, P. E. M.; Blomberg, M. R. A.; Chen, S.-L. Significant van der Waals Effects in Transition Metal Complexes. *J. Chem. Theory Comput.* **2010**, *6*, 2040–2044.

(136) Rong, C.; Lian, S.; Yin, D.; Zhong, A.; Zhang, R.; Liu, S. Effective Simulation of Biological Systems: Choice of Density Functional and Basis Set for Heme-Containing Complexes. *Chem. Phys. Lett.* **2007**, *434*, 149–154.

(137) Liao, M.-S.; Huang, M.-J.; Watts, J. D. Iron Porphyrins with Different Imidazole Ligands. A Theoretical Comparative Study. *J. Phys. Chem. A* **2010**, *114*, 9554–9569.

(138) Alcantara, R. E.; Xu, C.; Spiro, T. G.; Guallar, V. A Quantum-Chemical Picture of Hemoglobin Affinity. *Proc. Natl. Acad. Sci. USA* **2007**, *104*, 18451–18455.

(139) Kachalova, G. S.; Popov, A. N.; Bartunik, H. D. A Steric Mechanism for Inhibition of CO Binding to Heme Proteins. *Science* **1999**, *284*, 473–476.

(140) Vojtěchovský, J.; Chu, K.; Berendzen, J.; Sweet, R. M.; Schlichting, I. Crystal Structures of Myoglobin-Ligand Complexes at Near-Atomic Resolution. *Biophys. J.* **1999**, *77*, 2153–2174.

(141) Chen, H.; Ikeda-Saito, M.; Shaik, S. Nature of the Fe-O_2 Binding in Oxy-Myoglobin: Effect of the Protein. *J. Am. Chem. Soc.* **2008**, *130*, 14778–14790.

(142) Unno, M.; Chen, H.; Kusama, S.; Shaik, S.; Ikeda-Saito, M. Structural Characterization of the Fleeting Ferric Peroxo Species in Myoglobin: Experiment and Theory. *J. Am. Chem. Soc.* **2007**, *129*, 13394–13395.

(143) Radoń, M.; Pierloot, K. Binding of CO, NO, and O_2 to Heme by Density Functional and Multireference *ab Initio* Calculations. *J. Phys. Chem. A* **2008**, *112*, 11824–11832.

(144) Radoń, M.; Pierloot, K. Erratum: Binding of CO, NO, and O_2 to Heme by Density Functional and Multireference *ab Initio* Calculations. *J. Phys. Chem. A* **2011**, *115*, 7871.

(145) Scherlis, D. A.; Estrin, D. A. Structure and Spin-State Energetics of an Iron Porphyrin Model: An Assessment of Theoretical Methods. *Int. J. Quantum Chem.* **2002**, *87*, 158–166.

(146) Olson, J. S.; Phillips, G. N. J. Myoglobin Discriminates between O_2 , NO, and CO by Electrostatic Interactions with the Bound Ligand. *J. Biol. Inorg. Chem.* **1997**, *2*, 544–552.

(147) Private correspondence with John Olson regarding unpublished temperature dependence studies of myoglobin.

(148) Foster, M. E.; Wong, B. M. Nonempirically Tuned Range-Separated DFT Accurately Predicts Both Fundamental and Excitation Gaps in DNA and RNA Nucleobases. *J. Chem. Theory Comput.* **2012**, *8*, 2682–2687.

(149) Fouqueau, A.; Mer, S.; Casida, M. E.; Lawson Daku, L. M.; Hauser, A.; Mineva, T.; Neese, F. Comparison of Density Functionals for Energy and Structural Differences between the High- $[^5T_{2g}:(t_{2g})^4(e_g)^2]$ and Low- $[^1A_{1g}:(t_{2g})^6(e_g)^0]$ Spin States of the Hexaquoferrous Cation $[Fe(H_2O)_6]^{2+}$. *J. Chem. Phys.* **2004**, *120*, 9473–9486.

(150) Fouqueau, A.; Casida, M. E.; Lawson Daku, L. M.; Hauser, A.; Neese, F. Comparison of Density Functionals for Energy and Structural Differences between the High- $[^5T_{2g}:(t_{2g})^4(e_g)^2]$ and Low- $[A_{1g}:(t_{2g})^6(e_g)^0]$ Spin States of Iron(II) Coordination Compounds. II. More Functionals and the Hexaminoferrous Cation, $[Fe(NH_3)_6]^{2+}$. *J. Chem. Phys.* **2005**, *122*, 44110.

(151) Becke, A. D. A Real-Space Model of Nondynamical Correlation. *J. Chem. Phys.* **2003**, *119*, 2972–2977.

(152) Jensen, K. P.; Roos, B. O.; Ryde, U. O_2-Binding to Heme: Electronic Structure and Spectrum of Oxyheme, Studied by Multiconfigurational Methods. *J. Inorg. Biochem.* **2005**, *99*, 45–54.

(153) Jensen, K. P.; Roos, B. O.; Ryde, U. Erratum to "O_2-Binding to Heme: Electronic Structure and Spectrum of Oxyheme, Studied by Multiconfigurational Methods" [J. Inorg. Biochem. 99(1) (2004) 45–54]. *J. Inorg. Biochem.* **2005**, *99*, 978.

(154) Otero-de-la-Roza, A.; Johnson, E. R. Non-Covalent Interactions and Thermochemistry Using XDM-Corrected Hybrid and Range-Separated Hybrid Density Functionals. *J. Chem. Phys.* **2013**, *138*, 204109.

(155) Berryman, V. E. J.; Baker, M. G.; Boyd, R. J. Effect of Amino Acid Ligands on the Structure of Iron Porphyrin and Their Ability to Bind Oxygen. *J. Phys. Chem. A* **2014**, *118*, 4565–4574.

(156) Lu, Y.; Berry, S. M.; Pfister, T. D. Engineering Novel Metalloproteins: Design of Metal-Binding Sites into Native Protein Scaffolds. *Chem. Rev.* **2001**, *101*, 3047–3080.

(157) Campbell, A. N.; Stahl, S. S. Overcoming the "Oxidant Problem": Strategies to Use O_2 as the Oxidant in Organometallic C-H Ocidation Reactions Catalyzed by Pd (and Cu). *Acc. Chem. Res.* **2012**, *45*, 851–863.

(158) Hamada, D.; Kuroda, Y.; Kataoka, M.; Aimoto, S.; Yoshimura, T.; Goto, Y. Role of Heme Axial Ligands in the Conformational Stability of the Native and Molten Globule States of Horse Cytochrome c. *J. Mol. Biol.* **1996**, *256*, 172–186.

(159) Sorrell, T. N.; Martin, P. K.; Bowden, E. F. A Novel, Functional Variant of Cytochrome c: Replacement of the Histidine Ligand with Arginine via Site-Directed Mutagenesis. *J. Am. Chem. Soc.* **1989**, *111*, 766–767.

(160) Adachi, S. I.; Nagano, S.; Ishomori, K.; Watanabe, Y.; Morishima, I.; Egawa, T.; Kitagawa, T.; Makino, R. Roles of Proximal Ligand in Heme Proteins: Replacement of Proximal Histidine of Human Myoglobin with Cysteine and Tyrosine by Site-Directed Mutagenesis as Model for P-450, Chloroperoxidase, and Catalase. *Biochemistry* **1993**, *32*, 241–252.

(161) Reid, T. J. I.; Murthy, M. R. N.; Sicignano, A.; Tanaka, N.; Musick, W. D. L.; Rossmann, M. G. Structure and Heme Environment of Beef Liver Catalase at 2.5 Å Resolution. *Proc. Natl. Acad. Sci. USA* **1981**, *78*, 4767–4771.

(162) Cheesman, M. R.; Thomson, A. J.; Greenwood, C.; Moore, G. R.; Kadir, F. Bis-Methionine Axial Ligation of Haem in Bacterioferritin from Pseudomonas Aeruginosa. *Nature* **1990**, *346*, 771–773.

(163) Kaysser, T. M.; Ghaim, J. B.; Georgiou, C.; Gennis, R. B. Methionine-393 is an Axial Ligand of the Heme b_{558} Component of the Cytochrome bd Ubiquinol Oxidase from Escherichia Coli. *Biochemistry* **1995**, *34*, 13491–13501.

(164) Glukhovtsev, M. N.; Bach, R. D.; Nagel, C. J. Performance of B3LYP/ECP DFT Calculations of Iron-Containing Compounds. *J. Phys. Chem. A* **1997**, *101*, 316–323.

(165) Springer, B. A.; Egeberg, K. D.; Sligar, S. G.; Rohlfs, R. J.; Mathews, A. J.; Olson, J. S. Discrimination between Oxygen and Carbon Monoxide and Inhibition of Autooxidation by Myoglobin. Site-Directed Mutagenesis of the Distal Histidine. *J. Biol. Chem.* **1989**, *264*, 3057–3060.

(166) Dudev, T.; Lim, C. Factors Governing the Protonation State of Cysteines in Proteins: An *ab Initio*/CDM Study. *J. Am. Chem. Soc.* **2002**, *124*, 6759–6766.

(167) Ratilla, E. M. A.; Kostie, N. M. Guanidyl Groups: New Metal-Binding Ligands in Biomolecules. Reactions of Chloro(2,2':6',2"-terpyridine)platinum(II) with Arginine in Two Cytochromes c and with Other Guanidyl Ligands. *J. Am. Chem. Soc.* **1988**, *110*, 4427–4428.

(168) Perera, R.; Sono, M.; Sigman, J. A.; Pfister, T. D.; Lu, Y.; Dawson, J. H. Neutral Thiol as a Proximal Ligand to Ferrous Heme Iron: Implications for Heme Proteins That Lose Cysteine Thiolate Ligation on Reduction. *Proc. Natl. Acad. Sci. USA* **2003**, *100*, 3641–3646.

(169) Ramachandran, G. N.; Mazumdar, S. K.; Venkatesan, K.; Lakshminarayanan, A. V. Conformation of the Arginine Side-Group and Its Variations. *J. Mol. Biol.* **1966**, *15*, 232–242.

(170) Hol, W. G. J.; van Duijnen, P. T.; Berendsen, H. J. C. The α-Helix Dipole and the Properties of Proteins. *Nature* **1978**, *273*, 443–446.

(171) Patthy, L.; Thész, J. Origin of the Selectivity of α-Dicarbonyl Reagents for Arginyl Residues of Anion-Binding Sites. *Eur. J. Biochem.* **1980**, *105*, 387–393.

(172) Sundaramoorthy, M.; Terner, J.; Poulos, T. L. The Crystal Structure of Chloroperoxidase: A Heme Peroxidase-Cytochrome P450 Functional Hybrid. *Structure* **1995**, *3*, 1367–1377.

(173) Keller, R. M.; Wuthrich, K.; Debrunner, P. G. Proton Magnetic Resonance Reveals High-Spin Iron (II) in Ferrous Cytochrome P450$_{cam}$ from Pseudomonas Putida. *Proc. Natl. Acad. Sci. USA* **1972**, *69*, 2073–2075.

(174) Poulos, T. L.; Finzel, B. C.; Howard, A. J. High-Resolution Crystal Structure of Cytochrome P450$_{cam}$. *J. Mol. Biol.* **1987**, *195*, 687–700.

(175) Putnam, C. D.; Arvai, A. S.; Bourne, Y.; Tainer, J. A. Active and Inhibited Human Catalase Structures: Ligand and NADPH Binding and Catalytic Mechanism. *J. Mol. Biol.* **2000**, *296*, 295–309.

(176) Katsumoto, S.; Smith, S. M. E.; Martasek, P.; Salerno, J. C. Competition and Binding of Arginine, Imidazole, and Aminoguanidine to Endothelial Nitric Oxide Synthase: Aminoguanidine Is a Poor Model for Substrate, Intermediate, and Arginine Analog Inhibitor Binding. *Nitric Oxide* **2003**, *8*, 149–154.

(177) Stowasser, R.; Hoffmann, R. What Do the Kohn-Sham Orbitals and Eigenvalues Mean? *J. Am. Chem. Soc.* **1999**, *121*, 3414–3420.

(178) Squires, J. E. Artifical Blood. *Science* **2012**, *295*, 1002–1005.

(179) Everts, S. Artifical Blood. *Chem. Eng. News* **2009**, *87*, 52–55.

(180) D'Agnillo, F.; Chang, T. M. S. Polyhemoglobin-Superoxide Dismutase-Catalase as a Blood Substitute with Antioxidant Properties. *Nat. Biotechnol.* **1998**, *16*, 667–671.

(181) Spahn, D.; Kocian, R. Artificial O$_2$ Carriers: Status in 2005. *Curr. Pharm. Des.* **2005**, *11*, 4099–4114.

(182) Doherty, D. H.; Doyle, M. P.; Curry, S. R.; Vali, R. J.; Fattor, T. J.; Olson, J. S.; Lemon, D. D. Rate of Reaction with Nitric Oxide Determines the Hypertensive Effect of Cell-Free Hemoglobin. *Nat. Biotechnol.* **1998**, *16*, 672–676.

(183) Palmer, A. F. Molecular Volume and HBOC-Induced Vasoconstriction. *Blood* **2006**, *108*, 3231–3232.

(184) Thompson, A. J.; McGarry, A. E.; Valeri, C. R.; Lieberthal, W. Stroma-Free Hemoglobin Increases Blood Pressure and GFR in the Hypotensive Rat: Role of Nitric Oxide. *J. Appl. Physiol.* **1994**, *77*, 2348–2354.

(185) Feldman, P. L.; Griffith, O. W.; Stuehr, D. J. Surprising Life of Nitric Oxide. *Chem. Eng. News* **1993**, *71*, 26–38.

(186) Olson, J. S.; Foley, E. W.; Rogge, C.; Tsai, A.-L.; Doyle, M. P.; Lemon, D. D. NO Scavenging and the Hypertensive Effect of Hemoglobin-Based Blood Substitutes. *Free Radic. Biol. Med.* **2004**, *36*, 685–697.

(187) Eich, R. F.; Li, T.; Lemon, D. D.; Doherty, D. H.; Curry, S. R.; Aitken, J. F.; Mathews, A. J.; Johnson, K. A.; Smith, R. D.; Phillips, G. N.; Olson, J. S. Mechanism of NO-Induced Oxidation of Myoglobin and Hemoglobin. *Biochemistry* **1996**, *35*, 6976–6983.

(188) Winslow, R. M. Artificial Blood: Ancient Dream, Modern Enigma. *Nat. Biotechnol.* **1998**, *16*, 621–622.

(189) Brunori, M. Nitric Oxide, Cytochrome-c Oxidase and Myoglobin. *Trends Biochem. Sci.* **2001**, *26*, 21–23.

(190) Brunori, M. Nitric Oxide Moves Myoglobin Centre Stage. *Trends Biochem. Sci.* **2001**, *26*, 209–210.

(191) Livingston, D. J.; McLachlan, S. J.; La Mar, G. N.; Brown, W. D. Myoglobin: Cytochrome b_5 Interactions and the Kinetic Mechanism of Metmyoglobin Reductase. *J. Biol. Chem.* **1985**, *260*, 15699–15707.

(192) Wade, R. S.; Castro, C. E. Reactions of Oxymyoglobin with NO, NO_2, and NO_2^- under Argon and in Air. *Chem. Res. Toxicol.* **1996**, *9*, 1382–1390.

(193) Stern, M. K.; Jensen, M. P.; Kramer, K. Peroxynitrite Decomposition Catalysts. *J. Am. Chem. Soc.* **1996**, *118*, 8735–8736.

(194) Herold, S. Kinetic and Spectroscopic Characterization of an Intermediate Peroxynitrite Complex in the Nitrogen Monoxide Induced Oxidation of Oxyhemoglobin. *FEBS Lett.* **1999**, *443*, 81–84.

(195) Herold, S.; Exner, M.; Nauser, T. Kinetic and Mechanistic Studies of the NO^- Mediated Oxidation of Oxymyoglobin and Oxyhemoglobin. *Biochemistry* **2001**, *40*, 3385–3395.

(196) Doyle, M. P.; Hoekstra, J. W. Oxidation of Nitrogen Oxides by Bound Dioxygen in Hemoproteins. *J. Inorg. Biochem.* **1981**, *14*, 351–358.

(197) Huie, R. E.; Padmaja, S. The Reaction of NO with Superoxide. *Free Radic. Res.* **1993**, *18*, 195–199.

(198) Bytheway, I.; Hall, M. B. Theoretical Calculations of Metal-Dioxygen Complexes. *Chem. Rev.* **1994**, *94*, 639–658.

(199) Momenteau, M.; Reed, C. A. Synthetic Heme Dioxygen Complexes. *Chem. Rev.* **1994**, *94*, 659–698.

(200) Lee, J.; Hunt, J. A.; Groves, J. T. Mechanisms of Iron Porphyrin Reactions with Peroxynitrite. *J. Am. Chem. Soc.* **1998**, *120*, 7493–7501.

(201) Yukl, E. T.; de Vries, S.; Moënne-Loccoz, P. The Millisecond Intermediate in the Reaction of Nitric Oxide with Oxymyoglobin Is an Iron (III)-Nitrato Complex , Not a Peroxynitrite. *J.* **2009**, *131*, 7234–7235.

(202) Schlichting, I.; Berendzen, J.; Chu, K.; Stock, A. M.; Maves, S. A.; Benson, D. E.; Sweet, R. M.; Ringe, D.; Petsko, G. A.; Sligar, S. G. The Catalytic Pathway of Cytochrome P450$_{cam}$ at Atomic Resolution. *Science* **2000**, *287*, 1615–1622.

(203) Ohno, T.; Suzuki, N.; Dokoh, T.; Urano, Y.; Kikuchi, K.; Hirobe, M.; Higuchi, T.; Nagano, T. Remarkable Axial Thiolate Ligand Effect on the Oxidation of Hydrocarbons by Active Intermediate of Iron Porphyrin and Cytochrome P450. *J. Inorg. Biochem.* **2000**, *82*, 123–125.

(204) Woodward, J. J.; Chang, M. M.; Martin, N. I.; Marletta, M. A. The Second Step of the Nitric Oxide Synthase Reaction: Evidence for Ferric-Peroxo as the Active Oxidant. *J. Am. Chem. Soc.* **2009**, *131*, 297–305.

(205) Freeman, G.; Dyer, R. L.; Juhos, L. T.; St. John, G. A.; Anbar, M. Identification of Nitric Oxide (NO) in Human Blood. *Arch. Environ. Health* **1978**, *33*, 19–23.

(206) Blomberg, L. M.; Blomberg, M. R. A.; Siegbahn, P. E. M. A Theoretical Study of Myoglobin Working as a Nitric Oxide Scavenger. *J. Biol. Inorg. Chem.* **2004**, *9*, 923–935.

(207) Tsai, H.-H.; Hamilton, T. P.; Tsai, J.-H. M.; van der Woerd, M.; Harrison, J. G.; Jablonsky, M. J.; Beckman, J. S.; Koppenol, W. H. *ab Initio* and NMR Study of Peroxynitrite and Peroxynitrous Acid: Important Biological Oxidants. *J. Phys. Chem.* **1996**, *100*, 15087–15095.

(208) Blomberg, L. M.; Blomberg, M. R. A.; Siegbahn, P. E. M. A Theoretical Study on the Binding of O_2, NO and CO to Heme Proteins. *J. Inorg. Biochem.* **2005**, *99*, 949–958.

(209) Liao, M.-S.; Huang, M.-J.; Watts, J. D. FeP(Im)-AB Bonding Energies Evaluated with a Large Number of Density Functionals (P=Porphine, Im=Imidazole, AB=CO, NO and O_2). *Mol. Phys.* **2011**, *109*, 2035–2048.

(210) Groves, J. T.; Nemo, T. E.; Myers, R. S. Hydroxylation and Epoxidation Catalyzed by Iron-Porphine Complexes. Oxygen Transfer from Iodosylbenzene. *J. Am. Chem. Soc.* **1979**, *101*, 1032–1033.

(211) Groves, J. T.; Kruper, W. J.; Haushalter, R. C. Hydrocarbon Oxidations and Oxometalloporphinates. Isolation and Reactions of a (Porphinato)Manganese(V) Complex. *J. Am. Chem. Soc.* **1980**, *102*, 6375–6377.

(212) Hill, C. L.; Schardt, B. C. Alkane Activation and Functionalization under Mild Conditions by a Homogeneous Manganese(III)Porphyrin-Iodosylbenzene Oxidizing System. *J. Am. Chem. Soc.* **1980**, *102*, 6374–6375.

(213) Meunier, B.; Guilmet, E.; De Carvalho, M.-E.; Poilblanc, R. Sodium Hypochlorite: A Convenient Oxygen Source for Olefin Epoxidation Catalyzed by (Porphyrinato)Manganese Complexes. *J. Am. Chem. Soc.* **1984**, *106*, 6668–6676.

(214) De Pooter, B.; Meunier, B. Metalloporphyrin-Catalysed Epoxidation of Terminal Aliphatic Olefins with Hypochlorite Salts or Potassium Hydrogen Persulphate. *J. Chem. Soc. Perkin Trans. 2* **1985**, *11*, 1735–1740.

(215) Brand, H.; Arnold, J. Recent Developments in the Chemistry of Early Transition Metal Porphyrin Compounds. *Coord. Chem. Rev.* **1995**, *140*, 137–168.

(216) Miner, K. D.; Mukherjee, A.; Gao, Y.-G.; Null, E. L.; Petrik, I. D.; Zhao, X.; Yeung, N.; Robinson, H.; Lu, Y. A Designed Functional Metalloenzyme That Reduces O_2 to H_2O with Over One Thousand Turnovers. *Angew. Chemie* **2012**, *51*, 5589–5592.

(217) Liu, X.; Yu, Y.; Hu, C.; Zhang, W.; Lu, Y.; Wang, J. Significant Increase of Oxidase Activity through the Genetic Incorporation of a Tyrosine–Histidine Cross-Link in a Myoglobin Model of Heme–Copper Oxidase. *Angew. Chemie* **2012**, *51*, 4312–4316.

(218) Zastrow, M. L.; Peacock, A. F. A.; Stuckey, J. A.; Pecoraro, V. L. Hydrolytic Catalysis and Structural Stabilization in a Designed Metalloprotein. *Nat. Chem.* **2012**, *4*, 118–123.

(219) Larsen, R. W.; Wojtas, L.; Perman, J.; Musselman, R. L.; Zaworotko, M. J.; Vetromile, C. M. Mimicking Heme Enzymes in the Solid State: Metal-Organic Materials with Selectively Encapsulated Heme. *J. Am. Chem. Soc.* **2011**, *133*, 10356–10359.

(220) Korendovych, I. V; Senes, A.; Kim, Y. H.; Lear, J. D.; Fry, H. C.; Therien, M. J.; Blasie, J. K.; Walker, F. A.; DeGrado, W. F. *De Novo* Design and Molecular Assembly of a Transmembrane Diporphyrin-Binding Protein Complex. *J. Am. Chem. Soc.* **2010**, *132*, 15516–15518.

(221) Koder, R. L.; Anderson, J. L. R.; Solomon, L. A.; Reddy, K. S.; Moser, C. C.; Dutton, P. L. Design and Engineering of an O_2 Transport Protein. *Nature* **2009**, *458*, 305–309.

(222) Thyme, S. B.; Jarjour, J.; Takeuchi, R.; Havranek, J. J.; Ashworth, J.; Scharenberg, A. M.; Stoddard, B. L.; Baker, D. Exploitation of Binding Energy for Catalysis and Design. *Nature* **2009**, *461*, 1300–1304.

(223) Yeung, N.; Lin, Y.-W.; Gao, Y.-G.; Zhao, X.; Russell, B. S.; Lei, L.; Miner, K. D.; Robinson, H.; Lu, Y. Rational Design of a Structural and Functional Nitric Oxide Reductase. *Nature* **2009**, *462*, 1079–1082.

(224) Jiang, L.; Althoff, E. A.; Clemente, F. R.; Doyle, L.; Rothlisberger, D.; Zanghellini, A.; Gallaher, J. L.; Betker, J. L.; Tanaka, F.; Barbas, C. F. I.; Hilvert, D.; Houk, K. N.; Stoddard, B. L.; Baker, D. *De Novo* Computational Design of Retro-Aldol Enzymes. *Science* **2008**, *319*, 1387–1391.

Appendix: Copyright Permission Letters

The following is the copyright permission letter from the publishers of the journal articles included in this thesis. The letters correspond to publications used in the following chapters:

- Chapter 3: Walker, V. E. J.; Castillo, N.; Matta, C. F.; Boyd, R. J. The Effect of Multiplicity on the Size of Iron(II) and the Structure of Iron(II) Porphyrins. *J. Phys. Chem. A* **2010**, *114*, 10315–10319.

- Chapter 5: Berryman, V. E. J.; Baker, M. G.; Boyd, R. J. Effect of Amino Acid Ligands on the Structure of Iron Porphyrin and Their Ability to Bind Oxygen. *J. Phys. Chem. A* **2014**, *118*, 4565–4574.

PERMISSION/LICENSE IS GRANTED FOR YOUR ORDER AT NO CHARGE

ACS Publications
Most Trusted. Most Cited. Most Read.

Title: Effect of Amino Acid Ligands on the Structure of Iron Porphyrins and Their Ability to Bind Oxygen

Author: Victoria E. J. Berryman, Matthew G. Baker, Russell J. Boyd

Publication: The Journal of Physical Chemistry A

Publisher: American Chemical Society

Date: Jun 1, 2014

Copyright © 2014, American Chemical Society